Magnetic Resonance Imaging

A Bayesian Approach to 2D Acceleration for Studying Activation Detection Rate for Simultaneously Encoded Slice Acquisition in FMRI
--Manuscript Draft--

A Bayesian Approach to 2D Acceleration for Studying Activation Detection Rate for Simultaneously Encoded Slice Acquisition in FMRI

Ke Xu[a], Daniel B. Rowe[a,*]

[a]*Computational Mathematical and Statistical Sciences, Marquette University, 1313 W Wisconsin Ave, Milwaukee, 53233, WI, USA*

Abstract

Functional Magnetic Resonance Imaging (fMRI) enables researchers to study brain function and advance understanding in human sciences. Spatial and temporal changes in brain metabolism as by detecting the Blood Oxygen Level Dependent (BOLD) contrast signal are represented in the frequency domain of an image, known as k-space. Traditional MRI methodologies require full k-space information, which follows a unique data acquisition sequence to reconstruct the complete image. This process presents a time-consuming obstacle for medical imaging techniques. Our study proposes a novel image reconstruction method to enhance the efficiency of data acquisition while maintaining high accuracy in activation detection. The through-plane and in-plane acceleration techniques are combined to accelerate image acquisition along two dimensions. Multiple image-shift strategies and a 2D Hadamard encoding scheme are used to increase encoding diversity and reduce slice leakage. By applying our approach to both simulated and experimental fMRI data, we successfully reduced total scan time while achieving a higher signal-to-noise ratio (SNR) and contrast-to-noise ratio (CNR) in regions of interest (ROI). Compared with conventional reconstruction strategies, the proposed method demonstrates potential improvements in activation detection under specific acceleration and encoding conditions, while also providing voxel-wise estimates through a Bayesian framework.

Keywords:

*Corresponding author.
Email address:* `daniel.rowe@marquette.edu` (Daniel B. Rowe)

1. Introduction

1.1. Complex-Valued Bayesian Model

Functional magnetic resonance imaging (fMRI) studies can be interpreted following the Bayesian methodology but with complex-valued observations. To set up a complex-valued Bayesian linear model, the complex-valued observation can be written as Eq. 1:

$$a_C = X_C \beta_C + \varepsilon_C. \tag{1}$$

In Eq. 1, a_C is a $p \times 1$ complex-valued observed vector, X_C is a $p \times q$ complex-valued known design matrix, β_C is a $q \times 1$ complex-valued unobserved regression coefficient vector, and ε_C is a complex-valued measurement error vector with same dimension as vector a_C, where p is the number of observations, and q is the number of regression coefficients. Moreover, the real and imaginary component of the measurement error ε_C follow normal distribution with $\varepsilon_R, \varepsilon_I \sim N(0, \sigma^2 I_p)$. In the application of this study, a_C is the complex-valued observed coil measurements vector, X_C is the complex-valued observed coil sensitivity matrix, and β_C is the unobserved voxel values vector. Eq. 1 can be reformulated through a real-valued isomorphism to transform the complex-valued model into a real-valued model:

$$\begin{bmatrix} a_R \\ a_I \end{bmatrix} = \begin{bmatrix} X_R & -X_I \\ X_I & X_R \end{bmatrix} \begin{bmatrix} \beta_R \\ \beta_I \end{bmatrix} + \begin{bmatrix} \varepsilon_R \\ \varepsilon_I \end{bmatrix}. \tag{2}$$

In Eq. 2, the dimension of observation vector $a = [a_R; a_I]$ is $2p \times 1$, the dimension of design matrix $X = [X_R, -X_I; X_I, X_R]$ is $2p \times 2q$, the dimension of regression coefficient vector $\beta = [\beta_R; \beta_I]$ is $2q \times 1$, and the dimension of measurement error vector $\varepsilon = [\varepsilon_R; \varepsilon_I]$ is $2p \times 1$.

To enhance anatomical detail and improve the resolution of reconstructed images, calibration images can be incorporated as prior information. The Tikhonov regularization algorithm has been shown to effectively increase the signal-to-noise ratio (SNR) (Lin et al. [12]). However, careful selection of the regularization parameter λ is crucial for optimal performance. In this paper, we propose a Bayesian complex-valued image reconstruction algorithm. Compared with Tikhonov regularization, the Bayesian framework enables

principled use of calibration data and provides posterior estimates. This facilitates the construction of confidence intervals and hypothesis testing. As a result, inter-slice signal leakage can be eliminated, and correlations between reconstructed slices can be reduced. Based on prior knowledge and experience, the regression coefficient β (voxel values) is specified to have a normal prior distribution $P(\beta \mid \sigma^2)$, and the measurement error σ^2 is specified to have an inverse gamma prior distribution $P(\sigma^2 \mid \cdot)$. Thus, the posterior distribution of regression coefficient β and variance σ^2 is proportional to the joint distribution of the likelihood and the prior distributions:

$$P(\beta, \sigma^2 \mid \cdot) \propto P(a \mid X, \beta, \sigma^2)P(\beta \mid \sigma^2)P(\sigma^2 \mid \cdot). \tag{3}$$

The joint posterior distribution of the regression coefficient β (voxel values) and measurement error σ^2 can be integrated to obtain their marginal distributions and hence their marginal posterior mean (MPM) and variance. In this study, the complex-valued Bayesian reconstruction framework constitutes the central conceptual component of the proposed methodology, and its formulation is presented in detail in Section 2. The simulation and experimental analyses described in Sections 4 and 5 are designed to evaluate the performance of this framework, particularly in terms of activation detection stability, noise propagation, and reconstruction robustness under different image-shift strategies and acceleration factors. Limitations of the current approach and potential directions for future research are discussed in Section 6.

1.2. FMRI Background

In the functional magnetic resonance imaging (fMRI) study field, the topic of improving the efficiency of data acquisition in the image scanning process has been gaining researchers' interest since 1990. As a noninvasive medical imaging technique, the blood-oxygen-level dependent (BOLD) contrast signal is detected as the proxy reflecting neuron activation changes over time (Ogawa et al. [14]). In order to acquire the fully sampled spatial frequency space, known as k-space, the gradient echo echo-planar imaging (GRE-EPI) pulse sequence is applied to shorten the scan time and reduce the respiratory artifacts within a single excitation (Mansfield [13]; Redzian et al. [20]; Stehling et al. [24]). Fig. 1 illustrates a three-dimensional view of the brain image scanning process and the unique data acquisition sequential pattern in the k-space of the GRE-EPI pulse sequence (Sakitis et al. [21]).
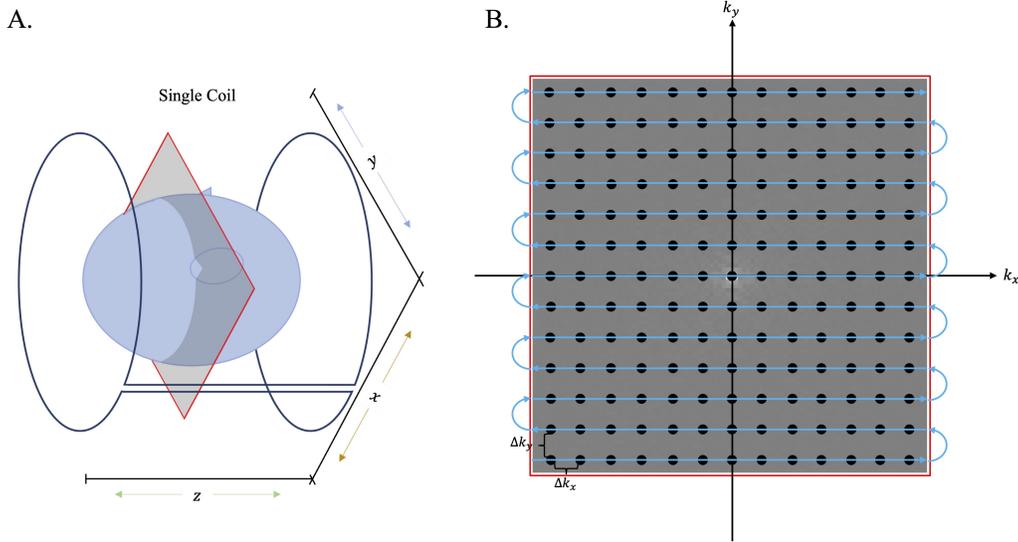
Figure 1: A. The three-dimensional view of brain image acquisition process with one single coil. B. The zig-zag data collecting pattern of GRE-EPI pulse sequence.

However, conducting an fMRI experiment requires acquiring multiple brain images at multiple slices, forming what is known as a volume-image.

In 1986, Hyde introduced a parallel image acquisition technique that incorporated multiple coils, with each coil measuring partial sensitivity-weighted spatial frequencies (Hyde et al. [7]). A full brain image can be reconstructed by applying the Sensitivity Encoding (SENSE) approach to combine weighted spatial frequencies from each coil into one single k-space array (Pruessmnn et al. [15]). In order to reduce the total image scan time, the data acquisition can be accelerated along two dimensions: the in-plane dimension and the through-plane dimension. The in-plane acceleration (IPA) method aims at expediting the single slice readout process by skipping partial lines in the k-space. As an alternative to SENSE, the unacquired spatial frequency points can be estimated by the application of the generalized autocalibrating partially parallel acquisition (GRAPPA) approach (Griswold et al. [6]). Prior information of missing data in the k-space can be obtained from the calibration images. Fig. 2A illustrates the brain image acquisition process with four receiver coils and the subsampled spatial frequency domain for IPA approach with acceleration factor IPA=2 (Sakitis et al. [21]). However, the total scan time does not decrease proportionally to the IPA factor due to

4

fixed time blocks in the data acquisition process, such as proper time to form T_2^* contrast and imaging encoding time in a single excitation. The through-plane acceleration (TPA) approach, on the other hand, accelerates the image acquisition process by acquiring multiple slices simultaneously in one excitation. Techniques such as the simultaneous multi-slice (SMS) approach can be incorporated with the TPA approach by applying a multiband (MB) radiofrequency (RF) pulse within a reduced repetition time (TR) (Souza et al. [23]; Rowe et al. [19]; Barth et al. [1]; Rowe et al. [17]; Xu and Rowe. [26]). Compared to the IPA approach, the TPA approach significantly improves the efficiency of data acquisition, as the total scan time is reduced by a fraction corresponding to the TPA acceleration factor. While the mSPECS-CAIPIVAT (Xu and Rowe. [26]) framework proposed primarily focused on through-plane acceleration and the feasibility of Bayesian slice separation, the present work extends that framework in several important directions. First, the current study introduces a unified two-dimensional acceleration framework that jointly considers both through-plane and in-plane acceleration. Second, a novel 2D Hadamard phase encoding strategy is incorporated to increase encoding diversity and improve reconstruction stability under aggressive acceleration. Third, the present work systematically investigates the influence of image-shift direction and acceleration factors on activation detection performance using both simulated and experimental fMRI data. Therefore, the objective of this study is not merely to extend the previous Bayesian reconstruction model, but to evaluate how the Bayesian framework behaves under different encoding and acceleration conditions relevant to activation detection in fMRI studies.

To further reduce the total image scan time and achieve the ultimate goal of our study, we introduce a novel SMS image reconstruction technique called "a controlled aliasing in parallel imaging with view angle tilting approach and in-plane acceleration method for multi-coil separation of parallel encoded complex-valued slices" (mSPECS-IPA-CAIPIVAT), which will be presented and discussed. This approach builds upon the mSPECS-IPA method by integrating both TPA and IPA acceleration techniques into a unified 2D acceleration technique (Kociuba [9]). By leveraging 2D acceleration, a higher acceleration factor can be achieved. Several encoding strategies have been proposed to improve slice separation in accelerated SMS imaging, including Controlled Aliasing in Parallel Imaging Results in Higher Acceleration (CAIPIRINHA) and View Angle Tilting (VAT). These techniques introduce controlled spatial shifts in the phase-encoding or readout direction to increase
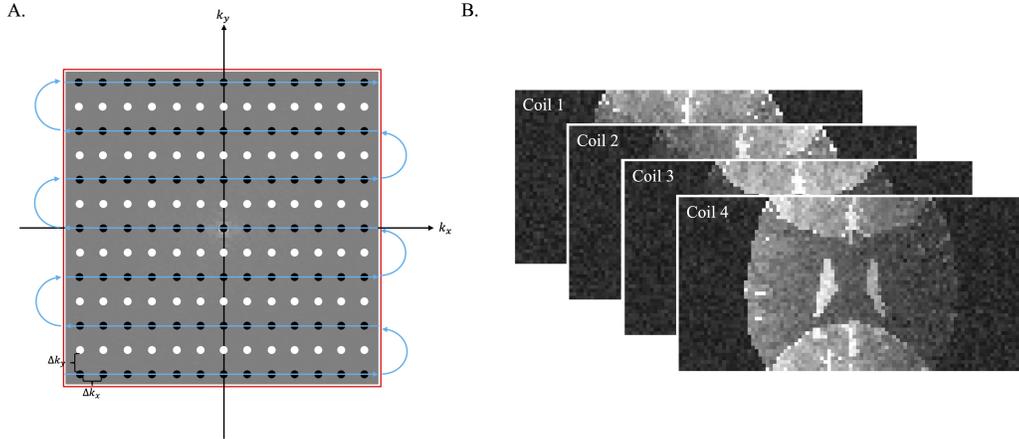
Figure 2: A. The subsampled spatial frequency domain incorporated with IPA approach and the acceleration factor equal to 2. B. The subsampled acquired images from four receriver coils.

encoding diversity and reduce slice leakage in multi-slice acquisitions. In this novel image reconstruction method, we incorporate an image shift technique into the model to reduce the similarity of coil sensitivity information for aliased voxels, thereby improving image reconstruction accuracy.

2. Theory

2.1. The Data Acquiring Process

2.1.1. Image Shift Techniques

As discussed in Section 1.2, the SMS technique enables the concurrent acquisition of multiple brain slice images, reducing the total volume scan time depending on the selected TPA factor. Fig. 3 illustrates both 3D and 2D views of the image acquisition process with four slices and four coils. Unlike single-slice acquisition, multi-slice acquisition results in a short physical distance between aliased images. When applying the SENSE algorithm to reconstruct brain images and capture activity signals, an ill-conditioned matrix problem arises due to the high similarity of coil sensitivity information between closely spaced aliased voxels. Consequently, strong inter-slice signals and anatomical structures from other slices may appear as artifacts in the reconstructed images. To eliminate those stray anatomical artifacts from other slices on the reconstructed brain images, decreasing the similarity of the coil sensitivity information is the primary strategy. Therefore,

6

we introduced the images shift techniques to manually increase the physical distance between aliased images. To assess the performance of the image reconstruction method at high acceleration factors, we define the noise amplification factor, also known as the geometry factor (g-factor), as described in (Setsompop et al. [22]; Welvaert and Rosseel. [25]):

$$g_{SMS} = \frac{SNR_{full}}{SNR_{accelerate}\sqrt{R}}. \tag{4}$$

In Eq. 4, SNR_{full} is the signal-to-noise (SNR) ratio for the reconstructed images from techniques without acceleration factors and image shift techniques, and it can be assessed from the calibration images. $SNR_{accelerate}$ is the SNR value for the reconstructed images with acceleration factors, and the IPA acceleration factor R indicates the omission of spatial frequency data along the phase encoding direction. The closer the value of g_{SMS} is to 1, the better the reconstruction quality of the accelerated method. According to Eq. 4, high similarity of coil sensitivity information induces the high g_{SMS} value, which leads to a reduction of the $SNR_{accelerate}$ for the reconstructed images. Thus, to increase the $SNR_{accelerate}$ value and improve the performance of the novel acceleration technique, three image shift techniques have been incorporated.

In fMRI studies, the brain image can be shifted along three directions: the phase-encoding (PE) direction (vertically in this study), the readout (RO) direction (horizontally in this study), and PE and RO direction concurrently (vertically and horizontally at the same time in this study). To decrease the influence of the geometric properties of the coil sensitivity maps, techniques like "controlled aliasing in parallel imaging results in higher acceleration" (CAIPIRINHA) and "blipped-CAIPIRINHA" (Blipped-CAIPI) provide other possible ways to minimize the influence of the g-factor and maximize the physical distance of the aliased voxels (Breuer et al. [2]; Setsompop et al. [22]). The CAIPIRINHA approach can shift the images along the PE direction by modulating the phase for each line in the k-space and imparting each line with a specific phase. Applying a unique phase modulation amount to each slice in the aliased image-acquiring process increases the physical distance between the aliased voxels. Therefore, the independence of coil sensitivity for each slice will increase, and the influence of the g-factor for each excitation will be minimized. Moreover, to shift the brain image along the RO direction, a technique like the view angle tilting (VAT) approach applies compensation gradients to the slice selection direction to correct the chemical-shift artifacts in the image scanning process (Cho et al. [3]; Kim et
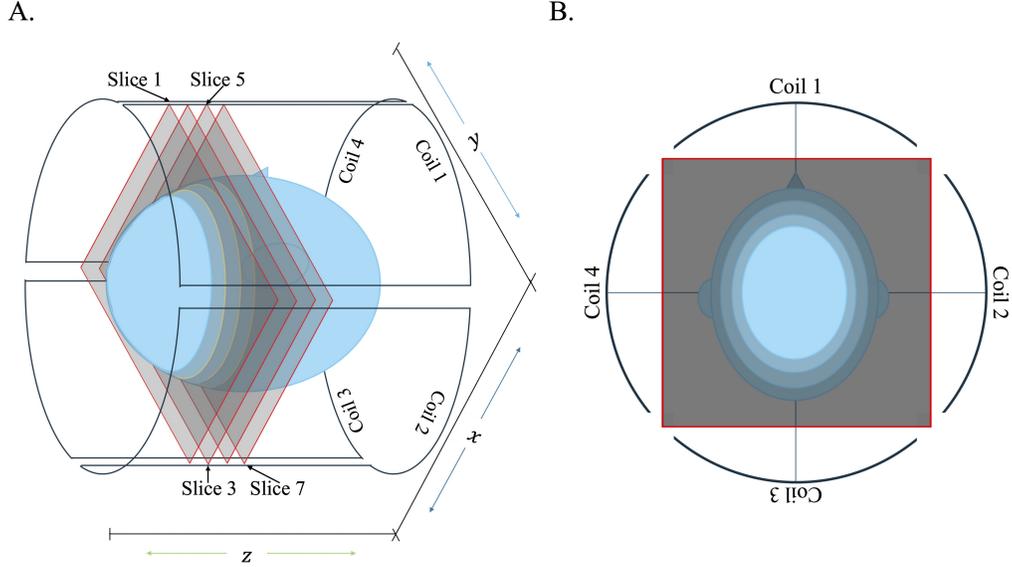
Figure 3: A. The 3D view of SMS technique with four slices and four coils acquisition process at one excitation. B. The 2D view for the same process with four slices and four coils.

al. [11]). The distance shifted along the RO direction is related to the view angle θ in the data acquisition process. The CAIPIRINHA and the VAT technique can be combined, and thus the study "multislice CAPIPRINHA using view angle tilting technique" (CAIPIVAT) proposed (Jungmann et al. [8]; Kim et al. [10]). Through this technique, the field-of-view (FOV) can be shifted along the PE and RO direction by applying different amounts of phase modulation to each line in the k-space and the compensation gradients on the slice selection direction together for each excitation. The GRE-EPI pulse sequence of the CAIPIRINHA, Blipped-CAIPI, and CAIPIVAT models could be investigated according to their respective references. Although the Blipped-CAIPI method compliments the VAT and the Hadamard encoding techniques, to further increase the diversity of the information in the image acquisition process, we introduced the 2D Hadamard phase encoding technique and discussed the combination with CAIPIRINHA, VAT and CAIPIVAT technique. Fig. 4 shows the k-space for CAIPIRINHA, VAT and CAIPIVAT techniques along the reconstructed brain images after the inverse Fourier transform.
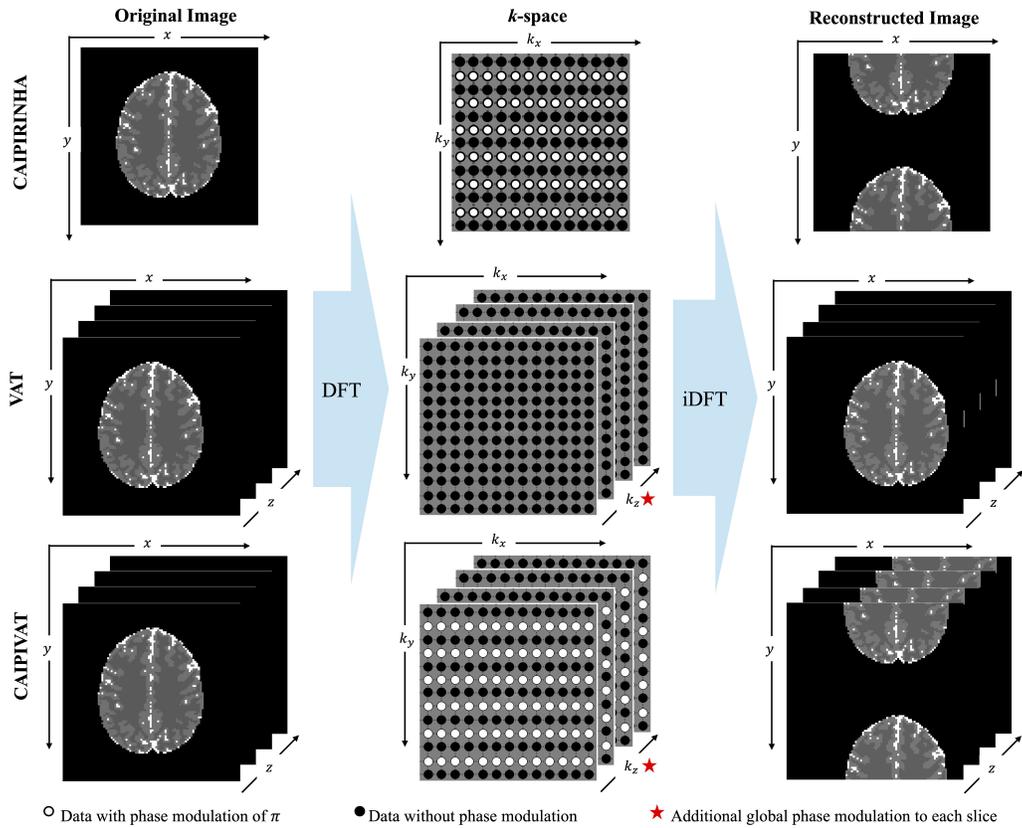
Figure 4: Top row: the image shift process corresponding to the CAIPIRINHA technique (shifted vertically). Middle row: the image shift process corresponding to the VAT technique (shifted horizontally). Bottom row: the image shift process corresponding to the CAIPIVAT technique (shifted vertically and horizontally).

2.1.2. 2D Hadamard Phase Encoding

The traditional Hadamard encoding technique is a well-developed volume-image method and widely used in fMRI studies (Souza et al. [23]). The conventional magnetic resonance (MR) imaging techniques have been limited by the size of the matrix for the acquired aliased images. The traditional Hadamard phase encoding method allows the increment of the size of the acquired aliased image matrix by aliasing in both frequency and phase encoding dimensions. With the support of this simultaneous binary-encoded technique, the TR will decrease, and the SNR ratio will improve. The Hadamard matrix is given by:

$$H_{2^n} = \begin{bmatrix} H_{2^{n-1}} & H_{2^{n-1}} \\ H_{2^{n-1}} & -H_{2^{n-1}} \end{bmatrix} = H_2 \otimes H_{2^{n-1}}, \text{where } H_1 = \begin{bmatrix} 1 \end{bmatrix}, H_2 = \begin{bmatrix} 1 & 1 \\ 1 & -1 \end{bmatrix}, \tag{5}$$

where $\otimes$ denotes the Kronecker product. It is an orthogonal and full rank matrix with elements of either +1 or -1. The Hadamard phase encoding technique can be applied not only to through-plane imaging scenario but also to in-plane imaging scheme. The entire FOV can be divided into various regions of interest by applying Walsh functions during the pre-encoding section to define the frequency profile that the Hadamard pulses must follow (Fletcher et al. [5]).

In this study, since the TPA approach and the IPA approach are combined to further decrease the total image scan time, and the image shift techniques are incorporated to decrease the influences of the geometry properties, we introduce a novel 2D Hadamard phase encoding technique to our approach. The novel 2D Hadamard phase encoding technique is developed and based upon the Hadamard phase encoding technique with elements of either +1 or -1. However, different from the traditional Hadamard phase encoding technique, in order to guarantee the orthogonality property for each aliased image, different 2D Hadamard coefficients will be assigned to different segments for different slices. Fig. 5 shows the 2D Hadamard phase encoding aliasing coefficient for $N_s = 2$ and $N_s = 4$ scenarios, where N_s is the number of aliased slices for each excitation. First, for each excitation or each TR, the through-plane Hadamard coefficient will be assigned to different slices. Second, for each segment of each slice, the in-plane Hadamard coefficient will be assigned to a different excitation. To maintain the orthogonality property for each segment of each slice, the in-plane Hadamard coefficient starts from the second column of the Hadamard coefficient for the first excitation.
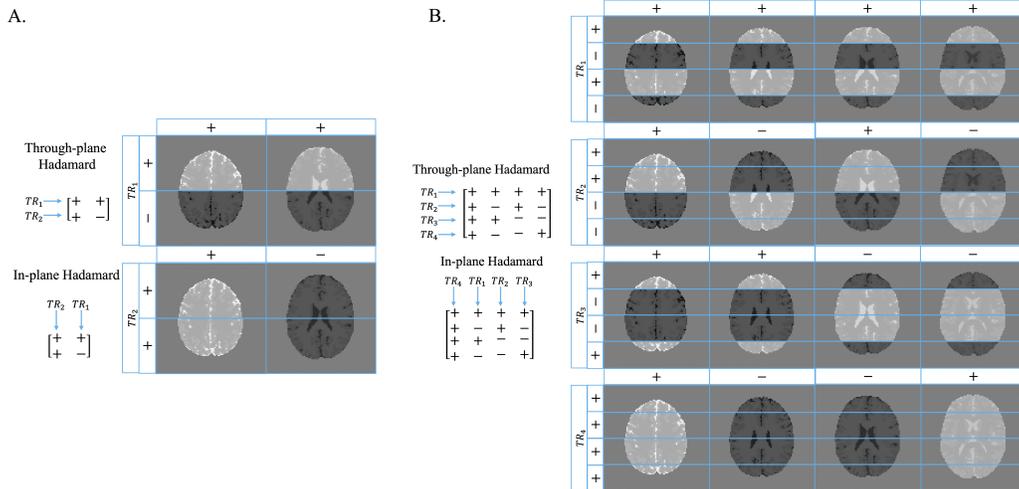
10

Figure 5: A. The 2D Hadamard phase encoding coefficient for $N_s = 2$. B. The 2D Hadamard phase encoding coefficient for $N_s = 4$.

At the last TR of the cycle, the in-plane Hadamard coefficient is the first column of the Hadamard matrix. Finally, the 2D Hadamard coefficient will be the product of the through-plane and in-plane Hadamard coefficient for each segment of each slice and each excitation. The size of the in-plane and through-plane Hadamard coefficient matrix is equal to the number of aliased slices, N_s, for each excitation.

2.1.3. The Combination of Image Shift Techniques and 2D Hadamard Phase Encoding

To accomplish the goal of decreasing the coil sensitivity information similarity of aliased voxels, and thus decreasing the influence of the g-factor, we combined the image shift techniques and the 2D Hadamard phase encoding technique together. Fig. 6 shows the image shift scenario corresponding to different SMS techniques for the first 4 TRs along with the 2D Hadamard coefficients for each segment of the slices under the circumstance with $N_s = 4$. Compared with the mSPECS-IPA method (Fig. 6A), the other three methods are incorporated with different image shift directions and amount for each slices and each excitation. Fig. 6B shows the image shift scenario along with the 2D Hadamard coefficients incorporating with the mSPECS-IPA-CAIPIRINHA method. For each slice within each TR, a $\Delta y = (l-1)FOV/N_s$ of in-plane image shift on the verti-

Figure 6: The voxel aliasing scenario for the first 4 TRs with $N_s = 4$ circumstance incorporating with A. mSPECS-IPA image shift technique, B. mSPECS-IPA-CAIPIRINHA technique, C. mSPECS-IPA-VAT technique, and D. mSPECS-IPA-CAIPIVAT technique.

cal direction will be imparted, where $l = 1, \ldots, N_s$. For each excitation, a $\Delta y = (m-1)FOV/N_s$ of in-plane image shift on the vertical direction will be imparted, where $m = 1, \ldots, N_s$. Thus, with the in-plane and the through-excitation CAIPIRINHA image shift, the voxel aliasing scenario at $TR_{N_s} + 1$ will be identically same as aliasing scenario at TR_1. Fig. 6C shows the image shift scenario along with the two-dimensional Hadamard coefficients incorporating with the mSPECS-IPA-VAT method. Unlike the mSPECS-IPA-CAIPIRINHA method, the mSPECS-IPA-VAT method only shift the image along the horizontal direction. Thus, for each excitation and each slice, no image shift occurs along the vertical direction, but a modest amount of image shift will be applied for each slice and each excitation along the hor-

12

izontal direction. Fig. 6D shows voxel aliasing scenario incorporated with the mSPECS-IPA-CAIPIVAT method. Since the mSPECS-IPA-CAIPIVAT method is combining the principle idea of mSPECS-IPA-CAIPIRINHA and mSPECS-IPA-VAT method together, the image shift will occur along the vertical and the horizontal direction. For each slice within each excitation, a $\Delta y = (l-1)FOV/N_s$ amount of the image shift along the vertical direction, where $l = 1, \ldots, N_s$, and the amount of the image shift technique corresponding to the VAT technique along the horizontal direction will be imparted. Moreover, for each excitation, a $\Delta y = (m-1)FOV/N_s$ of image shift will be imparted along the vertical direction, where $m = 1, \ldots, N_s$. In real-world volume image acquisition, the 2D Hadamard phase-encoding technique should be applied before the image shift techniques (Fletcher et al. [5]). A careful design of the Hadamard pre-encoding process is necessary to ensure the orthogonality of the 2D Hadamard aliasing coefficients. Comparing these four image shift techniques, the overlapping area between summed slices are decreasing from the mSPECS-IPA method to the mSPECS-IPA-CAIPIVAT method. However, since the novel proposed SMS technique is aiming at combining TPA and IPA technique together, thus, making the voxel aliasing scenario clear after the IPA technique is another vital process to discuss in this paper.

Fig. 7 displays the voxel aliasing scenario after the IPA aliasing technique for mSPECS-IPA, mSPECS-IPA-CAIPIRINHA, mSPECS-IPA-VAT, and mSPECS-IPA-CAIPIVAT technique under the circumstance with $N_s = 4$. In Fig. 7, those dots in the same color indicating voxels are aliased together. From the top model to the bottom model, the physical distance between aliased voxels increases, leading to reduced coil information similarity and, consequently, a lower g-factor. Moverover, comparing the mSPECS-IPA and the mSPECS-IPA-CAIPIRINHA method, after the IPA acceleration technique, the mSPECS-IPA-CAIPIRINHA has the more complex aliasing artifacts and the overlapping area is larger than the mSPECS-IPA method especially at the center part of the acquired images. Comparing the bottom two methods, mSPECS-IPA-VAT and the mSPECS-IPA-CAIPIVAT technique, the similar conclusion can be made. In this work, the combination of image shift techniques and 2D Hadamard phase encoding was not implemented experimentally, as this is a methodological study. Instead, we utilized fully sampled k-space data, and the slices were artificially Hadamard encoded and aliased.

13

Figure 7: The voxel aliasing scenario with $N_s = 4$ for mSPECS-IPA, mSPECS-IPA-CAIPIRINHA, mSPECS-IPA-VAT and mSPECS-IPA-CAIPIVAT technique.

2.2. A Single Aliased Voxel

Given an excitation δ in the fMRI time series, we define $IS_{\delta,z}$ notation indicating the image shift pattern for the zth slice and the δth TR, corresponding to one of the mSPECS-IPA, mSPECS-IPA-CAIPIRINHA, mSPECS-IPA-VAT and the mSPECS-IPA-CAIPIVAT technique, and it follows the definition in Section 2.1.1. Thus, for a single aliased voxel at the location (x, y) of the acquired aliased images with TPA and IPA acceleration techniques, corresponding to the 2D Hadamard coefficients at time point δ, measured at jth coil, is defined as the summation equation:

$$a_{j,\delta} = \sum_{k=1}^{IPA} \sum_{z=1}^{N_s} H_{\delta,z,k} S_{IS_{\delta,z},k} \beta_{IS_{\delta,z},k} + \varepsilon_{j,\delta}. \tag{6}$$

In Eq. 6, the acquired aliased voxel value $a_{j,\delta}$ is a complex-valued data with real and imaginary component, $a_C = a_R + ia_I$, and parameter k is the IPA

14

indicator. The 2D Hadamard coefficient, $H_{\delta,z,k}$, is a real-valued orthogonal matrix corresponding to the δth excitation, zth slice and the kth IPA process, and it strictly follows the definition of the 2D Hadamard phase encoding in Section 2.1.2. All of the element of the $H_{\delta,z,k}$ coefficient matrix is either $+1$ or -1. The coil sensitivity information matrix, $S_{IS_{\delta,z},k}$, is a complex-valued data point with real and imaginary component, $S_C = S_R + iS_I$, corresponding to the kth IPA process and the image shift process at δth excitation and zth slice. The true voxel value, $\beta_{IS_{\delta,z},k}$, is a complex-valued data point with real and imaginary component, $\beta_C = \beta_R + i\beta_I$, corresponding to the kth IPA process and the image shift process at δth excitation and zth slice. The measurement error, $\varepsilon_{j,\delta}$, is also a complex-valued data point with real and imaginary component, $\varepsilon_C = \varepsilon_R + i\varepsilon_I$, corresponding to the δth time point and jth coil. Moreover, the real and imaginary component of measurement error is specified to be a normal distribution with mean $E(\varepsilon_R) = E(\varepsilon_I) = 0$ and variance $var(\varepsilon_R) = var(\varepsilon_I) = \sigma^2$.

Considering the acquired aliased voxel in Eq. 6 across total N_c coils, N_α time points and the N_s slices in the whole fMRI time series, the real-valued isomorphic representation of Eq. 6 can be expressed similar to Eq. 1:

$$a = X_A\beta + \varepsilon. \tag{7}$$

In Eq. 7, $a = [a_R; a_I]$ is a real-valued vector with dimension $2N_cN_\alpha \times 1$. The real-valued aliasing matrix $X_A = [(X_A)_R, -(X_A)_I; (X_A)_I, (X_A)_R]$ is known prior information including the 2D Hadamard coefficients and the coil sensitivity information across the N_c coils, N_α time points and the N_s slices. Thus, the dimension of the aliasing matrix X_A is $2N_cN_\alpha \times 2N_s$. For the δth excitation, the known aliasing matrix $(X_A)_\delta$ across N_c coils and N_s slices is defined as:

$$(X_A)_\delta = \left[H_{\delta,1}\begin{pmatrix} S_{1,1} \\ \vdots \\ S_{N_c,1} \end{pmatrix}, \ldots, H_{\delta,N_c}\begin{pmatrix} S_{1,N_s} \\ \vdots \\ S_{N_c,N_s} \end{pmatrix} \right]. \tag{8}$$

Across the N_α excitations, the Eq. 8 can be expressed as:

$$X_A^{'} = \left[(X_A)_1^{'}, \ldots, (X_A)_{N_\alpha}^{'} \right]. \tag{9}$$

The true voxel value in Eq. 7, $\beta = [\beta_R; \beta_I]$, is a vector we want to estimate, with dimension $2N_s \times 1$. The measurement error in Eq. 7, $\varepsilon = [\varepsilon_R; \varepsilon_I]$ has the

same dimension as the a vector. The real and imaginary component of the measurement error is specified to be normal distributed with mean $E(\varepsilon) = 0$ and covariance $cov(\varepsilon) = \sigma^2 I_{2N_c N_\alpha}$, where $I_{2N_c N_\alpha}$ is the identity matrix.

Thus, in order to separate the aliased images and estimate the true voxel value for each slice, the maximum likelihood estimation in Eq. **??** can be applied and the estimated voxel value, $\hat{\beta}_{MLE}$, can be calculated by:

$$\hat{\beta}_{MLE} = \left(X'_A X_A \right)^{-1} X'_A a. \tag{10}$$

Moreover, the covariance of the voxel value $\hat{\beta}$, can be estimated by:

$$cov(\hat{\beta}_{MLE}) = \sigma^2 \left(X'_A X_A \right)^{-1}. \tag{11}$$

According to the methodology of the combination of image shift techniques and the 2D Hadamard phase encoding technique, the novel proposed SMS method accelerates the image acquiring process along the TPA and the IPA dimension. However, the relative short scan time leads to less data information collected during the image acquiring process compared with the traditional imaging technique without acceleration techniques. Furthermore, it also leads to an ill-conditioning of the designed aliasing matrix which will cause failure to calculate the inverse of $X'_A X_A$. Thus, coming up with a technique that is capable to fix the ill-condition designed matrix problem and hence calculate the inverse problem is the next priority. In this study, we introduce the bootstrap sampling technique along with the artificial aliasing of the calibration images technique to solve this problem. By applying these two techniques into the novel image shift SMS technique, the designed aliasing matrix is made to be full rank and invertible and the inter-slice signal leakage can be eliminated.

2.3. The Bootstrap Sampling and Artificial Aliasing of Calibration Images

The Bayesian reconstruction model forms the conceptual foundation of this study. Unlike conventional SMS reconstruction techniques that provide deterministic voxel estimates, the proposed framework models the reconstruction problem probabilistically and incorporates calibration information through structured prior distributions. Based on the discussion in the previous sections, to make the designed aliasing matrix to be full rank and invertible, slices information from the calibration images can be utilized as the reference information. The bootstrap sampling technique is a widely used

Figure 8: The the 2D Hadamard aliasing coefficients for acquired aliased slices (red box) and the artificial aliased calibration slices (blue box) for the first 4 TRs with $N_s = 4$.

tool which can decrease the correlation induced by the image separation process and eliminate the inter-slice signal leakage. In the image separation process, for each excitation, the bootstrap sampling technique will be applied to the calibration images. The bootstrapping size for each excitation is related to the TPA factor, which is equal to the number of aliased slices for

each excitation and the IPA factor. Thus, for each excitation in the fMRI time series, $N_s R$ bootstrapped sampled slices will be randomly chosen from the fully sampled calibration image time series. The randomly chosen slices will be averaged and the mean calibration images will be utilized for the artificial aliasing process. Although this results in a slightly larger variance than averaging all calibration images, it eliminates correlation between unaliased slices.

For each excitation, the same image shift pattern will be applied to both acquired aliased images and the artificial aliased calibration images. But different 2D Hadamard aliasing coefficient matrix will be applied to acquired 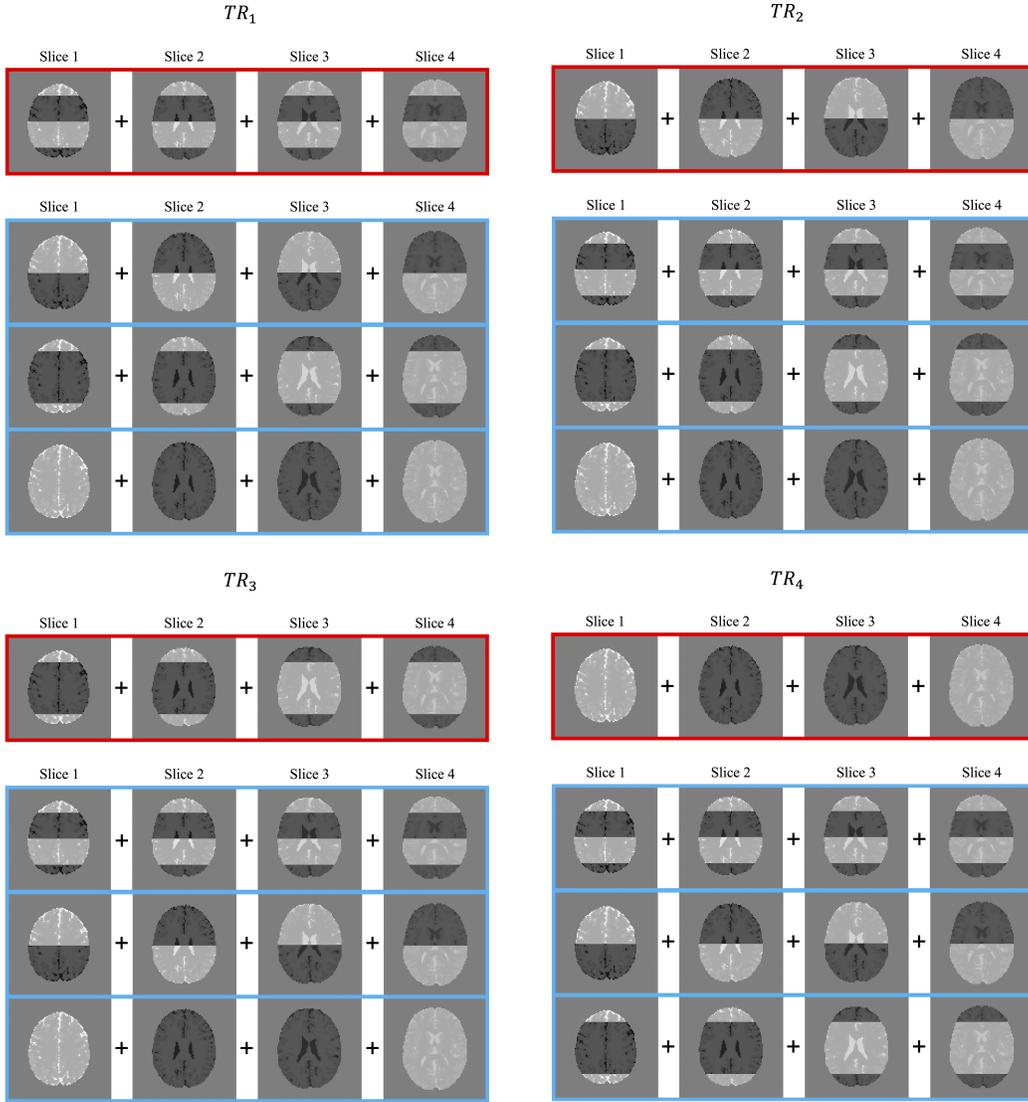aliased images and the artificial aliased calibration images. Fig. 8 shows the 2D Hadamard aliasing coefficient for acquired aliased slices (red box) and the artificial aliased calibration slices (blue box) for the first 4 TRs with $N_s = 4$. For each segment of each slice, the white part means the Hadamard coefficient is +1, and the black part means the Hadamard coefficient is -1. Moreover, the 2D Hadamard aliasing coefficient for acquired aliased slices and artificial aliased calibration slices at time point TR_{N_s+1} will be identical as TR_1. Based on the 2D Hadamard aliasing coefficients for acquired aliased slices and the artificial aliased calibration slices, for each excitation, $N_s - 1$ combinations of 2D Hadamard aliasing coefficient remain for the artificial aliasing process.

Similar to Eq. 7, for a single excitation, a single voxel, ν, from the artificial aliasing calibration aliased slices located at (x, y) across N_s slices, measured through N_c coils can be expressed as:

$$\nu = C\bar{\nu} = C_A \mu + C\eta. \tag{12}$$

In Eq. 12, the artificial aliased voxel value, $\nu = [\nu_R; \nu_I]$, is a vector with real and imaginary component and dimension $2N_s N_c(N_s - 1) \times 1$. The mean bootstrap sampled voxel, $\bar{\nu} = [\bar{\nu}_R; \bar{\nu}_I]$, is a vector with dimension $2N_s \times 1$. The true calibration voxel value, $\mu = [\mu_R; \mu_I]$, and the measurement error, $\eta = [\eta_R; \eta_I]$, have the same dimension with the mean bootstrap sampled voxel vector. Moreover, the mean of the measurement error is $E(C\eta) = 0$ and covariance is $cov(C\eta) = \tau^2 I_{2N_s N_c(N_s-1)}$ where $I_{2N_s N_c(N_s-1)}$ is the identity matrix. If the bootstrap sampling technique is not incorporated, *i.e.* the same calibration images are used in the model, then the covariance of the measurement error is $\tau^2 = 0$, thus a correlation between the reconstructed slices is induced solely by the image separation process. This is a very important

18

result. However, with the assistance of the bootstrap sampling technique, $\tau^2 = \sigma^2$, and the covariance of the measurement error of the calibration image is $cov(C\eta) = \sigma^2 I_{2N_s N_c(N_s-1)}$. A small trade-off of increased variance for an elimination of correlation as shown later.

The artificial aliasing matrix, C_A in Eq. 12, is a known prior information including the 2D Hadamard coefficients for the artificial aliasing slices and the coil sensitivity information across N_c coils, N_α time points and N_s slices. Thus, the dimension of the artificial aliasing matrix, C_A, is $2N_s N_c(N_s - 1) \times 2N_s$. For the δth excitation, the known artificial aliasing matrix $(C_A)_\delta$ across N_c coils and N_s slices is defined as:

$$(C_A)_\delta = \left[\overline{H_{\delta,1}} \begin{pmatrix} S_{1,1} \\ \vdots \\ S_{N_c,1} \end{pmatrix}, \ldots, \overline{H_{\delta,N_c}} \begin{pmatrix} S_{1,N_s} \\ \vdots \\ S_{N_c,N_s} \end{pmatrix} \right]. \tag{13}$$

The notation $\overline{H}$ indicates the remaining 2D Hadamard aliasing coefficient for each excitation after removing the 2D Hadamard aliasing coefficient for the acquired aliased images. Across the N_α excitations, the Eq. 13 can be expressed as:

$$C_A' = \left[(C_A)_1', \ldots, (C_A)_{N_\alpha}' \right]. \tag{14}$$

2.4. The Likelihood, Prior, and Joint Distribution

As discussed in Section 1.1, the acquired aliased voxel values across the whole brain image are independent and identically distributed and the measurement error for each acquired aliased voxel is specified to be Gaussian distributed. Thus, the likelihood distribution (Eq. **??**) of the acquired aliased voxel is:

$$P(a \mid X_A, \beta, \sigma^2) \propto (\sigma^2)^{-\frac{2N_c N_\alpha}{2}} \exp\left[-\frac{1}{2\sigma^2} (a - X_A\beta)'(a - X_A\beta) \right]. \tag{15}$$

Following the methodology of the Bayesian approach, the voxel value from calibration images can be utilized as prior information. Moreover, in Section 1.1 the voxel value, β, is specified to have a normal prior distribution. Therefore, the prior distribution of the voxel value $\beta \sim N(\mu, \sigma^2(C_A'C_A)^{-1})$:

$$P(\beta \mid C_A, \mu, \sigma^2) \propto (\sigma^2)^{-\frac{2N_s N_r}{2}} \exp\left[-\frac{1}{2\sigma^2} (\beta - \mu)'(C_A'C_A)(\beta - \mu) \right]. \tag{16}$$

19

Moreover, in Section 1.1, the variance of the measurement error, σ^2 is specified to have an inverse gamma prior distribution:

$$P(\sigma^2 \mid \lambda, \delta) \propto (\sigma^2)^{-(\lambda+1)} \exp\left[-\frac{\delta}{\sigma^2}\right], \tag{17}$$

where hyperparameters μ, λ and δ are assessed from the calibration images. The posterior distribution of the voxel value, β, and the variance of the measurement error, σ^2, follows the joint distribution as Eq. 3:

$$P(\beta, \sigma^2 \mid \cdot) \propto P(a \mid X_A, \beta, \sigma^2) P(\beta \mid C_A, \mu, \sigma^2) P(\sigma^2 \mid \lambda, \delta). \tag{18}$$

2.5. Hyperparameters Assessment

Before applying the image acquisition process of this proposed novel SMS model, a time series of calibration images will be collected first. The calibration image time series will be acquired through the traditional fMRI technique, and unlike the novel SMS model incorporating with different image shift techniques and 2D Hadamard aliasing coefficient. The calibration image time series is acquired without any image shift techniques or aliasing coefficient, no task experiment will be executed during this time series. As discussed in Section 2.4, the calibration images can be utilized as prior information, hence the unknown hyperparameters can be assessed from calibration time series. In Eq. 18, the acquired aliasing matrix X_A and the artificial aliasing matrix C_A are known prior information that we do not need to assess from the calibration image time series. The hyperparameters μ, λ, and δ, on the other hand, need to be assessed from the calibration image time series. As discussed in Section 2.3, the hyperparameter μ is the averaged voxel value after the bootstrap resampling process. For each excitation in the time series, N_s brain images will be randomly chosen from the fully sampled calibration images and averaged to assess the voxel hyperparameter value $\mu = \bar{\nu}$. The shape parameter λ and the scale parameter δ from inverse gamma distribution in Eq. 17, also need to be assessed from the calibration image time series. After the bootstrap resampling process, the sample noise variance σ_0^2 can be estimated from the calibration image time series. Thus, the shape parameter can be assessed by $\lambda = n_0$, and the scale parameter can be assessed by $\delta = (n_0 - 1)\sigma_0^2$, where n_0 is the number of calibration images and σ_0^2 is sample noise variance.

2.6. The Posterior Estimation

According to the discussion in Section 1.1, Section 2.4, and Section 2.5, the joint distribution (Eq. 18) of the likelihood distribution of acquired aliased (Eq. 15), the prior distribution of the voxel value β (Eq. 16), and the prior distribution of the noise variance σ^2 (Eq. 17) can be calculated after algebra:

$$P(\beta, \sigma^2 \mid \cdot)$$
$$\propto (\sigma^2)^{-\frac{p}{2}} \exp\left[-\frac{1}{2\sigma^2}((\beta - \hat{\beta}_{MPM})'(X_A'X_A + C_A'C_A)(\beta - \hat{\beta}_{MPM}) + w)\right],$$
$$\tag{19}$$

where $p = 2N_c N_\alpha + 2N_s N_r - 2\lambda - 2$, and $w = a'a + \mu'C_A'C_A\mu - (X_A'a + C_A'C_A\mu)'(X_A'X_A + C_A'C_A)^{-1}(X_A'a + C_A'C_A\mu) + 2\delta$. Moreover, as discussed in Section 1.1, the posterior distribution of the voxel value, β, and the noise variance, σ^2 can be integrated through the MPM technique. Therefore, the marginal posterior distribution of estimate voxel value β after integration is a student-t distribution $\beta \sim t(\nu^\star)$:

$$f(\beta \mid \cdot) \propto \left\{1 + \frac{1}{\nu^\star}(\beta - \hat{\beta}_{MPM})'\left[\frac{(X_A'X_A + C_A'C_A)}{\tau^2}\right](\beta - \hat{\beta}_{MPM})\right\}^{\frac{\nu^\star + 1}{2}},$$
$$\tag{20}$$

with $\nu^\star = p - 1$ and $\tau^2 = w/\nu^\star$. The marginal posterior mean (MPM) for $\hat{\beta}$ after integration is:

$$E(\beta \mid \cdot) = \hat{\beta}_{MPM} = (X_A'X_A + C_A'C_A)^{-1}(X_A'a + C_A'C_A\mu). \tag{21}$$

In Eq. 21, the matrix $C_A'C_A$ acts as a regularizer for the matrix inverse to improve the condition of the equation. Since the true voxel value from calibration images is close to the true voxel value from acquired aliased images, Eq. 21 leads to $E(\beta \mid \cdot) = \beta$. The marginal posterior covariance of the voxel value $\hat{\beta}$ is:

$$cov(\beta \mid \cdot) = \frac{\nu^\star}{\nu^\star - 2}\tau^2(X_A'X_A + C_A'C_A)^{-1}, \tag{22}$$

the separated voxel values are uncorrelated, meaning that there will not be signal leakage or correlation induced between slices.

Moreover, the marginal posterior distribution of σ^2 after integration is an inverse gamma distribution, $\sigma^2 \sim IG(\gamma, w/2)$:

$$f(\sigma^2 \mid \cdot) \propto (\sigma^2)^{-\frac{p}{2}-1} \exp\left[-w/(2\sigma^2)\right], \tag{23}$$
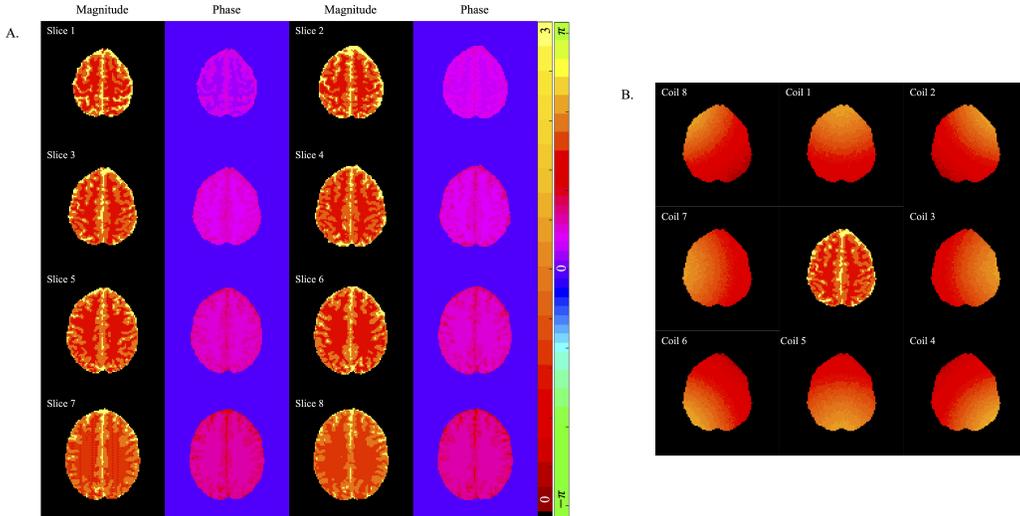
21

Figure 9: A. The magnitude and phase for the true noiseless simulated axial brain images with $N_s = 8$. B. The magnitude of the simulated sensitivity coils for slice 3 with $N_c = 8$.

with $\gamma = (p-1)/2$. The MPM of the noise variance σ^2 is:

$$E(\sigma^2 \mid \cdot) = \frac{w/2}{\gamma}, \tag{24}$$

and the marginal posterior variance of the noise variance is:

$$var(\sigma^2 \mid \cdot) = \frac{w/2}{(\gamma-1)^2(\gamma-2)}. \tag{25}$$

3. FMRI Data

3.1. Simulated FMRI Data

The proposed novel image shifted SMS technique was first applied to simulated fMRI data. The reconstructed brain images were compared through the mSPECS-IPA model (non image shift technique), the mSPECS-IPA-CAIPIRINHA model (image vertically shift), the mSPECS-IPA-VAT model (image horizontally shift) and the mSPECS-IPA-VAT model (image vertically and horizontally shift). Our goal is to improve the efficiency of the image acquisition process while simultaneously determining which image shift direction provides the best reconstruction results.

The simulated fMRI time series mimicks our right hand finger tapping experimental data with the total number of TR (repetition time) = 510. According to the methodology of the image shifted SMS technique, two separate fMRI time series are simulated: the acquired fMRI time series and the calibration fMRI time series. The acquired fMRI time series was simulated using the mSPECS-IPA, mSPECS-IPA-CAIPIRINHA, mSPECS-IPA-VAT, and mSPECS-IPA-CAIPIVAT models, as different image shift directions were applied. The calibration fMRI time series, however, was simulated without any image shift technique or acceleration techniques. The calibration images were reconstructed by applying SENSE model. Since the simulated fMRI time series mimics an *in vivo* experiment, the first 20 repetition times are omitted to achieve a steady magnetic field, leaving a total number of $TR = 490$. In the simulated fMRI time series, total $N_s = 8$ axial brain images were included in the acquired simulated fMRI time series and the calibration simulated fMRI time series. In the calibration simulated time series, no simulated task block were added to the brain images. On the other hand, the simulated task blocks were added to the left motor cortex of the top 4 brain images. The simulated task blocks were added according to the real-world right hand finger tapping experiment with 15 TRs off and 15 TRs on for 16 epochs, and the first 20 TRs and last 10 TRs off. The contrast-to-noise ratio and the signal-to-noise ratio we choose also mimick our fMRI experiment with $SNR = 50$ and $CNR = 0.5$. Thus, the mean magnitude added to each simulated slice is 4 and the mean magnitude added to the simulated task blocks is 0.04. The region-of-interest (ROI) was defined based on the reconstructed calibration images used in the experimental dataset. Specifically, voxels showing strong signal intensity in the reconstructed calibration images within the expected motor cortex region were selected as the reference location. The same spatial region was then used to define the ROI in the simulated datasets in order to maintain consistency between the simulated and experimental analyses. This ROI definition therefore reflects both anatomical location (motor cortex) and functional relevance for the finger-tapping task. Moreover, Gaussian distributed noise $N(0, 0.0064)$ was added to each slice of the simulated acquired fMRI time series and the simulated calibration fMRI time series. To mimic phade differences between slices, different phase angles from 5° to 40° with 5° intervals were added to each slice. Different phase angles were also added to different brain tissue types with 7.5° for white matter (WM), 15° for gray matter (GM), and 22.5° for cerebral spinal fluid (CSF).

In order to investigate the performance of different models with different acceleration factors, the IPA factor we used in the simulated acquired fMRI dataset is $R = 2$, and different TPA factors were incorporated in the experiment with $TPA = 2$, $TPA = 4$, and $TPA = 8$. Thus, the net acceleration factor is the product of the IPA factor and the TPA factor with $NET = 4$, $NET = 8$, and $NET = 16$. For the $TPA = 2$ scenario, the slice aliasing scenario is: packet 1: slice 1 and slice 5, packet 2: slice 2 and slice 6, packet 3: slice 3 and slice 7, packet 4: slice 4 and slice 8. For $TPA = 4$ scenario, the slices aliasing scenario is: packet 1: even slices, packet 2: odd slices. For $TPA = 8$ scenario, all slices are aliased in one packet.

Fig. 9A shows the true noiseless magnitude and phase for each slice of simulated axial brain images with $N_s = 8$. A total number of $N_c = 8$ channel sensitivity coils were simulated and applied according to the real right hand finger tapping experiment. Fig. 9B shows the magnitude and position for each coil corresponding to slice 3. The mean magnitude for each simulated coil is 0.95, and to increase the difference between each coil, different phase angles were added to the simulated coils from 0° to 17.5° with 2.5° intervals.

The simulated SMS data used in this study were generated through artificial aliasing of fully sampled k-space data. While this approach allows controlled investigation of image shift direction, Hadamard encoding, and Bayesian regularization effects, it does not reproduce all characteristics of experimental SMS acquisitions, such as slice dependent phase errors, eddy current effects, and complex noise correlations. Therefore, the simulation results are intended to provide mechanistic insights into the reconstruction behavior rather than a definitive performance comparison against established SMS reconstruction methods such as Slice-GRAPPA or Split Slice-GRAPPA, which have been extensively validated using in vivo multiband acquisitions (Cauley et al. [4]; Setsompop et al. [22]).

3.2. Experimental FMRI Data

A right-handed finger tapping fMRI experiment for a single object was executed through a 3.0 T General Electric Signa LX MRI scanner. The flip angel was 90° and the acquisition bandwidth is 125 kHz in this experiment. The slice thickness for the axial brain images was 2.5 mm. A total of nine slices were scanned. In this experiment, an 8 channel receiver head coil was utilized with dimension 96×96 for a 24 cm full field-of-view, with the phase encoding direction from posterior to anterior. It should be noted that the 8

channel receiver coil used in this experiment provides limited spatial sensitivity variation for high through-plane acceleration factors. In current SMS fMRI practice, 32 channel or higher receiver arrays are typically employed to support robust slice separation. Consequently, the present dataset is not intended to demonstrate optimal SMS image quality, but rather to evaluate relative reconstruction behavior under constrained coil geometry. In our right-handed finger tapping fMRI experiment, two fMRI time series were acquired: a non-task calibration time series and a task time series. The right-handed finger tapping experiment was designed with an initial 20 TRs off rest, followed by 15 TRs off and 15 TRs on for 16 epochs, and the final 10 TRs of rest, resulting in a total 510 TRs for the task time series. The same echo time (TE) was applied to both fMRI time series, consisting of three segments. The calibration dataset was acquired with the same number of time points as the fMRI task acquisition to ensure stable parameter estimation and consistent comparisons across reconstruction models. Consequently, the calibration acquisition time is approximately equal to the task acquisition time in this experimental setup. The TE for the first 10 TRs and the last 490 TRs was 42.7 ms. From the 11th to the 20th time point, the TE values were 42.7 ms, 45.2 ms, 47.7 ms, 50.2 ms, and 52.7 ms, and this sequence was repeated twice. The first 20 TRs of the task time series were disregarded to achieve a steady magnetic field of the scanner, resulting in last 490 TRs of the task time series were applied to the novel proposed model.

In our right-handed finger-tapping fMRI experiment, aliased task images were not acquired experimentally, as this is a methodological study and so we can evaluate various acceleration factors with the same data. Since the dimension of the 2D Hadamard aliasing coefficient must be a power of two, only eight slices were used in the proposed image-shifted SMS techniques, with the most interior axial brain slice disregarded. Instead, the task images were artificially aliased from the fully acquired task time series, following a procedure similar to that used for generating simulated aliased task images. The artificially aliased task images for each model were primarily generated using different image shift techniques and 2D Hadamard encoding coefficients. The artificially aliased subsampled k-space data were obtained by skipping every other line in the fully sampled k-space of the summed images after applying the Fourier transform. The aliased task images were then reconstructed from the subsampled k-space using the inverse Fourier transform.

The last $N_{cal} = 40$ fully sampled non-task calibration images were used to assess the hyperparameter. The same acceleration factors from the simulated
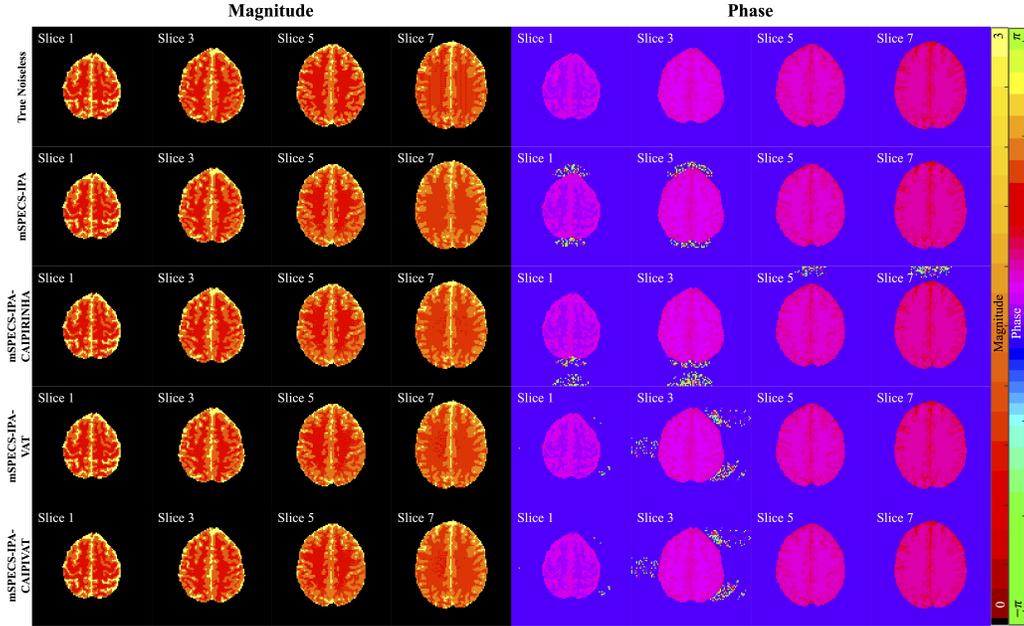
Figure 10: The magnitude and phase of the reconstructed images odd slices from mSPECS-IPA, mSPECS-IPA-CAIPIRINHA, mSPECS-IPA-VAT, and mSPECS-IPA-CAIPIVAT, compared with the magnitude and phase from true noiseless simulated images odd slices with TPA=2.

fMRI time series were applied in the real-world right-handed finger tapping experiment with $R = 2$, and $TPA = 2, 4, 8$. The same net acceleration factors were achieved in the real-world experimental time series. The mSPECS-IPA model, mSPECS-IPA-CAIPIRINHA model, mSPECS-IPA-VAT model and the mSPECS-IPA-CAIPIVAT model were applied to the right-handed finger tapping experiment fMRI time series. The SENSE method was also applied to the calibration fMRI time series, and the reconstructed images were utilized as the reference images. The reconstructed results from the novel image shift SMS technique were compared with the reference images. All simulations and data analyses were implemented in MATLAB (MathWorks, Natick, MA, USA) using MATLAB R2022b. The numerical experiments were performed using built-in MATLAB functions together with standard toolboxes. A fixed random seed was used for the simulation procedures to ensure reproducibility.
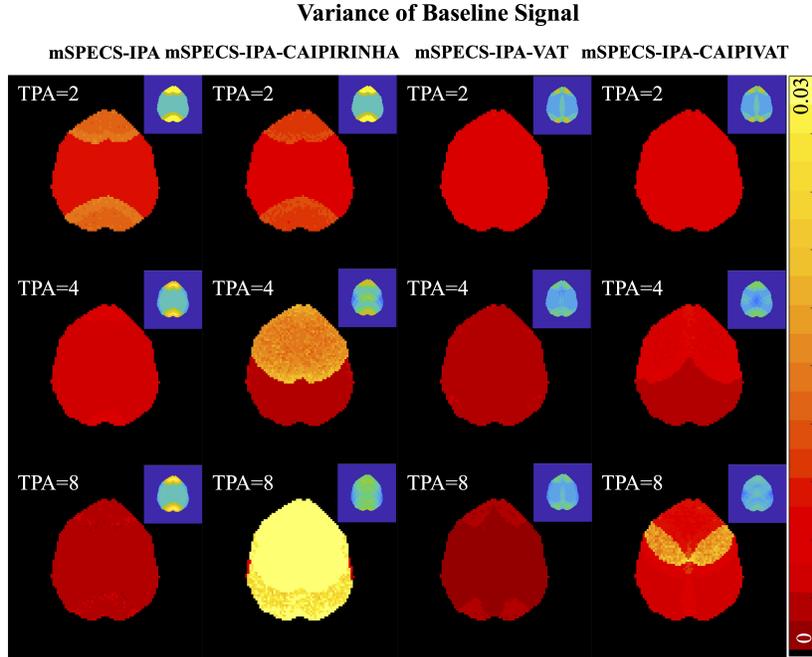
Variance of Baseline Signal

Figure 11: The variance of the baseline regression coefficient of slice 3 from reconstructed images from mSPECS-IPA, mSPECS-IPA-CAIPIRINHA, mSPECS-IPA-VAT, and mSPECS-IPA-CAIPIVAT model with different through-plane acceleration factors. The top-right corner shows the overlapping indicator for each SMS reconstruction model under different TPA factors, illustrating the corresponding slice overlap and voxel aliasing patterns.

4. The Simulation Results

4.1. Non-Task Simulated Reconstruction Results

Based on the methodology of the novel proposed image shift SMS techniques, we conducted the simulated experiment with the same in-plane acceleration factor, $IPA = 2$, and different through-plane acceleration factors with $TPA = 2$, $TPA = 4$, and $TPA = 8$. The reconstructed results were compared between mSPECS-IPA model (without image shift technique), mSPECS-IPA-CAIPIRINHA model (image shift along vertical direction), mSPECS-IPA-VAT model (image shift along horizontal direction), and mSPECS-IPA-CAIPIVAT (image shift along vertical and horizontal direction). The reconstructed results were also compared with the true noiseless simulated images. Fig. 10 shows the mean magnitude and mean phase from
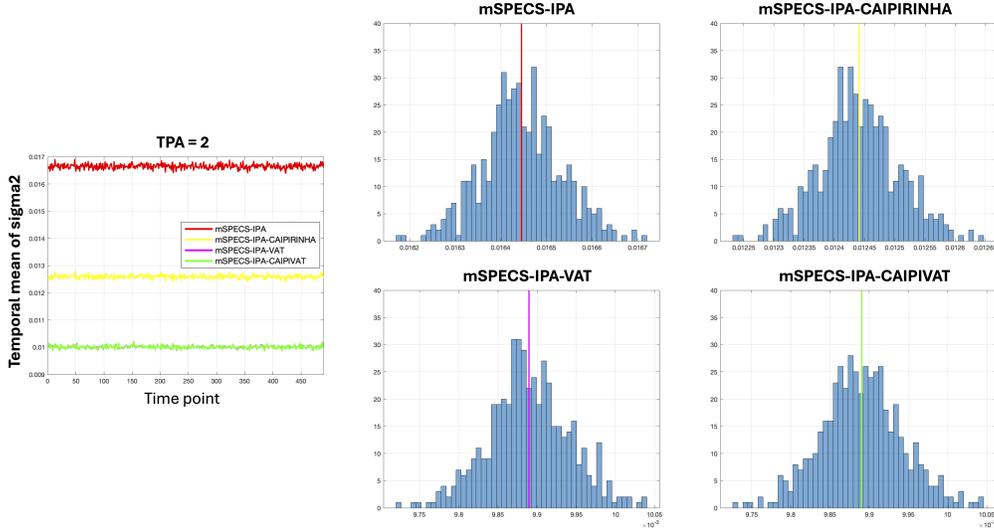
Figure 12: The temporal mean of residual variance of brain images reconstructed from the mSPECS-IPA (red), mSPECS-IPA-CAIPIRINHA (yellow), mSPECS-IPA-VAT (pink), and mSPECS-IPA-CAIPIVAT (green) models with IPA = 2 and TPA = 2. The curve corresponding to the mSPECS-IPA-VAT model (pink) closely overlaps with the curve for the mSPECS-IPA-CAIPIVAT model (green).

odd slices of the reconstructed images from mSPECS-IPA, mSPECS-IPA-CAIPIRINHA, mSPECS-IPA-VAT, and mSPECS-IPA-CAIPIVAT, compared with the magnitude and phase from true noiseless simulated images, and the through-plane acceleration factor is 2. Fig. 10 is generated based on Eq. 21. Compared to the true magnitude, the mean magnitude from these four models is closely aligned with the true value. No inter-slice signal leakage or artifact distortions appear in the mean magnitude images. The mean phase of the reconstructed images from these four models is also consistent with the phase value of the true noiseless simulated image inside the brain. Fig. 11 was generated according to Eq. 22. The top-right corner displays the overlapping indicator for each novel SMS image reconstruction model, incorporating different TPA factors. It represents the slice overlapping and voxel aliasing scenario for each approach and acceleration factor. When the acceleration factor is low, IPA = 2 and TPA = 2, all four models have a low variance at the center of the brain image. As the acceleration factor increases, models that do not incorporat the vertical image shift technique, mSPECS-IPA and mSPECS-IPA-VAT model, show a decrease in task regression coefficient vari-
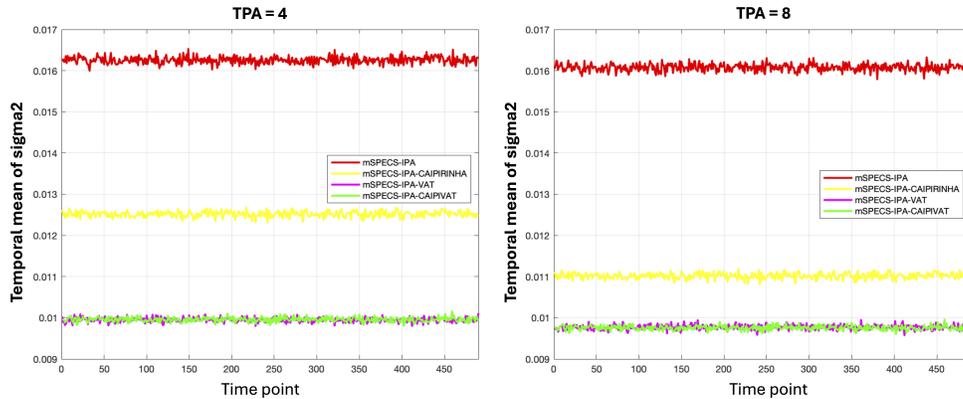
28

Figure 13: The temporal mean of residual variance of brain images reconstructed from mSPECS-IPA, mSPECS-IPA-CAIPIRINHA, mSPECS-IPA-VAT and mSPECS-IPA-CAIPIVAT model with IPA = 2 and TPA = 4 and 8.

ance. On the other hand, models that incorporate with the vertical image shift technique, mSPECS-IPA-CAIPIRINHA and mSPECS-IPA-CAIPIVAT model, exhibit an increase in task regression coefficient variance in the anterior region of the brain image. Among these four models, the mSPECS-IPA-CAIPIRINHA has the highest task regression coefficient variance when IPA = 2 and TPA = 8. The temporal variance of the task signal is shown in the Appendix A Fig. A.21.

Fig. 12 displays temporal mean of residual variance of brain images reconstructed from mSPECS-IPA, mSPECS-IPA-CAIPIRINHA, mSPECS-IPA-VAT and mSPECS-IPA-CAIPIVAT model with IPA = 2 and TPA = 2. Fig. 13 shows temporal mean of residual variance for brain images reconstructed from same models but with acceleration factors IPA = 2 and TPA = 4 and 8. Fig. 12 and Fig. 13 are generated based on Eq. 24. For each acceleration factor, among the four models, mSPECS-IPA has the highest temporal mean of residual variance, whereas the models incorporating the horizontal image shift technique, mSPECS-IPA-VAT and mSPECS-IPA-CAIPIVAT, exhibit the lowest temporal mean of residual variance. As the acceleration factor increases, the temporal mean of residual variance slightly decreases across all four models. We also investigated the temporal variance of the residual variance of brain images reconstructed from mSPECS-IPA, mSPECS-IPA-CAIPIRINHA, mSPECS-IPA-VAT and mSPECS-IPA-CAIPIVAT model with IPA = 2 and TPA = 2, 4, and 8, which is shown in

29

Appendix A Fig. A.22 and Fig. A.23.

We also investigated the signal-to-noise ratio (SNR) and the geometric factor g-factor values across mSPECS-IPA, mSPECS-IPA-CAIPIRINHA, mSPECS-IPA-VAT, and mSPECS-IPA-CAIPIVAT models. The SNR can be calculated as $SNR = \beta_0/\sigma_N$, where β_0 represents the baseline signal for each location of the brain image, and σ_N represents the standard deviation of the noise. According to the g-factor definition(Eq. 1) in Section 2.1.1, the through-plane acceleration factor also needs to be incorporated into it. Thus, the g-factor can be calculated as $g_{accelerate} = \sqrt{N_s} SNR_{full}/SNR_{accelerate}\sqrt{R}$, where $R = 2$ indicating the in-plane acceleration factor. Fig. 14A shows the SNR value of slice 3 for four models with different through-plane acceleration factors. The top right corner is the slice overlapping scenario corresponding to average of the first N_α time point for each model. As the TPA factor increases, the SNR value for the mSPECS-IPA and mSPECS-IPA-VAT models also increases. Moreover, in the mSPECS-IPA-VAT model, both the posterior and anterior regions of the brain exhibit higher SNR values compared to the mSPECS-IPA model. In contrast, for the mSPECS-IPA-CAIPIRINHA and mSPECS-IPA-CAIPIVAT models, the SNR value does not increase evenly across the entire brain image as the TPA factor increases. In the mSPECS-IPA-CAIPIRINHA model, at higher TPA factors, the SNR in the middle brain region is lower than at lower TPA factors. A similar pattern is observed in the left side of the brain image in the mSPECS-IPA-CAIPIVAT model. Fig. 14B shows the g-factor of slice 3 across different models with varying through-plane acceleration factors. As the TPA factor increases, the g-factor in the mSPECS-IPA-CAIPIRINHA and mSPECS-IPA-CAIPIVAT models increases dramatically, whereas in the mSPECS-IPA and mSPECS-IPA-VAT models, it increases only slightly. Comparing the g-factor values between the mSPECS-IPA and mSPECS-IPA-VAT models, the g-factor in the mSPECS-IPA-VAT model is closer to 1 in both the posterior and anterior regions of the brain. These artifacts are expected under aggressive SMS acceleration when using low channel count receiver coils.

4.2. Task Simulated Reconstruction Results

In order to investigate the task activation detection performance of each model, we applied the novel image shift SMS techniques to the simulated right-handed finger tapping experiment with the same in-plane acceleration factor, IPA=2, and different through-plane acceleration factors TPA=2, TPA=4, and TPA=8. For each voxel in the brain image, the signal can be
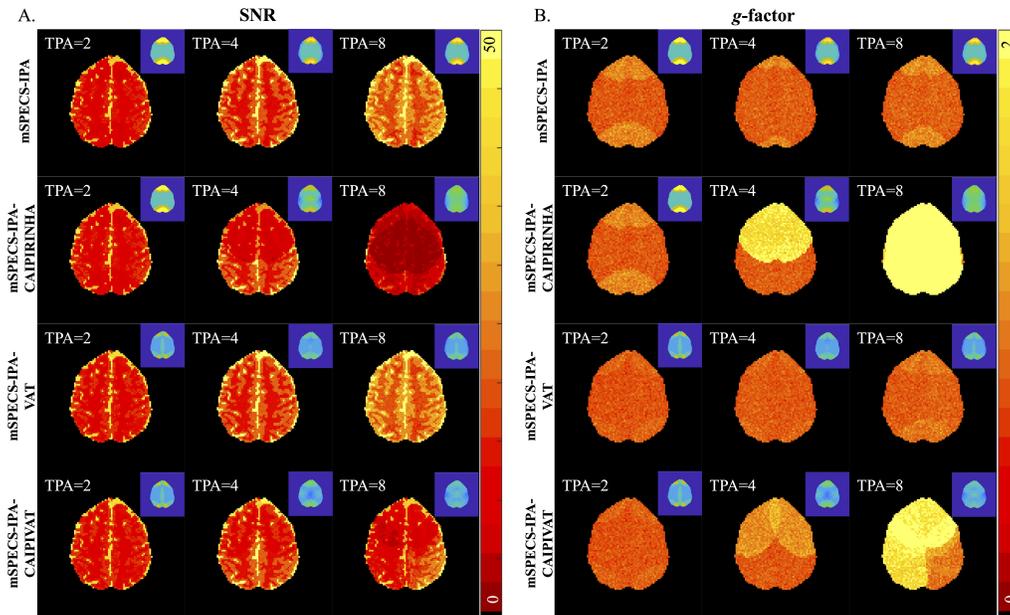
Figure 14: A. The *SNR* value of slice 3 from reconstructed images for mSPECS-IPA, mSPECS-IPA-CAIPIRINHA, mSPECS-IPA-VAT, and mSPECS-IPA-CAIPIVAT model with different TPA factor. B. The *g*-factor value of slice 3 from reconstucted images for mSPECS-IPA, mSPECS-IPA-CAIPIRINHA, mSPECS-IPA-VAT, and mSPECS-IPA-CAIPIVAT model with different TPA factor. The top-right corner shows the overlapping indicator for each SMS reconstruction model under different TPA factors, illustrating the corresponding slice overlap and voxel aliasing patterns.

expressed as $y = \beta_0 + \beta_1 x + \epsilon$, where β_0 is the baseline signal of the voxel, β_1 is the task signal, x is a vector with elements 0 and 1 indicating each time point with or without task activation. Therefore, the contrast-to-noise ratio (*CNR*) can be calculated as $CNR = \beta_1/\sigma_N$, and same as the definition in *SNR*, σ_N stands for the standard deviation of the noise. The activation detection rate for each model was also investigated by applying a complex-valued model to compute fMRI activation (Rowe and Logan [18]). Fig. 15A shows the average and standard deviation of the *CNR* values in the region of interest (ROI) for odd slices from the mSPECS-IPA, mSPECS-IPA-CAIPIRINHA, mSPECS-IPA-VAT, and mSPECS-IPA-CAIPIVAT models with an acceleration factor of TPA = 2. The *CNR* value of the ROI for slice 1 in the mSPECS-IPA-VAT and mSPECS-IPA-CAIPIVAT models is slightly higher than in the mSPECS-IPA and mSPECS-IPA-CAIPIRINHA models. Mean-
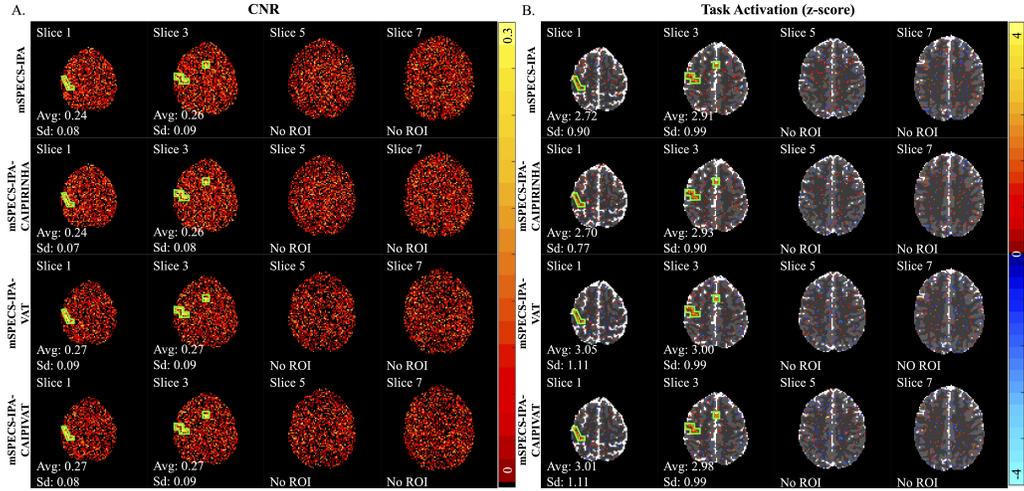
31

Figure 15: A. The average *CNR* value of ROI for odd slices with acceleration factor TPA=2 from mSPECS-IPA, mSPECS-IPA-CAIPIRINHA, mSPECS-IPA-VAT, and mSPECS-IPA-CAIPIVAT model. B. The average task activation rate (z-score) of ROI for odd slices with acceleration factor TPA=2 from mSPECS-IPA, mSPECS-IPA-CAIPIRINHA, mSPECS-IPA-VAT, and mSPECS-IPA-CAIPIVAT model.

while, the *CNR* value of the ROI for slice 3 is similar across all four models. Fig. 15B shows the average task activation detection rate in the ROI for odd slices from the mSPECS-IPA, mSPECS-IPA-CAIPIRINHA, mSPECS-IPA-VAT, and mSPECS-IPA-CAIPIVAT models with TPA = 2. Compared to the models with a horizontal image shift, mSPECS-IPA-VAT and mSPECS-IPA-CAIPIVAT, the models without horizontal image shift, mSPECS-IPA and mSPECS-IPA-CAIPIRINHA, exhibit a lower average z-score in the ROI.

To assess the influence of a high acceleration factor on the task activation detection ability of each model, we compared the *CNR* value and the task activation detection rate of ROI for mSPECS-IPA, mSPECS-IPA-CAIPIRINHA, mSPECS-IPA-VAT, and mSPECS-IPA-CAIPIVAT models under different acceleration factors, TPA = 2, TPA = 4, and TPA = 8. Fig. 16A shows the average *CNR* value in the ROI of slice 3 for the mSPECS-IPA, mSPECS-IPA-CAIPIRINHA, mSPECS-IPA-VAT, and mSPECS-IPA-CAIPIVAT models with different acceleration factors. As the acceleration factor increases, the average *CNR* value decreases across all four models. However, at high acceleration factors, the average *CNR* value in the ROI is higher in the mSPECS-IPA and mSPECS-IPA-VAT models compared to
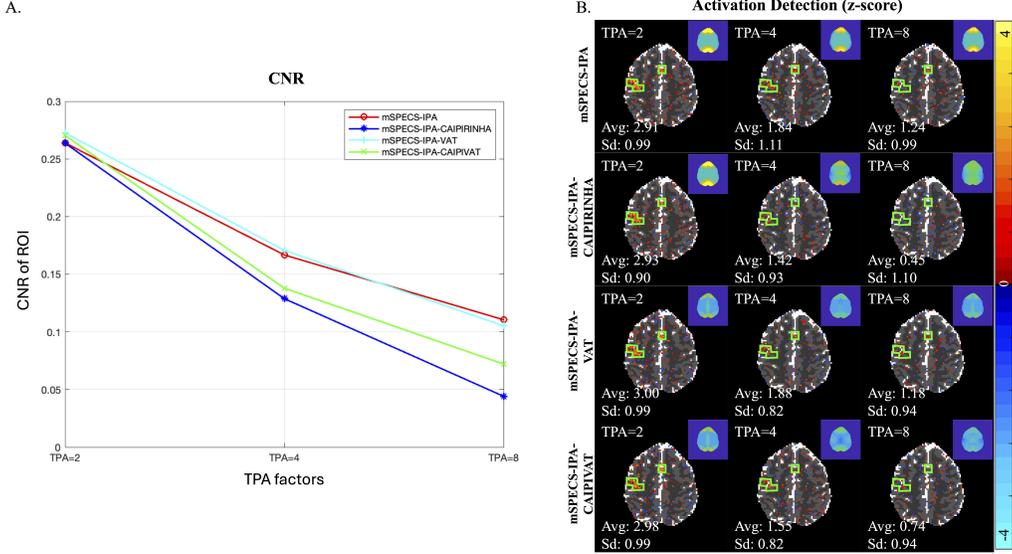
Figure 16: A. The average *CNR* value of ROI for slice 3 from mSPECS-IPA, mSPECS-IPA-CAIPIRINHA, mSPECS-IPA-VAT, and mSPECS-IPA-CAIPIVAT model with acceleration factor TPA=2, TPA=4, and TPA=8. B. The average activation detection rate (z-score) of ROI for slice 3 from mSPECS-IPA, mSPECS-IPA-CAIPIRINHA, mSPECS-IPA-VAT, and mSPECS-IPA-CAIPIVAT model with acceleration factor TPA=2, TPA=4, and TPA=8. The top-right corner shows the overlapping indicator for each SMS reconstruction model under different TPA factors, illustrating the corresponding slice overlap and voxel aliasing patterns.

the models incorporating vertical image shift, mSPECS-IPA-CAIPIRINHA and mSPECS-IPA-CAIPIVAT. Among these models, the model applies image shift only along the vertical direction, mSPECS-IPA-CAIPIRINHA exhibits the lowest average *CNR* value in the ROI. Fig. 16B shows the activation detection rate (z-score) in the ROI of slice 3 for the mSPECS-IPA, mSPECS-IPA-CAIPIRINHA, mSPECS-IPA-VAT, and mSPECS-IPA-CAIPIVAT models with different acceleration factors. However, at TPA = 8, the models without vertical image shift, mSPECS-IPA and mSPECS-IPA-VAT, exhibit higher average z-scores in the ROI compared to the models with vertical image shift, mSPECS-IPA-CAIPIRINHA and mSPECS-IPA-CAIPIVAT. Although the models incorporating vertical image shift exhibit lower average z-scores in the ROI, the mSPECS-IPA-CAIPIVAT model achieves a higher average z-score compared to the mSPECS-IPA-CAIPIRINHA model. Among all models, mSPECS-IPA-CAIPIRINHA provides the lowest
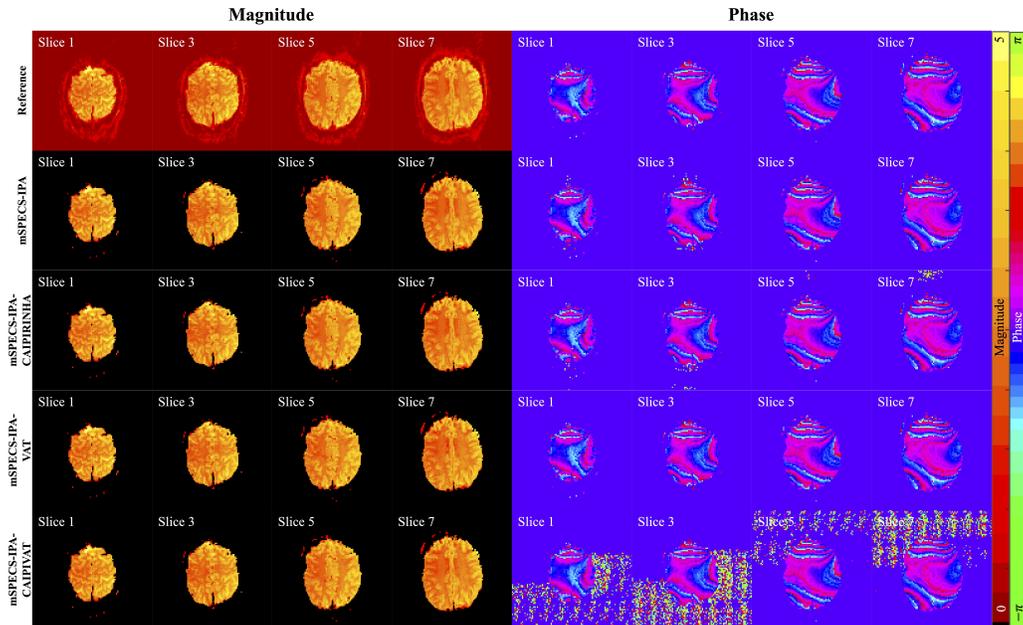
Figure 17: The mean magnitude and mean phase of the odd slices from reconstructed image with through-plane acceleration factor TPA=2 corresponding to mSPECS-IPA, mSPECS-IPA-CAIPIRINHA, mSPECS-IPA-VAT and mSPECS-IPA-CAIPIVAT model.

activation detection rate, indicating that it has the least ability to capture the simulated task activation blocks. Although the proposed method exhibits higher mean *CNR* and activation detection rates across several configurations, the associated variability indicates that these improvements are not uniformly statistically significant. The detailed quantitative values of the activation detection (z-score) and *CNR* for the simulation and experimental analyses are summarized in Tables A.1 in the Supplementary Materials.

5. The Experimental Results

5.1. Non-Task Experimental Reconstruction Results

To investigate the performance of the proposed novel image-shifted SMS techniques in a real-world fMRI experiment, we applied four models to an in vivo right-handed finger-tapping fMRI time series. The reconstruction results from these models were compared with reference axial brain images, reconstructed using the SENSE technique from the calibration axial brain image time series. Additionally, we applied the novel image-shifted SMS

34

techniques with the same in-plane acceleration factor, IPA = 2, and varying through-plane acceleration factors, TPA = 2, TPA = 4, and TPA = 8, to examine the impact of acceleration on each model. Fig. 17 shows the mean magnitude and mean phase of the odd slices reconstructed with TPA = 2 from the mSPECS-IPA, mSPECS-IPA-CAIPIRINHA, mSPECS-IPA-VAT, and mSPECS-IPA-CAIPIVAT models, compared to the mean magnitude and mean phase of the reference image from the calibration images. Compared to the mean magnitude of the reference image, the mean magnitude from the four image-shifted SMS models is closely aligned with the reference image. No inter-slice signal leakage or artifactual brain distortions from other slices were observed in the reconstructed images. Compared to the mean phase of the reference image, the mean phase of the reconstructed images from the mSPECS-IPA, mSPECS-IPA-CAIPIRINHA, mSPECS-IPA-VAT, and mSPECS-IPA-CAIPIVAT models exhibits a highly similar pattern inside the brain. However, residual artifacts (which could be measured) appear outside the brain, particularly in the mSPECS-IPA-CAIPIRINHA and mSPECS-IPA-CAIPIVAT models, which can be attributed to voxel aliasing, slice overlapping, and image shift techniques applied in different models. The temporal variance of the task signal is shown in Appendix B Fig. A.24.

Similar to the simulation-based reconstructed axial brain image analysis, we also investigate the signal-to-noise ratio (SNR) and the geometric factor (g-factor) in the reconstructed brain images from the mSPECS-IPA, mSPECS-IPA-CAIPIRINHA, mSPECS-IPA-VAT, and mSPECS-IPA-CAIPIVAT models under different acceleration factors. The SNR value and the g-factor are calculated as described in Section 4.1. Fig. 18A shows the average SNR value for slice 3 in the mSPECS-IPA, mSPECS-IPA-CAIPIRINHA, mSPECS-IPA-VAT, and mSPECS-IPA-CAIPIVAT models with acceleration factors TPA = 2, TPA = 4, and TPA = 8. As the acceleration factor increases, the average SNR in the mSPECS-IPA and mSPECS-IPA-VAT models also increases. The mSPECS-IPA-VAT model exhibits a higher average SNR at the edges of the brain image compared to the mSPECS-IPA model. Conversely, in the models incorporating vertical image shift (mSPECS-IPA-CAIPIRINHA and mSPECS-IPA-CAIPIVAT), the average SNR initially increases as the acceleration factor increases from TPA = 2 to TPA = 4 but decreases at TPA = 8. Comparing the average SNR of the reconstructed axial brain images across the four models, the mSPECS-IPA-VAT model provides the highest SNR value. Fig. 18B shows the g-factor of the reconstructed image of slice 3 for the mSPECS-IPA, mSPECS-IPA-CAIPIRINHA,
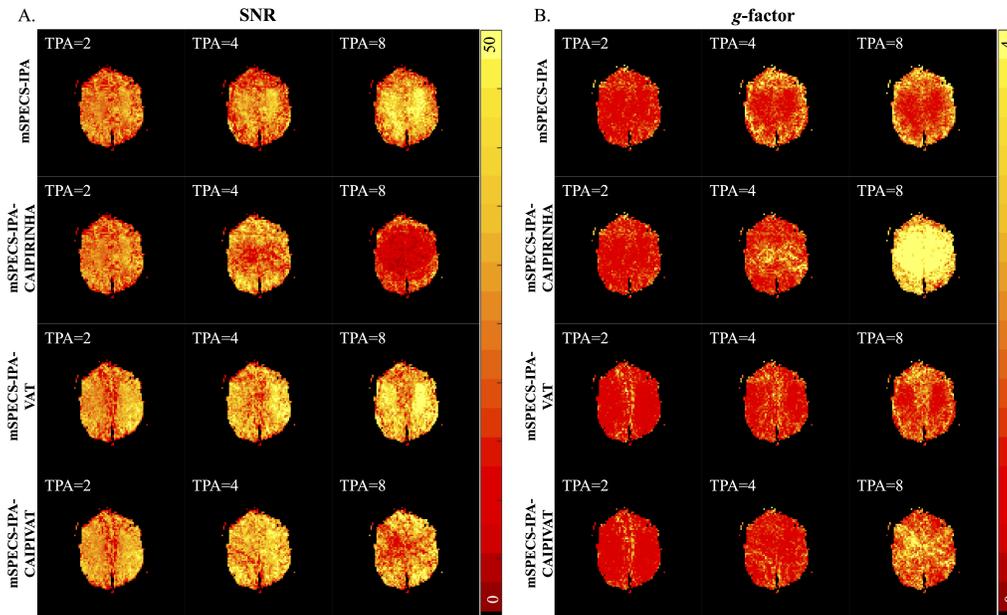
Figure 18: A. The *SNR* value of reconstructed brain images slice 3 from mSPECS-IPA, mSPECS-IPA-CAIPIRINHA, mSPECS-IPA-VAT and mSPECS-IPA-CAIPIVAT model with different acceleration factors. B. The *g*-factor value of reconstructed brain images slice 3 from mSPECS-IPA, mSPECS-IPA-CAIPIRINHA, mSPECS-IPA-VAT and mSPECS-IPA-CAIPIVAT model with different acceleration factors.

mSPECS-IPA-VAT, and mSPECS-IPA-CAIPIVAT models under different acceleration factors. Although the *g*-factor increases across all four models as the acceleration factor increases, the mSPECS-IPA-VAT model exhibits the lowest *g*-factor compared to the other three models. In contrast, the mSPECS-IPA-CAIPIRINHA model has the highest *g*-factor among the four models at TPA = 8.

5.2. Task Experimental Reconstruction Results

To analyze the activation detection ability of the proposed image-shifted SMS technique in a real-world right-handed finger-tapping fMRI experiment, we also investigate the contrast-to-noise ratio (*CNR*) and the activation detection rate (z-score) of ROI of the reconstructed axial brain images from the mSPECS-IPA, mSPECS-IPA-CAIPIRINHA, mSPECS-IPA-VAT, and mSPECS-IPA-CAIPIVAT models under different acceleration factors. Since a right-handed finger-tapping fMRI experiment was conducted, the
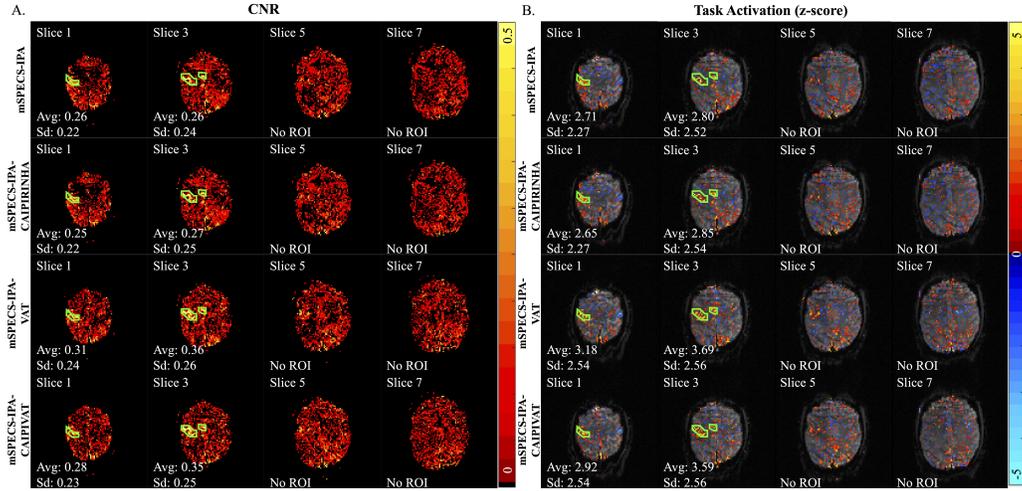
Figure 19: A. The average *CNR* value of ROI for odd slices of reconstructed images from mSPECS-IPA, mSPECS-IPA-CAIPIRINHA, mSPECS-IPA-VAT and mSPECS-IPA-CAIPIVAT model with TPA=2. B. The task activation detection (z-score) map of ROI for odd slices of reconstructed images from mSPECS-IPA, mSPECS-IPA-CAIPIRINHA, mSPECS-IPA-VAT and mSPECS-IPA-CAIPIVAT model with TPA=2.

task activation area was expected to be in the left motor cortex of the brain. Fig. 19A shows the average *CNR* value in the ROI for odd slices of the reconstructed images from the mSPECS-IPA, mSPECS-IPA-CAIPIRINHA, mSPECS-IPA-VAT, and mSPECS-IPA-CAIPIVAT models with an acceleration factor of TPA = 2. Compared to models without horizontal image shift, mSPECS-IPA and mSPECS-IPA-CAIPIRINHA, models incorporating horizontal image shift, mSPECS-IPA-VAT and mSPECS-IPA-CAIPIVAT, exhibit a higher average *CNR* value in the ROI, with mSPECS-IPA-VAT achieving the highest *CNR* value among the four models. Fig. 19B shows the task activation detection rate for odd slices of the reconstructed images from the mSPECS-IPA, mSPECS-IPA-CAIPIRINHA, mSPECS-IPA-VAT, and mSPECS-IPA-CAIPIVAT models with TPA = 2. Similar to the conclusion drawn from the average *CNR* in the ROI, the mSPECS-IPA-VAT and mSPECS-IPA-CAIPIVAT models exhibit a higher average z-score in the ROI of the left motor cortex compared to the mSPECS-IPA and mSPECS-IPA-CAIPIRINHA models. Among these four models, the mSPECS-IPA-VAT model provides the best activation detection map at TPA = 2.

The average *CNR* value in the ROI and the task activation detection

37

rate were also analyzed for the mSPECS-IPA, mSPECS-IPA-CAIPIRINHA, mSPECS-IPA-VAT, and mSPECS-IPA-CAIPIVAT models under different acceleration factors. Fig. 20A shows the average CNR value in the ROI of slice 3 for the four models, compared at different acceleration factors, TPA = 2, TPA = 4, and TPA = 8. As the acceleration factor increases, the average CNR decreases significantly across all four models. However, among them, the mSPECS-IPA-VAT model provides the highest average CNR in the ROI, while the mSPECS-IPA-CAIPIRINHA model exhibits the lowest average CNR. Moreover, models incorporating horizontal image shift exhibit a higher average CNR in the ROI compared to models without horizontal image shift. Fig. 20B shows the average task activation detection map for the ROI of slice 3 across the four models with different acceleration factors. As the acceleration factor increases, the average z-score in the ROI decreases significantly for each model. Among these four models, the mSPECS-IPA-VAT model provides the highest average z-score in the ROI, while the mSPECS-IPA-CAIPIRINHA model exhibits the lowest. Additionally, models incorporating vertical image shift exhibit a lower average z-score compared to models without vertical image shift. A detailed quantitative values of the activation detection (z-score) and CNR for the simulation and experimental analyses are summarized in Tables B.2 in the Supplementary Materials.

6. Discussion

The primary objective of this study was to evaluate the proposed complex-valued Bayesian reconstruction framework under different acceleration and image-shift conditions, rather than merely to compare image-shift strategies. The simulation and experimental results together show that reconstruction performance depends strongly on both acceleration factor and image-shift direction, particularly when activation detection is used as the performance criterion.

With increasing through-plane acceleration, the reconstructed images generally exhibited a trade-off between acquisition efficiency and activation sensitivity. Although SNR increased in some models, particularly mSPECS-IPA and mSPECS-IPA-VAT, both CNR and activation-related z-scores decreased as the acceleration factor increased. This pattern indicates that higher acceleration does not necessarily improve the practical detectability of task-related signals, even when image reconstruction remains visually acceptable. Among the four models considered in this study, mSPECS-IPA-VAT showed
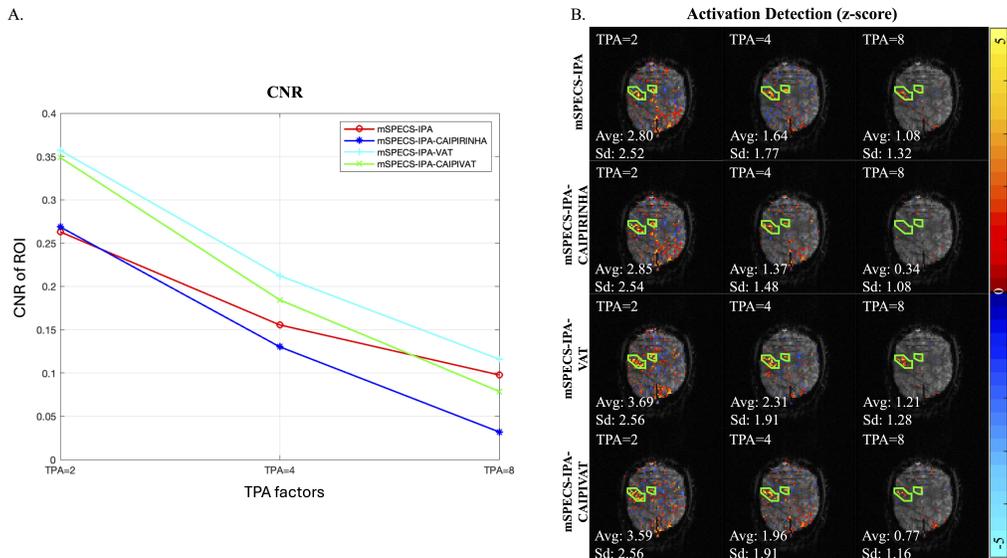
38

Figure 20: A. The average *CNR* value of ROI for slice 3 from mSPECS-IPA, mSPECS-IPA-CAIPIRINHA, mSPECS-IPA-VAT, and mSPECS-IPA-CAIPIVAT model with acceleration factor TPA=2, TPA=4, and TPA=8. B. The average activation detection rate (z-score) of ROI for slice 3 from mSPECS-IPA, mSPECS-IPA-CAIPIRINHA, mSPECS-IPA-VAT, and mSPECS-IPA-CAIPIVAT model with acceleration factor TPA=2, TPA=4, and TPA=8.

the most stable performance across acceleration settings, maintaining comparatively higher *CNR* and z-scores under both simulated and experimental conditions. Previous studies suggest that an optimal multiband factor for resting-state fMRI is MB = 4 (Risk et al. [16]). From a practical perspective, the results suggest that moderate acceleration factors, such as IPA = 2 combined with TPA = 2, provide a more favorable balance between scan efficiency and activation detection performance, which is consistent with the conclusions of previous studies. Image-shift direction also had a substantial effect on reconstruction quality. Models incorporating vertical image shift, namely mSPECS-IPA-CAIPIRINHA and mSPECS-IPA-CAIPIVAT, generally showed poorer performance than models without vertical shift, especially at high acceleration factors. One possible explanation is that vertical image shift occurs in the same direction as the in-plane acceleration, leading to more complex slice overlap and voxel aliasing patterns. As the complexity of slice overlap increases, the separation of aliased slices becomes more difficult, resulting in a less favorable conditioning of the reconstruction problem. In

contrast, the horizontal shift used in mSPECS-IPA-VAT produced lower g-factor penalties and more favorable activation-related measures. These findings suggest that, within the present framework, image shift should preferably be applied in a direction different from the in-plane acceleration direction.

The Bayesian reconstruction framework provides voxel-wise posterior mean estimates together with associated uncertainty measures, allowing variability in the reconstructed signal to be quantified. The incorporation of calibration-derived prior information also introduces structured regularization that stabilizes the reconstruction under accelerated acquisitions. The advantages of this framework are most apparent under moderate acceleration settings and appropriate encoding strategies. In particular, improved activation detection was observed when IPA = 2 and TPA = 2, especially when horizontal image shift (VAT) was applied, where higher CNR and z-scores were obtained. At very high acceleration factors (e.g., TPA = 8), however, increased voxel aliasing and g-factor penalties reduce these benefits.

The proposed Bayesian framework should also be interpreted in relation to established SMS reconstruction methods such as Slice-GRAPPA, Split-Slice-GRAPPA, and MB-SENSE. Unlike these approaches, which produce deterministic voxel estimates, the present method provides posterior mean estimates together with voxel-wise posterior variance, enabling explicit uncertainty quantification. The Bayesian formulation also incorporates prior information from calibration images that introduces structured regularization and can stabilize reconstruction under accelerated acquisitions. The present study does not include a direct benchmark comparison with these techniques. Such comparisons are not entirely straightforward because conventional SMS reconstruction methods are typically designed for standard multiband acquisitions with fixed slice aliasing patterns separated using coil sensitivity information and calibration kernels. In contrast, the proposed framework incorporates additional encoding diversity through image-shift strategies combined with a 2D Hadamard phase-encoding scheme across multiple excitations. This design introduces structured variations in slice overlap and voxel aliasing patterns that are explicitly modeled in the Bayesian reconstruction framework but are not directly represented in conventional Slice-GRAPPA, Split-Slice-GRAPPA, or MB-SENSE formulations. A systematic benchmark under acquisition settings designed to support both the proposed framework and conventional SMS reconstruction pipelines will therefore be investigated in future work using true multiband acquisitions and higher channel-count receiver arrays.

Several limitations of the proposed approach should be acknowledged. First, the 2D Hadamard encoding strategy requires multiple excitations to complete a full encoding cycle, which reduces the effective temporal sampling rate relative to conventional single-shot SMS acquisitions. Consequently, the framework is more naturally suited to block-design paradigms or moderate-TR studies than to high temporal resolution fMRI. Second, the current model assumes spatially independent Gaussian noise, whereas real EPI data may exhibit spatial and temporal correlations arising from physiological fluctuations and scanner drift. This independence assumption simplifies the reconstruction model but does not fully capture the noise structure present in practical fMRI acquisitions. Future extensions of the framework could incorporate more realistic noise models, such as spatial covariance structures or additional components representing physiological noise, to better characterize noise propagation in accelerated imaging. Third, the experimental study used an 8-channel receiver coil, which limits coil sensitivity diversity and is expected to reduce reconstruction stability under aggressive acceleration.

In summary, the present results suggest that the proposed Bayesian reconstruction framework provides a probabilistic approach for 2D-accelerated SMS fMRI that may offer advantages under certain acquisition settings, particularly with moderate acceleration and appropriate image-shift strategies. Among the configurations considered, horizontal image shift produced more stable reconstruction performance than vertical image shift within the current encoding design. The mSPECS-IPA-CAIPIVAT framework showed potential improvements in activation detection under these conditions, although the magnitude of the improvements was modest and depended on the acceleration and encoding configuration. The Bayesian formulation also provides voxel-wise uncertainty estimates and prior-based regularization derived from calibration data, which may help stabilize reconstruction in accelerated imaging. Consequently, the proposed approach should be interpreted as a complementary reconstruction framework that may offer benefits in specific scenarios rather than a universal replacement for existing SMS reconstruction methods. Future work will include higher channel-count receiver arrays, as well as extensions of the Bayesian model to incorporate more realistic spatial-temporal noise structures.
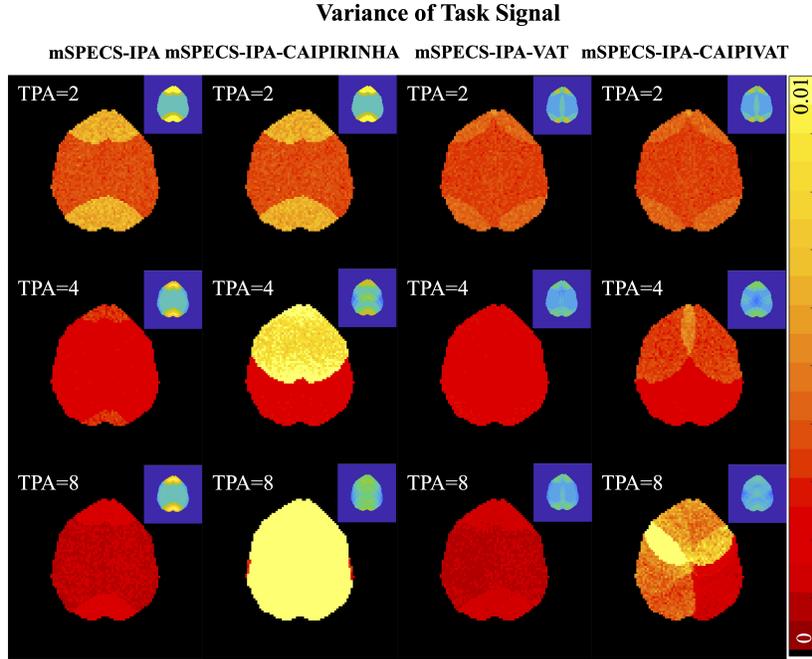
Variance of Task Signal

Figure A.21: The task regression coefficient variance of slices 3 from reconstructed images from mSPECS-IPA, mSPECS-IPA-CAIPIRINHA, mSPECS-IPA-VAT, and mSPECS-IPA-CAIPIVAT model with different through-plane acceleration factors. The top-right corner shows the overlapping indicator for each SMS reconstruction model under different TPA factors, illustrating the corresponding slice overlap and voxel aliasing patterns.

7. Acknowledgment

Appendix A. Supplemental Simulation Results

In the main text, we displays the temporal variance of the baseline signal of slice 3 from reconstructed images corresponding to four SMS models: mSPECS-IPA, mSPECS-IPA-CAIPIRINHA, mSPECS-IPA-VAT, and mSPECS-IPA-CAIPIVAT model with different through-plane acceleration factors. Fig. A.21 shows the temporal variance of task coefficient of slice 3
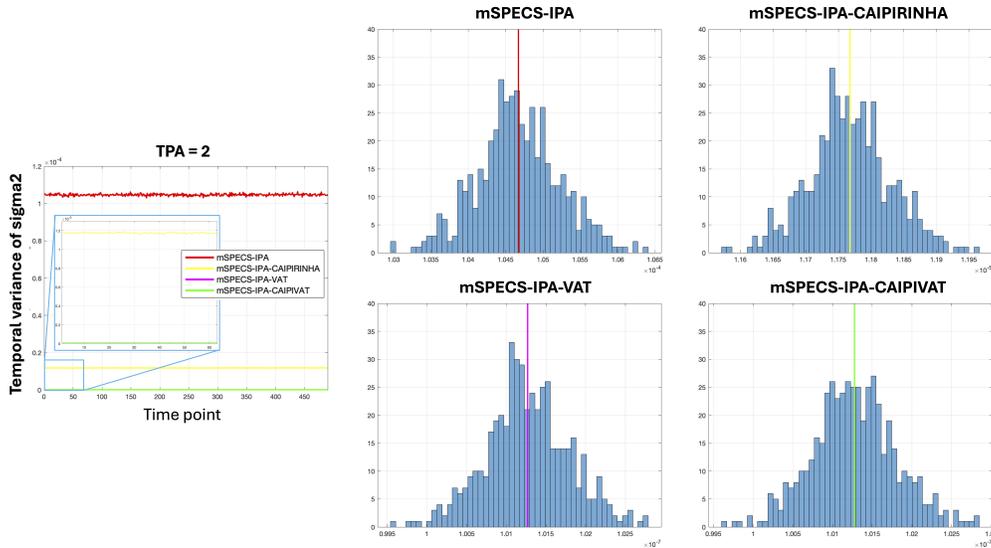
Figure A.22: The variance of the baseline regression coefficient of slice 3 from reconstructed images using the mSPECS-IPA (red), mSPECS-IPA-CAIPIRINHA (yellow), mSPECS-IPA-VAT (pink), and mSPECS-IPA-CAIPIVAT (green) models with IPA=2 and TPA=2. The curve corresponding to the mSPECS-IPA-VAT model (pink) closely overlaps with the curve for the mSPECS-IPA-CAIPIVAT model (green).

from the reconstructed images corresponding to the mSPECS-IPA, mSPECS-IPA-CAIPIRINHA, mSPECS-IPA-VAT, and mSPECS-IPA-CAIPIVAT with different through-plane acceleration factors. The top right corner is the slice overlapping scenario corresponding to the average of first N_α time point for each model, indicating the voxel aliasing complexity for each method. For TPA = 2 and IPA = 2, the voxel aliasing and slice overlapping conditions are identical for the mSPECS-IPA and mSPECS-IPA-CAIPIRINHA models, as well as for the mSPECS-IPA-VAT and mSPECS-IPA-CAIPIVAT models. Consequently, the temporal variance of the reconstructed images from mSPECS-IPA is similar to that of mSPECS-IPA-CAIPIRINHA, while mSPECS-IPA-VAT exhibits similar behavior to mSPECS-IPA-CAIPIVAT. Comparing temporal variance across different models, mSPECS-IPA and mSPECS-IPA-CAIPIRINHA yield higher variance values than mSPECS-IPA-VAT and mSPECS-IPA-CAIPIVAT, particularly in the posterior-to-anterior regions of the brain. When the through-plane acceleration factor increases to 4 and 8, mSPECS-IPA-CAIPIRINHA exhibits the highest tem-

poral variance among the four models. Although the temporal variance in the posterior region is lower for mSPECS-IPA-CAIPIVAT compared to mSPECS-IPA-CAIPIRINHA, high temporal variance values are observed in the anterior region of the brain in the mSPECS-IPA-CAIPIVAT model. The mSPECS-IPA and mSPECS-IPA-VAT demonstrate better temporal variance performance compared to models incorporating vertical shifts. Among the four models, mSPECS-IPA-VAT provides the best temporal variance performance at high acceleration factors.

Fig. A.22 shows the temporal variance of the residual variance for brain images reconstructed from four SMS models: mSPECS-IPA, mSPECS-IPA-CAIPIRINHA, mSPECS-IPA-VAT and mSPECS-IPA-CAIPIVAT model with IPA = 2 and TPA = 2. Fig. A.23 shows the temporal variance of the residual variance for brain images reconstructed from the same model but with acceleration factor IPA = 2 and TPA = 4 and 8. Fig. A.22 and Fig. A.23 are generated from Eq. 25. For each acceleration factor, the mSPECS-IPA model has the highest temporal variance of residual variance, while the mSPECS-IPA-VAT and mSPECS-IPA-CAIPIVAT models have the lowest, with values approaching zero. Moreover, as the acceleration factor increases, the temporal variance of residual variance decreases for all four models.
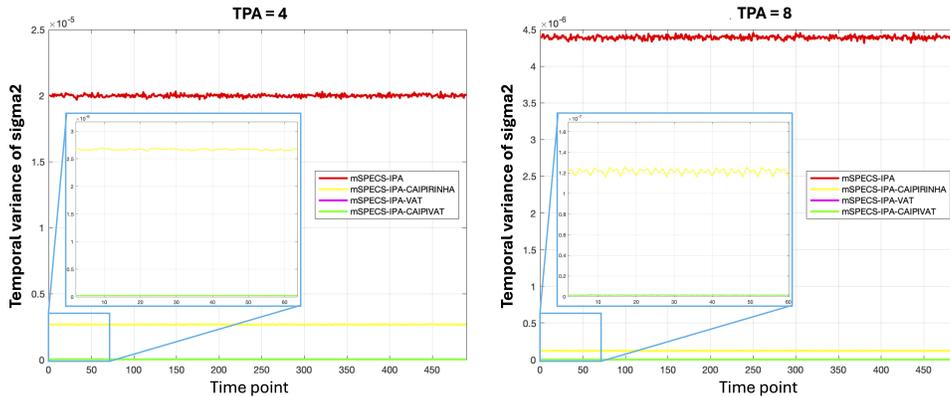

Figure A.23: Variance of the baseline regression coefficient of slice 3 from reconstructed images using the mSPECS-IPA (red), mSPECS-IPA-CAIPIRINHA (yellow), mSPECS-IPA-VAT (pink), and mSPECS-IPA-CAIPIVAT (green) models with IPA=2, TPA=4 and TPA=8. The curve corresponding to the mSPECS-IPA-VAT model (pink) closely overlaps with the curve for the mSPECS-IPA-CAIPIVAT model (green).

Variance of Task Signal

mSPECS-IPA mSPECS-IPA-CAIPIRINHA   mSPECS-IPA-VAT   mSPECS-IPA-CAIPIVAT
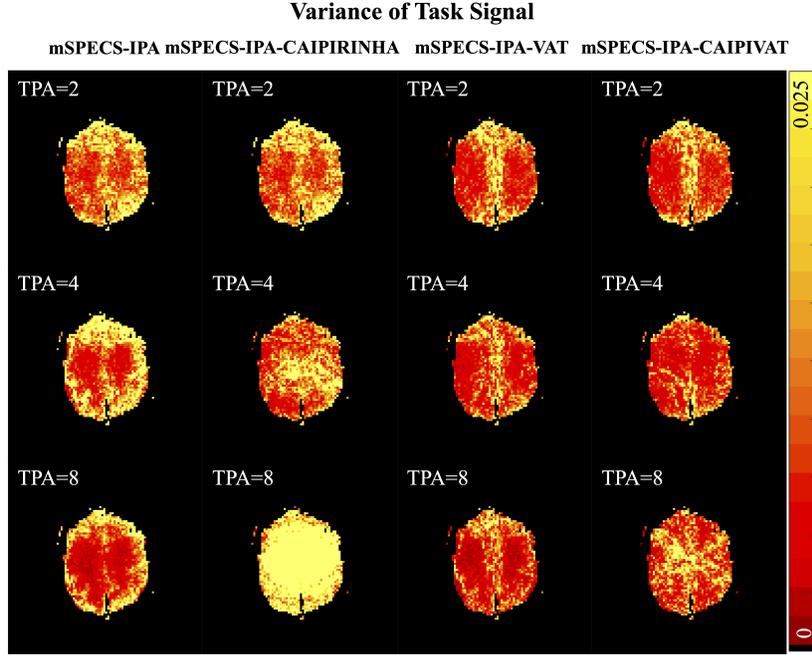
Figure A.24: The temporal variance of reconstructed image for slice 3 from mSPECS-IPA, mSPECS-IPA-CAIPIRINHA, mSPECS-IPA-VAT and mSPECS-IPA-CAIPIVAT model with different acceleration factor TPA=2, TPA=4, and TPA=8.

Table A.1: Activation detection (z-score) and *CNR* for different reconstruction methods under varying through-plane acceleration factors for simulation results.

	Activation Detection (z-score)		
Method	TPA = 2	TPA = 4	TPA = 8
mSPECS-IPA	2.91	1.84	1.24
mSPECS-IPA-CAIPIRINHA	2.93	1.42	0.45
mSPECS-IPA-VAT	3.00	1.88	1.18
mSPECS-IPA-CAIPIVAT	2.98	1.55	0.74
	CNR		
Method	TPA = 2	TPA = 4	TPA = 8
mSPECS-IPA	0.26	0.17	0.11
mSPECS-IPA-CAIPIRINHA	0.26	0.13	0.04
mSPECS-IPA-VAT	0.27	0.17	0.10
mSPECS-IPA-CAIPIVAT	0.27	0.13	0.07

Table B.2: Activation detection (z-score) and *CNR* for different reconstruction methods under varying through-plane acceleration factors for experimental results.

Method	Activation Detection (z-score)		
	TPA = 2	TPA = 4	TPA = 8
mSPECS-IPA	2.80	1.64	1.08
mSPECS-IPA-CAIPIRINHA	2.85	1.37	0.34
mSPECS-IPA-VAT	3.69	2.31	1.21
mSPECS-IPA-CAIPIVAT	3.59	1.96	0.77
Method	*CNR*		
	TPA = 2	TPA = 4	TPA = 8
mSPECS-IPA	0.26	0.16	0.11
mSPECS-IPA-CAIPIRINHA	0.26	0.12	0.04
mSPECS-IPA-VAT	0.27	0.17	0.11
mSPECS-IPA-CAIPIVAT	0.27	0.14	0.07

Appendix B. Supplemental Experimental Results

Fig. A.24 shows the temporal variance of the reconstructed image of slice 3 for each model under different acceleration factors. As the acceleration factor increases, the temporal variance increases significantly in the mSPECS-IPA-CAIPIRINHA model. The temporal variance in the mSPECS-IPA-CAIPIVAT model also increases, particularly in the central region of the brain, as the acceleration factor increases. However, in the two models without vertical image shift techniques, mSPECS-IPA and mSPECS-IPA-VAT, the temporal variance decreases. Moreover, in a comparison between these two models, the mSPECS-IPA-VAT model exhibits lower temporal variance in the left and right motor cortex regions of the brain as the acceleration factor increases.

References

[1] Barth, M., Breuer, F., Koopmans, P. J., Norris, D. G., and Poser, B. A. *Simultaneous multislice (SMS) imaging techniques.* Magn Reson Med. 75(1):63–81. https://doi.org/10.1002/mrm.25897.

[2] Breuer, F. A., Blaimer, M., Heidemann, R. M., Mueller, M. F., Griswold, M. A., and Jakob, P. M. *Controlled aliasing in parallel imaging results in*

higher acceleration (CAIPIRINHA) for multi-slice imaging. Magn Reson Med. 53(3):684–91. https://doi.org/10.1002/mrm.20401.

[3] Cho, Z. H., Kim, D. J., and Kim, Y. K. *Total inhomogeneity correction including chemical shifts and susceptibility by view angle tilting.* Medical physics. 15(1), 7-11. https://doi.org/10.1118/1.596162.

[4] Cauley, S. F., Polimeni, J. R., Bhat, H., Wald, L. L., and Setsompop, K. *Interslice leakage artifact reduction technique for simultaneous multislice acquisitions*, Magn Reson Med, 72(1), 93-102. https://doi.org/10.1002/mrm.24898

[5] Fletcher, D. W., Haselgrove, J. C., and Bolinger, L. *High-resolution imaging using Hadamard encoding.* Magnetic Resonance Imaging. 17(10), 1457-1468. https://doi.org/10.1016/S0730-725X(99)00098-3.

[6] Griswold, M. A., Jamob, P. M., Heidemann, R. M., Nikkka, M., Jellus, V., Wang, J., Kiefer, B., and Haase, A. *Generalized autocalibrating partially parallel acquisition (GRAPPA).* Magn Reson Med. 47:1202–1210. https://doi.org/10.1002/mrm.10171.

[7] Hyde, J. S., Jesmanowicz, A., Froncisz, W., Kneeland, J. B., Grist, T. M., and Campagna, N. F. *Parallel image acquisition from noninteracting local coils.* Journal of Magnetic Resonance. 70(3), 512-517. https://doi.org/10.1016/0022-2364(86)90146-0.

[8] Jungmann, P. M., Ganter, C., Schaeffeler, C. J., Bauer, J. S., Baum, T., Meier, R., Nittka, M., Pohlig, F., Rechl, H., von Eisenhart-Rothe, R., Rummeny, E. J., and Woertler, K. *View-Angle Tilting and Slice-Encoding Metal Artifact Correction for Artifact Reduction in MRI: Experimental Sequence Optimization for Orthopaedic Tumor Endoprostheses and Clinical Application.* PLoS One. 10(4):e0124922. https://doi.org/10.1371/journal.pone.0124922.

[9] Kociuba, M. C. *A Fourier description of covariance, and separation of simultaneously encoded slices with in-plane acceleration in fMRI.* Ph.D. Dissertation. Marquette University, Milwaukee, Wisconsin, USA. https://api.semanticscholar.org/CorpusID:114186307.

[10] Kim, M-O, Hong, T., and Kim, D-H. *Multislice CAIPIRINHA Using View Angle Tilting Technique (CAIPIVAT).* Tomography. 43-48. https://doi.org/10.18383/j.tom.2016.00109.

[11] Kim, M-O, Zho, S-Y, and Kim, D-H. *3D imaging using magnetic resonanace tomosynthesis (MRT) technique.* Med. Phys. 39(8): 4733-4741. https://doi.org/10.1118/1.4737111.

[12] Lin, F. H., Kwong, K. K., Belliveau, J. W., and Wald, L. L. *Parallel imaging reconstruction using automatic regularization.* Magnetic Resonance in Medicine. 51(3), 559-567. https://doi.org/10.1002/mrm.10718.

[13] Mansfield, P. *Multi-planar image formation using NMR spin echoes.* Journal of Physics C: Solid State Physics. 10(3): L55. https://dx.doi.org/10.1088/0022-3719/10/3/004.

[14] Ogawa, S., Lee, T. M., Kay, A. R., and Tank, D. W. *Brain magnetic resonance imaging with contrast dependent on blood oxygenation.* Proc Natl Acad Sci USA. 87(24):9868-721. https://doi.org/10.1073/pnas.87.24.9868.

[15] Pruessmann, K. P., Weiger, M., Scheidegger, M. B., and Boesiger, P. *SENSE: Sensitivity Encoding for Fast MRI.* Magn Reson Med. 42:952–962. https://doi.org/10.1002/(SICI)1522-2594(199911)42:5<952::AID-MRM16>3.0.CO;2-S

[16] Risk, B. B., Murden, R. J., Wu, J., Nebel, M. B., Venkataraman, A., Zhang, Z., and Qiu, D. *Which multiband factor should you choose for your resting-state fMRI study?* Neuroimage. 234:117965. https://doi.org/10.1016/j.neuroimage.2021.117965

[17] Rowe, D. B., Bruce, I. P., Nencka, A. S., Hyde, J. S., and Kociuba, M. C. *Separation of parallel encoded complex-valued slices (SPECS) from a signal complex-valued aliased coil image.* Magn Reson Imaging. 34(3):359-69. https://doi.org/10.1016/j.mri.2015.11.003

[18] Rowe, D. B. and Logan, B. R. *A complex way to compute fMRI activation.* Neuroimage. 23(3):1078-92. https://doi.org/10.1016/j.neuroimage.2004.06.042

[19] Rowe, D. B., Nencka, A. S., Jesmanowicz, A., and Hyde, J. S. *Separation of two simultaneously encoded slices with a single coil.* In Proc Intl Soc Magn Reson Med. Vol. 21, p. 0123.

[20] Redzian, R., Mansfield, P., and Doyle, M. *Real-time nuclear magnetic resonance clinical imaging in pediatrics.* Lancet. 322:1281-2. 10.1016/S0140-6736(83)91153-4.

[21] Sakitis, C. J., Brown, D. A., and Rowe, D. B. *A Bayesian complex-valued latent variable model applied to functional magnetic resonance imaging.* Journal of the Royal Statistical Society Series C: Applied Statistics. 74(1), 100-125. https://doi.org/10.1093/jrsssc/qlae046.

[22] Setsompop, K., Gagoski, B. A., Polimeni, J. R., Witzel, T., Wedeen, V. J., and Wald, L. L. *Blipped-controlled aliasing in parallel imaging (blipped-CAIPI) for simultaneous multi-slice EPI with reduced g-factor penalty.* Magn Reson Med. 67(5): 1210-1224. https://doi.org/10.1002/mrm.23097.

[23] Souza, S. P., Szumowskim, J., Dumoulin, C. L., Plewes, D. P., and Glover, G. *SIMA - simultaneous multislice acquisition of MR images by Hadamard-encoded excitation.* J Comput Assist Tomogr. 12:1026–1030.

[24] Stehling, M. K., Turner, R., and Mansfield, P. *Echo-planar imaging: magnetic resonance imaging in a fraction of a second.* Science. 254(5028), 43-50. DOI: 10.1126/science.1925560.

[25] Welvaert, M. and Rosseel, Y. *On the Definition of Signal-To-Noise Ratio and Contrast-To-Noise Ratio for fMRI Data.* J PloS ONE. 8(11): e77089. https://doi.org/10.1371/journal.pone.0077089.

[26] Xu, K., and Rowe, D. B. *A Bayesian CAIPIVAT approach with through-plane acceleration to enhance efficiency of simultaneously encoded slice acquisition in FMRI..* Magnetic Resonance Imaging. 110540. https://doi.org/10.1016/j.mri.2025.110540.

Highlights

A Bayesian Approach to 2D Acceleration for Studying Activation Detection Rate for Simultaneously Encoded Slice Acquisition in FMRI

Ke Xu, Daniel B. Rowe

- The efficiency of an fMRI study relies on how rapidly the image is acquired.

- In-plane and through-plane acceleration combine to reduce scan time.

- The novel SMS model is presented in a Bayesian manner using pre-scan calibration data.

- Task signal detection depends on image shift direction, brain size, and task signal location.

A Bayesian Approach to 2D Acceleration for Studying Activation Detection Rate for Simultaneously Encoded Slice Acquisition in FMRI

Ke Xu[a], Daniel B. Rowe[a,*]

[a]*Computational Mathematical and Statistical Sciences, Marquette University, 1313 W Wisconsin Ave, Milwaukee, 53233, WI, USA*

Abstract

Functional Magnetic Resonance Imaging (fMRI) enables researchers to study brain function and advance understanding in human sciences. Spatial and temporal changes in brain metabolism as by detecting the Blood Oxygen Level Dependent (BOLD) contrast signal are represented in the frequency domain of an image, known as k-space. Traditional MRI methodologies require full k-space information, which follows a unique data acquisition sequence to reconstruct the complete image. This process presents a time-consuming obstacle for medical imaging techniques. Our study proposes a novel image reconstruction method to enhance the efficiency of data acquisition while maintaining high accuracy in activation detection. The through-plane and in-plane acceleration techniques are combined to accelerate image acquisition along two dimensions. Multiple image-shift strategies and a 2D Hadamard encoding scheme are used to increase encoding diversity and reduce slice leakage. By applying our approach to both simulated and experimental fMRI data, we successfully reduced total scan time while achieving a higher signal-to-noise ratio (SNR) and contrast-to-noise ratio (CNR) in regions of interest (ROI). Compared with conventional reconstruction strategies, the proposed method demonstrates potential improvements in activation detection under specific acceleration and encoding conditions, while also providing voxel-wise estimates through a Bayesian framework.

Keywords:

---

*Corresponding author.
   Email address: `daniel.rowe@marquette.edu` (Daniel B. Rowe)

1. Introduction

1.1. Complex-Valued Bayesian Model

Functional magnetic resonance imaging (fMRI) studies can be interpreted following the Bayesian methodology but with complex-valued observations. To set up a complex-valued Bayesian linear model, the complex-valued observation can be written as Eq. 1:

$$a_C = X_C \beta_C + \varepsilon_C. \tag{1}$$

In Eq. 1, a_C is a $p \times 1$ complex-valued observed vector, X_C is a $p \times q$ complex-valued known design matrix, β_C is a $q \times 1$ complex-valued unobserved regression coefficient vector, and ε_C is a complex-valued measurement error vector with same dimension as vector a_C, where p is the number of observations, and q is the number of regression coefficients. Moreover, the real and imaginary component of the measurement error ε_C follow normal distribution with $\varepsilon_R, \varepsilon_I \sim N(0, \sigma^2 I_p)$. In the application of this study, a_C is the complex-valued observed coil measurements vector, X_C is the complex-valued observed coil sensitivity matrix, and β_C is the unobserved voxel values vector. Eq. 1 can be reformulated through a real-valued isomorphism to transform the complex-valued model into a real-valued model:

$$\begin{bmatrix} a_R \\ a_I \end{bmatrix} = \begin{bmatrix} X_R & -X_I \\ X_I & X_R \end{bmatrix} \begin{bmatrix} \beta_R \\ \beta_I \end{bmatrix} + \begin{bmatrix} \varepsilon_R \\ \varepsilon_I \end{bmatrix}. \tag{2}$$

In Eq. 2, the dimension of observation vector $a = [a_R; a_I]$ is $2p \times 1$, the dimension of design matrix $X = [X_R, -X_I; X_I, X_R]$ is $2p \times 2q$, the dimension of regression coefficient vector $\beta = [\beta_R; \beta_I]$ is $2q \times 1$, and the dimension of measurement error vector $\varepsilon = [\varepsilon_R; \varepsilon_I]$ is $2p \times 1$. ~~Thus, the likelihood distribution of the multivariate observation is:~~

$$P(a \mid X, \beta, \sigma^2) \propto (\sigma^2)^{-\frac{2p}{2}} \exp\left[-\frac{1}{2\sigma^2}(a - X\beta)'(a - X\beta) \right], \tag{3}$$

~~with independent and identical distributed (iid) observation, error for the normal distribution $a \sim N(X\beta, \sigma^2 I_{2p})$. In the linear regression model, the~~

regression coefficients (voxel values) can be estimated through maximum likelihood estimation (MLE):

$$\hat{\beta}_{MLE} = (X'X)^{-1}X'a \tag{4}$$

And the estimated variance through MLE is:

$$\hat{\sigma}^2_{MLE} = \frac{1}{2p}(a - X\hat{\beta})'(a - X\hat{\beta}). \tag{5}$$

To enhance anatomical detail and improve the resolution of reconstructed images, calibration images can be incorporated as prior information. The Tikhonov regularization algorithm has been shown to effectively increase the signal-to-noise ratio (SNR) (Lin et al. [12]). However, careful selection of the regularization parameter λ is crucial for optimal performance. In this paper, we propose a Bayesian complex-valued image reconstruction algorithm. Compared with Tikhonov regularization, the Bayesian framework enables principled use of calibration data and provides posterior estimates. This facilitates the construction of confidence intervals and hypothesis testing. As a result, inter-slice signal leakage can be eliminated, and correlations between reconstructed slices can be reduced. Based on prior knowledge and experience, the regression coefficient β (voxel values) is specified to have a normal prior distribution $P(\beta \mid \sigma^2)$, and the measurement error σ^2 is specified to have an inverse gamma prior distribution $P(\sigma^2 \mid \cdot)$. Thus, the posterior distribution of regression coefficient β and variance σ^2 is proportional to the joint distribution of the likelihood and the prior distributions:

$$P(\beta, \sigma^2 \mid \cdot) \propto P(a \mid X, \beta, \sigma^2)P(\beta \mid \sigma^2)P(\sigma^2 \mid \cdot). \tag{6}$$

The joint posterior distribution of the regression coefficient β (voxel values) and measurement error σ^2 can be integrated to obtain their marginal distributions and hence their marginal posterior mean (MPM) and variance. More details are provided in Section 2. In this study, the complex-valued Bayesian reconstruction framework constitutes the central conceptual component of the proposed methodology, and its formulation is presented in detail in Section 2. The simulation and experimental analyses described in Sections 4 and 5 are designed to evaluate the performance of this framework, particularly in terms of activation detection stability, noise propagation, and reconstruction robustness under different image-shift strategies and acceleration factors. Limitations of the current approach and potential directions for future research are discussed in Section 6.
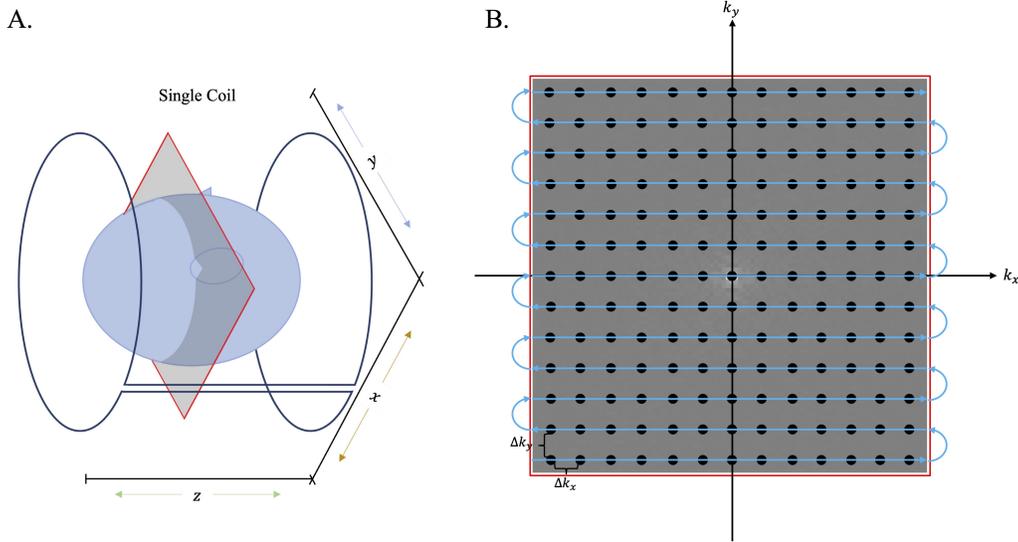
3

Figure 1: A. The three-dimensional view of brain image acquisition process with one single coil. B. The zig-zag data collecting pattern of GRE-EPI pulse sequence.

1.2. FMRI Background

In the functional magnetic resonance imaging (fMRI) study field, the topic of improving the efficiency of data acquisition in the image scanning process has been gaining researchers' interest since 1990. As a noninvasive medical imaging technique, the blood-oxygen-level dependent (BOLD) contrast signal is detected as the proxy reflecting neuron activation changes over time (Ogawa et al. [14]). In order to acquire the fully sampled spatial frequency space, known as k-space, the gradient echo echo-planar imaging (GRE-EPI) pulse sequence is applied to shorten the scan time and reduce the respiratory artifacts within a single excitation (Mansfield [13]; Redzian et al. [20]; Stehling et al. [24]). Fig. 1 illustrates a three-dimensional view of the brain image scanning process and the unique data acquisition sequential pattern in the k-space of the GRE-EPI pulse sequence (Sakitis et al. [21]). However, conducting an fMRI experiment requires acquiring multiple brain images at multiple slices, forming what is known as a volume-image.

In 1986, Hyde introduced a parallel image acquisition technique that incorporated multiple coils, with each coil measuring partial sensitivity-weighted spatial frequencies (Hyde et al. [7]). A full brain image can be reconstructed by applying the Sensitivity Encoding (SENSE) approach to combine weighted

spatial frequencies from each coil into one single k-space array (Pruessmnn et al. [15]). In order to reduce the total image scan time, the data acquisition can be accelerated along two dimensions: the in-plane dimension and the through-plane dimension. The in-plane acceleration (IPA) method aims at expediting the single slice readout process by skipping partial lines in the k-space. As an alternative to SENSE, the unacquired spatial frequency points can be estimated by the application of the generalized autocalibrating partially parallel acquisition (GRAPPA) approach (Griswold et al. [6]). Prior information of missing data in the k-space can be obtained from the calibration images. Fig. 2A illustrates the brain image acquisition process with four receiver coils and the subsampled spatial frequency domain for IPA approach with acceleration factor IPA=2 (Sakitis et al. [21]). However, the total scan time does not decrease proportionally to the IPA factor due to fixed time blocks in the data acquisition process, such as proper time to form T_2^* contrast and imaging encoding time in a single excitation. The through-plane acceleration (TPA) approach, on the other hand, accelerates the image acquisition process by acquiring multiple slices simultaneously in one excitation. Techniques such as the simultaneous multi-slice (SMS) approach can be incorporated with the TPA approach by applying a multiband (MB) radiofrequency (RF) pulse within a reduced repetition time (TR) (Souza et al. [23]; Rowe et al. [19]; Barth et al. [1]; Rowe et al. [17]; Xu and Rowe. [26]). Compared to the IPA approach, the TPA approach significantly improves the efficiency of data acquisition, as the total scan time is reduced by a fraction corresponding to the TPA acceleration factor. While the mSPECS-CAIPIVAT (Xu and Rowe. [26]) framework proposed primarily focused on through-plane acceleration and the feasibility of Bayesian slice separation, the present work extends that framework in several important directions. First, the current study introduces a unified two-dimensional acceleration framework that jointly considers both through-plane and in-plane acceleration. Second, a novel 2D Hadamard phase encoding strategy is incorporated to increase encoding diversity and improve reconstruction stability under aggressive acceleration. Third, the present work systematically investigates the influence of image-shift direction and acceleration factors on activation detection performance using both simulated and experimental fMRI data. Therefore, the objective of this study is not merely to extend the previous Bayesian reconstruction model, but to evaluate how the Bayesian framework behaves under different encoding and acceleration conditions relevant to activation detection in fMRI studies.
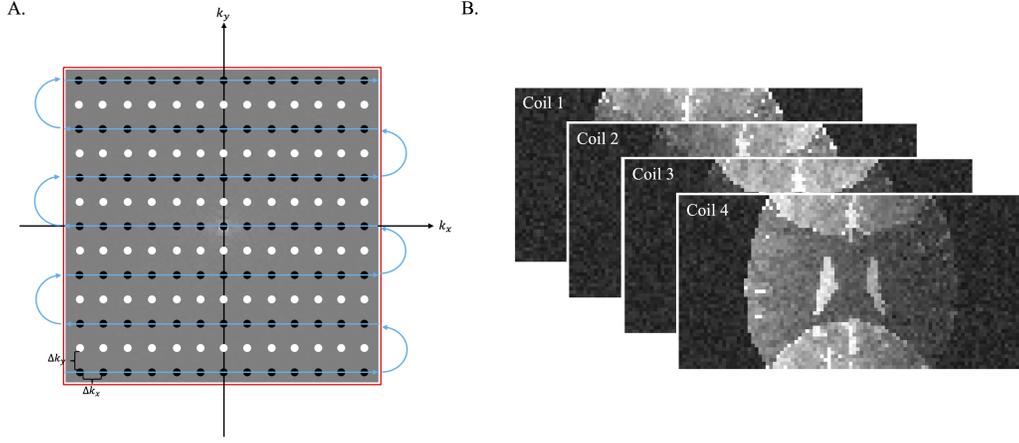
5

Figure 2: A. The subsampled spatial frequency domain incorporated with IPA approach and the acceleration factor equal to 2. B. The subsampled acquired images from four receriver coils.

To further reduce the total image scan time and achieve the ultimate goal of our study, we introduce a novel SMS image reconstruction technique called "a controlled aliasing in parallel imaging with view angle tilting approach and in-plane acceleration method for multi-coil separation of parallel encoded complex-valued slices" (mSPECS-IPA-CAIPIVAT), which will be presented and discussed. This approach builds upon the mSPECS-IPA method by integrating both TPA and IPA acceleration techniques into a unified 2D acceleration technique (Kociuba [9]). By leveraging 2D acceleration, a higher acceleration factor can be achieved. Several encoding strategies have been proposed to improve slice separation in accelerated SMS imaging, including Controlled Aliasing in Parallel Imaging Results in Higher Acceleration (CAIPIRINHA) and View Angle Tilting (VAT). These techniques introduce controlled spatial shifts in the phase-encoding or readout direction to increase encoding diversity and reduce slice leakage in multi-slice acquisitions. In this novel image reconstruction method, we incorporate an image shift technique into the model to reduce the similarity of coil sensitivity information for aliased voxels, thereby improving image reconstruction accuracy.

2. Theory

2.1. The Data Acquiring Process

2.1.1. Image Shift Techniques

As discussed in Section 1.2, the SMS technique enables the concurrent acquisition of multiple brain slice images, reducing the total volume scan time depending on the selected TPA factor. Fig. 3 illustrates both 3D and 2D views of the image acquisition process with four slices and four coils. Unlike single-slice acquisition, multi-slice acquisition results in a short physical distance between aliased images. When applying the SENSE algorithm to reconstruct brain images and capture activity signals, an ill-conditioned matrix problem arises due to the high similarity of coil sensitivity information between closely spaced aliased voxels. Consequently, strong inter-slice signals and anatomical structures from other slices may appear as artifacts in the reconstructed images. To eliminate those stray anatomical artifacts from other slices on the reconstructed brain images, decreasing the similarity of the coil sensitivity information is the primary strategy. Therefore, we introduced the images shift techniques to manually increase the physical distance between aliased images. To assess the performance of the image reconstruction method at high acceleration factors, we define the noise amplification factor, also known as the geometry factor (g-factor), as described in (Setsompop et al. [22]; Welvaert and Rosseel. [25]):

$$g_{SMS} = \frac{SNR_{full}}{SNR_{accelerate}\sqrt{R}}. \tag{7}$$

In Eq. 7, SNR_{full} is the signal-to-noise (SNR) ratio for the reconstructed images from techniques without acceleration factors and image shift techniques, and it can be assessed from the calibration images. $SNR_{accelerate}$ is the SNR value for the reconstructed images with acceleration factors, and the IPA acceleration factor R indicates the omission of spatial frequency data along the phase encoding direction. The closer the value of g_{SMS} is to 1, the better the reconstruction quality of the accelerated method. According to Eq. 7, high similarity of coil sensitivity information induces the high g_{SMS} value, which leads to a reduction of the $SNR_{accelerate}$ for the reconstructed images. Thus, to increase the $SNR_{accelerate}$ value and improve the performance of the novel acceleration technique, three image shift techniques have been incorporated.

In fMRI studies, the brain image can be shifted along three directions: the phase-encoding (PE) direction (vertically in this study), the readout (RO)
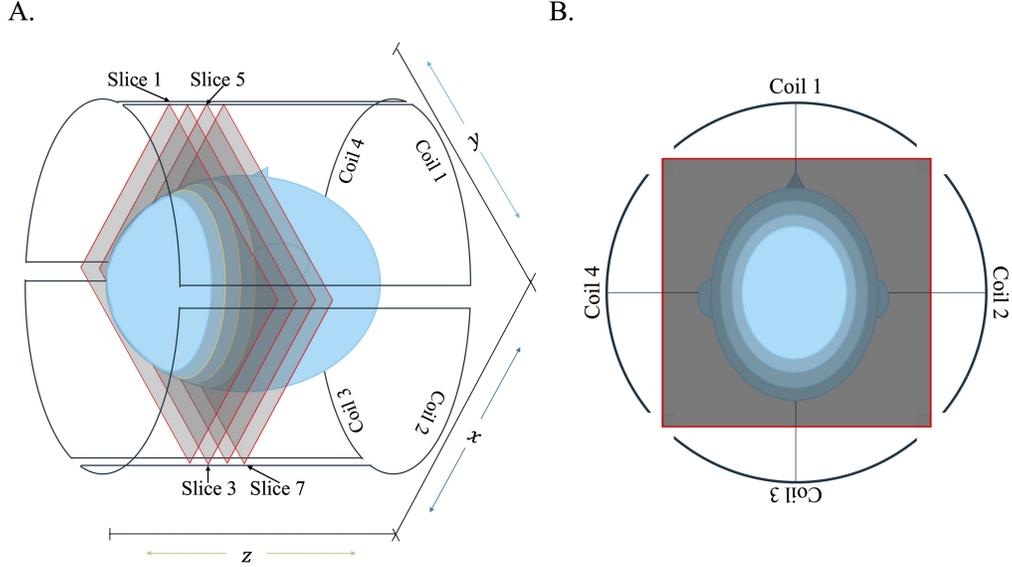
Figure 3: A. The 3D view of SMS technique with four slices and four coils acquisition process at one excitation. B. The 2D view for the same process with four slices and four coils.

direction (horizontally in this study), and PE and RO direction concurrently (vertically and horizontally at the same time in this study). To decrease the influence of the geometric properties of the coil sensitivity maps, techniques like "controlled aliasing in parallel imaging results in higher acceleration" (CAIPIRINHA) and "blipped-CAIPIRINHA" (Blipped-CAIPI) provide other possible ways to minimize the influence of the g-factor and maximize the physical distance of the aliased voxels (Breuer et al. [2]; Setsompop et al. [22]). The CAIPIRINHA approach can shift the images along the PE direction by modulating the phase for each line in the k-space and imparting each line with a specific phase. Applying a unique phase modulation amount to each slice in the aliased image-acquiring process increases the physical distance between the aliased voxels. Therefore, the independence of coil sensitivity for each slice will increase, and the influence of the g-factor for each excitation will be minimized. Moreover, to shift the brain image along the RO direction, a technique like the view angle tilting (VAT) approach applies compensation gradients to the slice selection direction to correct the chemical-shift artifacts in the image scanning process (Cho et al. [3]; Kim et al. [11]). The distance shifted along the RO direction is related to the view

angle θ in the data acquisition process. The CAIPIRINHA and the VAT technique can be combined, and thus the study "multislice CAPIPRINHA using view angle tilting technique" (CAIPIVAT) proposed (Jungmann et al. [8]; Kim et al. [10]). Through this technique, the field-of-view (FOV) can be shifted along the PE and RO direction by applying different amounts of phase modulation to each line in the k-space and the compensation gradients on the slice selection direction together for each excitation. The GRE-EPI pulse sequence of the CAIPIRINHA, Blipped-CAIPI, and CAIPIVAT models could be investigated according to their respective references. Although the Blipped-CAIPI method compliments the VAT and the Hadamard encoding techniques, to further increase the diversity of the information in the image acquisition process, we introduced the 2D Hadamard phase encoding technique and discussed the combination with CAIPIRINHA, VAT and CAIPIVAT technique. Fig. 4 shows the k-space for CAIPIRINHA, VAT and CAIPIVAT techniques along the reconstructed brain images after the inverse Fourier transform.

2.1.2. 2D Hadamard Phase Encoding

The traditional Hadamard encoding technique is a well-developed volume-image method and widely used in fMRI studies (Souza et al. [23]). The conventional magnetic resonance (MR) imaging techniques have been limited by the size of the matrix for the acquired aliased images. The traditional Hadamard phase encoding method allows the increment of the size of the acquired aliased image matrix by aliasing in both frequency and phase encoding dimensions. With the support of this simultaneous binary-encoded technique, the TR will decrease, and the SNR ratio will improve. The Hadamard matrix is given by:

$$H_{2^n} = \begin{bmatrix} H_{2^{n-1}} & H_{2^{n-1}} \\ H_{2^{n-1}} & -H_{2^{n-1}} \end{bmatrix} = H_2 \otimes H_{2^{n-1}}, \text{where } H_1 = \begin{bmatrix} 1 \end{bmatrix}, H_2 = \begin{bmatrix} 1 & 1 \\ 1 & -1 \end{bmatrix}, \tag{8}$$

where $\otimes$ denotes the Kronecker product. It is an orthogonal and full rank matrix with elements of either +1 or -1. The Hadamard phase encoding technique can be applied not only to through-plane imaging scenario but also to in-plane imaging scheme. The entire FOV can be divided into various regions of interest by applying Walsh functions during the pre-encoding section to define the frequency profile that the Hadamard pulses must follow (Fletcher et al. [5]).
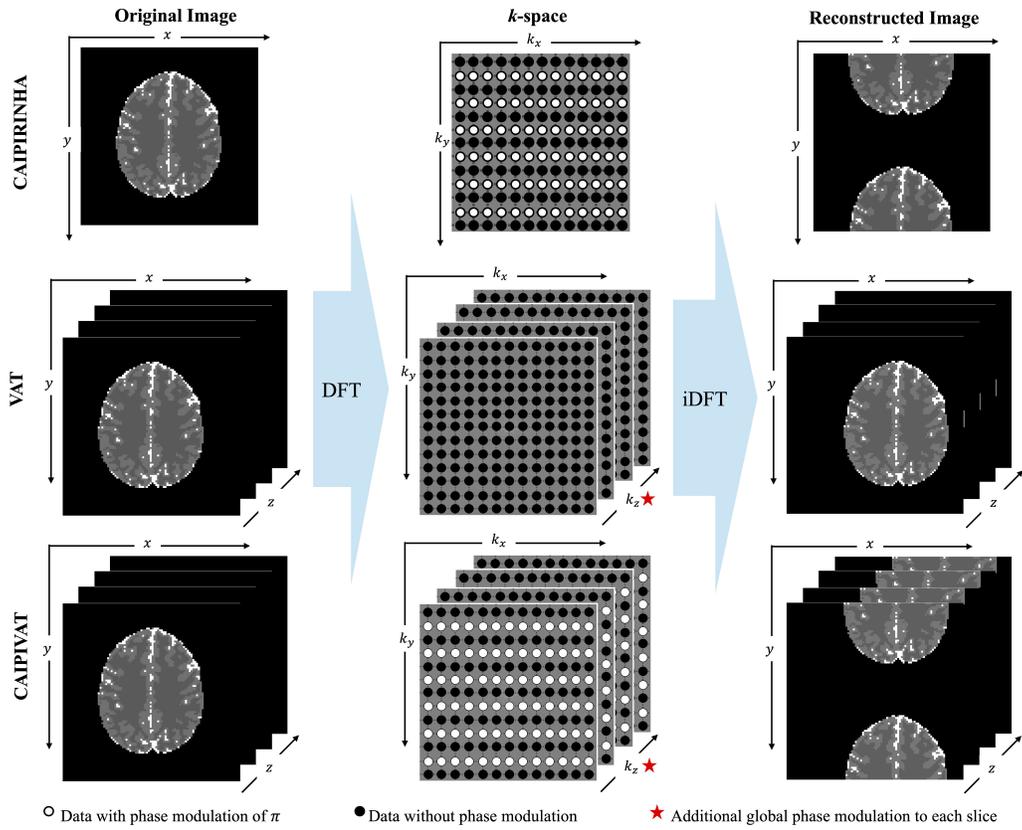
Figure 4: Top row: the image shift process corresponding to the CAIPIRINHA technique (shifted vertically). Middle row: the image shift process corresponding to the VAT technique (shifted horizontally). Bottom row: the image shift process corresponding to the CAIPIVAT technique (shifted vertically and horizontally).

In this study, since the TPA approach and the IPA approach are combined to further decrease the total image scan time, and the image shift techniques are incorporated to decrease the influences of the geometry properties, we introduce a novel 2D Hadamard phase encoding technique to our approach. The novel 2D Hadamard phase encoding technique is developed and based upon the Hadamard phase encoding technique with elements of either $+1$ or -1. However, different from the traditional Hadamard phase encoding technique, in order to guarantee the orthogonality property for each aliased image, different 2D Hadamard coefficients will be assigned to different segments for different slices. Fig. 5 shows the 2D Hadamard phase encoding aliasing coefficient for $N_s = 2$ and $N_s = 4$ scenarios, where N_s is the number of aliased slices for each excitation. First, for each excitation or each TR, the through-plane Hadamard coefficient will be assigned to different slices. Second, for each segment of each slice, the in-plane Hadamard coefficient will be assigned to a different excitation. To maintain the orthogonality property for each segment of each slice, the in-plane Hadamard coefficient starts from the second column of the Hadamard coefficient for the first excitation. At the last TR of the cycle, the in-plane Hadamard coefficient is the first column of the Hadamard matrix. Finally, the 2D Hadamard coefficient will be the product of the through-plane and in-plane Hadamard coefficient for each segment of each slice and each excitation. The size of the in-plane and through-plane Hadamard coefficient matrix is equal to the number of aliased slices, N_s, for each excitation.

2.1.3. The Combination of Image Shift Techniques and 2D Hadamard Phase Encoding

To accomplish the goal of decreasing the coil sensitivity information similarity of aliased voxels, and thus decreasing the influence of the g-factor, we combined the image shift techniques and the 2D Hadamard phase encoding technique together. Fig. 6 shows the image shift scenario corresponding to different SMS techniques for the first 4 TRs along with the 2D Hadamard coefficients for each segment of the slices under the circumstance with $N_s = 4$. Compared with the mSPECS-IPA method (Fig. 6A), the other three methods are incorporated with different image shift directions and amount for each slices and each excitation. Fig. 6B shows the image shift scenario along with the 2D Hadamard coefficients incorporating with the mSPECS-IPA-CAIPIRINHA method. For each slice within each TR, a $\Delta y = (l - 1)FOV/N_s$ of in-plane image shift on the verti-
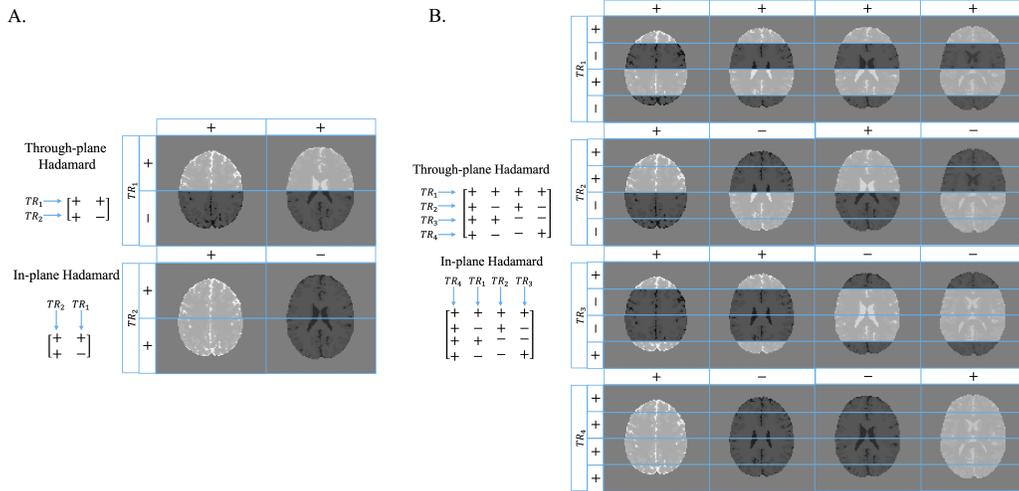
11

Figure 5: A. The 2D Hadamard phase encoding coefficient for $N_s = 2$. B. The 2D Hadamard phase encoding coefficient for $N_s = 4$.

cal direction will be imparted, where $l = 1, \ldots, N_s$. For each excitation, a $\Delta y = (m-1)FOV/N_s$ of in-plane image shift on the vertical direction will be imparted, where $m = 1, \ldots, N_s$. Thus, with the in-plane and the through-excitation CAIPIRINHA image shift, the voxel aliasing scenario at $TR_{N_s} + 1$ will be identically same as aliasing scenario at TR_1. Fig. 6C shows the image shift scenario along with the two-dimensional Hadamard coefficients incorporating with the mSPECS-IPA-VAT method. Unlike the mSPECS-IPA-CAIPIRINHA method, the mSPECS-IPA-VAT method only shift the image along the horizontal direction. Thus, for each excitation and each slice, no image shift occurs along the vertical direction, but a modest amount of image shift will be applied for each slice and each excitation along the horizontal direction. Fig. 6D shows voxel aliasing scenario incorporated with the mSPECS-IPA-CAIPIVAT method. Since the mSPECS-IPA-CAIPIVAT method is combining the principle idea of mSPECS-IPA-CAIPIRINHA and mSPECS-IPA-VAT method together, the image shift will occur along the vertical and the horizontal direction. For each slice within each excitation, a $\Delta y = (l-1)FOV/N_s$ amount of the image shift along the vertical direction, where $l = 1, \ldots, N_s$, and the amount of the image shift technique corresponding to the VAT technique along the horizontal direction will be imparted. Moreover, for each excitation, a $\Delta y = (m-1)FOV/N_s$ of image shift will be imparted along the vertical direction, where $m = 1, \ldots, N_s$. In
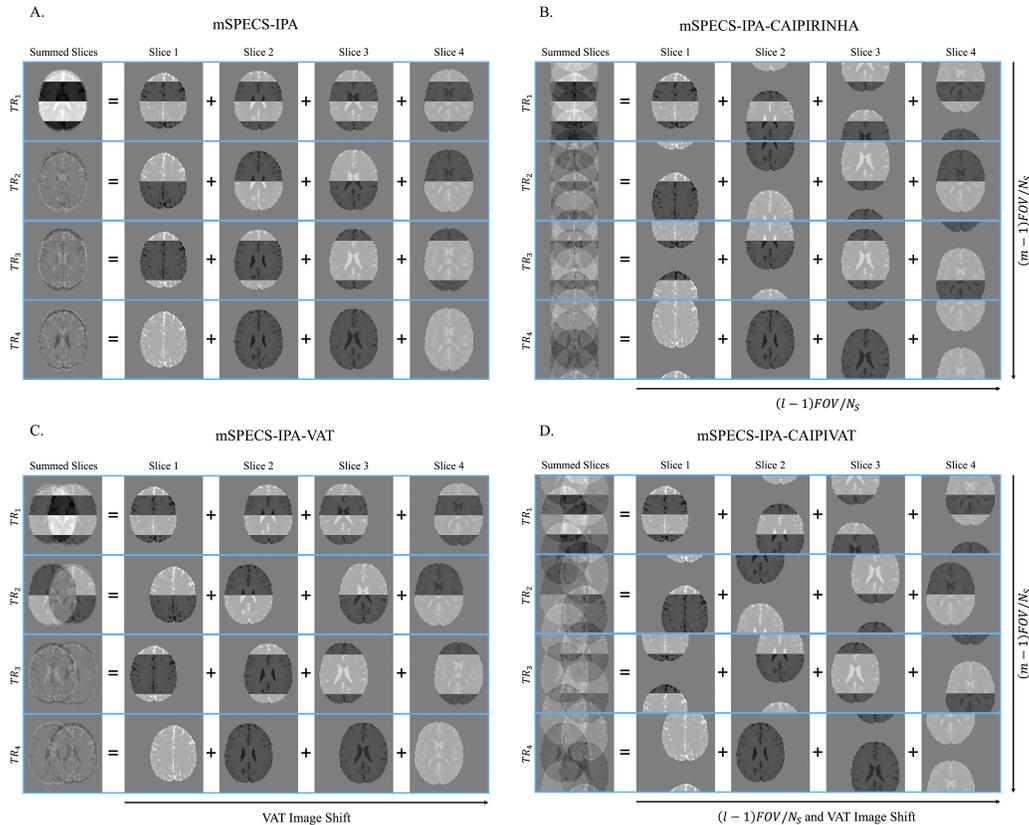
Figure 6: The voxel aliasing scenario for the first 4 TRs with $N_s = 4$ circumstance incorporating with A. mSPECS-IPA image shift technique, B. mSPECS-IPA-CAIPIRINHA technique, C. mSPECS-IPA-VAT technique, and D. mSPECS-IPA-CAIPIVAT technique.

real-world volume image acquisition, the 2D Hadamard phase-encoding technique should be applied before the image shift techniques (Fletcher et al. [5]). A careful design of the Hadamard pre-encoding process is necessary to ensure the orthogonality of the 2D Hadamard aliasing coefficients. Comparing these four image shift techniques, the overlapping area between summed slices are decreasing from the mSPECS-IPA method to the mSPECS-IPA-CAIPIVAT method. However, since the novel proposed SMS technique is aiming at combining TPA and IPA technique together, thus, making the voxel aliasing scenario clear after the IPA technique is another vital process to discuss in this paper.

Fig. 7 displays the voxel aliasing scenario after the IPA aliasing tech-
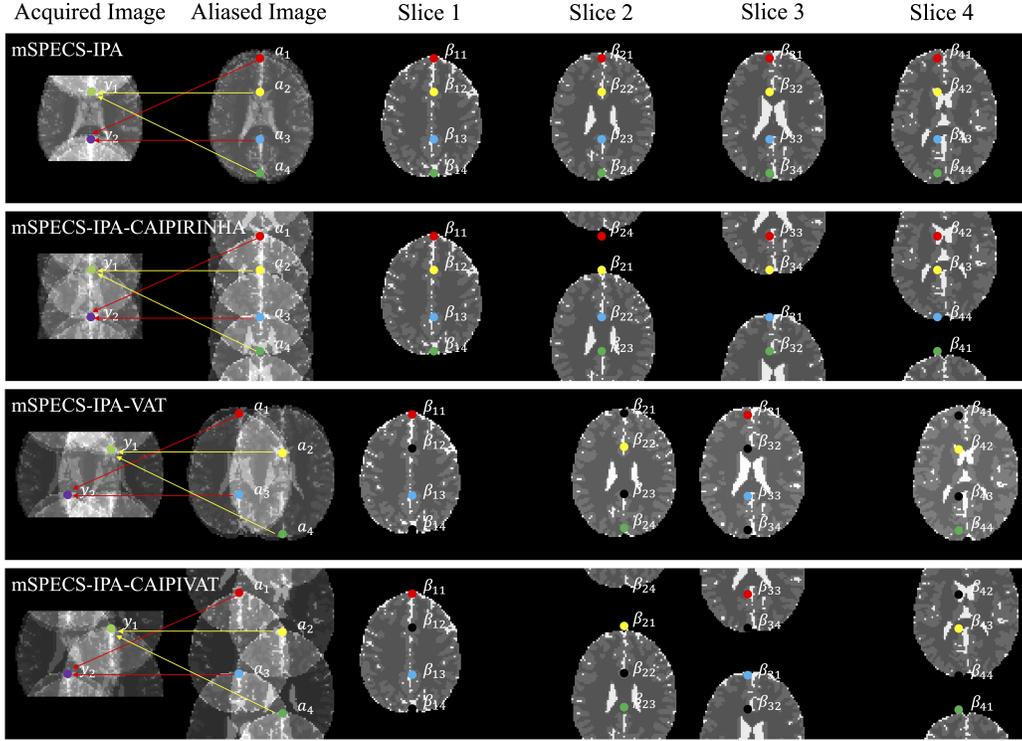
13

Figure 7: The voxel aliasing scenario with $N_s = 4$ for mSPECS-IPA, mSPECS-IPA-CAIPIRINHA, mSPECS-IPA-VAT and mSPECS-IPA-CAIPIVAT technique.

nique for mSPECS-IPA, mSPECS-IPA-CAIPIRINHA, mSPECS-IPA-VAT, and mSPECS-IPA-CAIPIVAT technique under the circumstance with $N_s = 4$. In Fig. 7, those dots in the same color indicating voxels are aliased together. From the top model to the bottom model, the physical distance between aliased voxels increases, leading to reduced coil information similarity and, consequently, a lower g-factor. Moverover, comparing the mSPECS-IPA and the mSPECS-IPA-CAIPIRINHA method, after the IPA acceleration technique, the mSPECS-IPA-CAIPIRINHA has the more complex aliasing artifacts and the overlapping area is larger than the mSPECS-IPA method especially at the center part of the acquired images. Comparing the bottom two methods, mSPECS-IPA-VAT and the mSPECS-IPA-CAIPIVAT technique, the similar conclusion can be made. In this work, the combination of image shift techniques and 2D Hadamard phase encoding was not implemented experimentally, as this is a methodological study. Instead, we

utilized fully sampled k-space data, and the slices were artificially Hadamard encoded and aliased.

2.2. A Single Aliased Voxel

Given an excitation δ in the fMRI time series, we define $IS_{\delta,z}$ notation indicating the image shift pattern for the zth slice and the δth TR, corresponding to one of the mSPECS-IPA, mSPECS-IPA-CAIPIRINHA, mSPECS-IPA-VAT and the mSPECS-IPA-CAIPIVAT technique, and it follows the definition in Section 2.1.1. Thus, for a single aliased voxel at the location (x, y) of the acquired aliased images with TPA and IPA acceleration techniques, corresponding to the 2D Hadamard coefficients at time point δ, measured at jth coil, is defined as the summation equation:

$$a_{j,\delta} = \sum_{k=1}^{IPA} \sum_{z=1}^{N_s} H_{\delta,z,k} S_{IS_{\delta,z},k} \beta_{IS_{\delta,z},k} + \varepsilon_{j,\delta}. \tag{9}$$

In Eq. 9, the acquired aliased voxel value $a_{j,\delta}$ is a complex-valued data with real and imaginary component, $a_C = a_R + ia_I$, and parameter k is the IPA indicator. The 2D Hadamard coefficient, $H_{\delta,z,k}$, is a real-valued orthogonal matrix corresponding to the δth excitation, zth slice and the kth IPA process, and it strictly follows the definition of the 2D Hadamard phase encoding in Section 2.1.2. All of the element of the $H_{\delta,z,k}$ coefficient matrix is either $+1$ or -1. The coil sensitivity information matrix, $S_{IS_{\delta,z},k}$, is a complex-valued data point with real and imaginary component, $S_C = S_R + iS_I$, corresponding to the kth IPA process and the image shift process at δth excitation and zth slice. The true voxel value, $\beta_{IS_{\delta,z},k}$, is a complex-valued data point with real and imaginary component, $\beta_C = \beta_R + i\beta_I$, corresponding to the kth IPA process and the image shift process at δth excitation and zth slice. The measurement error, $\varepsilon_{j,\delta}$, is also a complex-valued data point with real and imaginary component, $\varepsilon_C = \varepsilon_R + i\varepsilon_I$, corresponding to the δth time point and jth coil. Moreover, the real and imaginary component of measurement error is specified to be a normal distribution with mean $E(\varepsilon_R) = E(\varepsilon_I) = 0$ and variance $var(\varepsilon_R) = var(\varepsilon_I) = \sigma^2$.

Considering the acquired aliased voxel in Eq. 9 across total N_c coils, N_α time points and the N_s slices in the whole fMRI time series, the real-valued isomorphic representation of Eq. 9 can be expressed similar to Eq. 1:

$$a = X_A \beta + \varepsilon. \tag{10}$$

In Eq. 10, $a = [a_R; a_I]$ is a real-valued vector with dimension $2N_cN_\alpha \times 1$. The real-valued aliasing matrix $X_A = [(X_A)_R, -(X_A)_I; (X_A)_I, (X_A)_R]$ is known prior information including the 2D Hadamard coefficients and the coil sensitivity information across the N_c coils, N_α time points and the N_s slices. Thus, the dimension of the aliasing matrix X_A is $2N_cN_\alpha \times 2N_s$. For the δth excitation, the known aliasing matrix $(X_A)_\delta$ across N_c coils and N_s slices is defined as:

$$(X_A)_\delta = \left[H_{\delta,1} \begin{pmatrix} S_{1,1} \\ \vdots \\ S_{N_c,1} \end{pmatrix}, \dots, H_{\delta,N_c} \begin{pmatrix} S_{1,N_s} \\ \vdots \\ S_{N_c,N_s} \end{pmatrix} \right]. \tag{11}$$

Across the N_α excitations, the Eq. 11 can be expressed as:

$$X_A' = \left[(X_A)_1', \dots, (X_A)_{N_\alpha}' \right]. \tag{12}$$

The true voxel value in Eq. 10, $\beta = [\beta_R; \beta_I]$, is a vector we want to estimate, with dimension $2N_s \times 1$. The measurement error in Eq. 10, $\varepsilon = [\varepsilon_R; \varepsilon_I]$ has the same dimension as the a vector. The real and imaginary component of the measurement error is specified to be normal distributed with mean $E(\varepsilon) = 0$ and covariance $cov(\varepsilon) = \sigma^2 I_{2N_cN_\alpha}$, where $I_{2N_cN_\alpha}$ is the identity matrix.

Thus, in order to separate the aliased images and estimate the true voxel value for each slice, the maximum likelihood estimation in Eq. 4 can be applied and the estimated voxel value, $\hat{\beta}_{MLE}$, can be calculated by:

$$\hat{\beta}_{MLE} = \left(X_A' X_A \right)^{-1} X_A' a. \tag{13}$$

Moreover, the covariance of the voxel value $\hat{\beta}$, can be estimated by:

$$cov(\hat{\beta}_{MLE}) = \sigma^2 \left(X_A' X_A \right)^{-1}. \tag{14}$$

According to the methodology of the combination of image shift techniques and the 2D Hadamard phase encoding technique, the novel proposed SMS method accelerates the image acquiring process along the TPA and the IPA dimension. However, the relative short scan time leads to less data information collected during the image acquiring process compared with the traditional imaging technique without acceleration techniques. Furthermore,

it also leads to an ill-conditioning of the designed aliasing matrix which will cause failure to calculate the inverse of $X'_A X_A$. Thus, coming up with a technique that is capable to fix the ill-condition designed matrix problem and hence calculate the inverse problem is the next priority. In this study, we introduce the bootstrap sampling technique along with the artificial aliasing of the calibration images technique to solve this problem. By applying these two techniques into the novel image shift SMS technique, the designed aliasing matrix is made to be full rank and invertible and the inter-slice signal leakage can be eliminated.

2.3. The Bootstrap Sampling and Artificial Aliasing of Calibration Images

The Bayesian reconstruction model forms the conceptual foundation of this study. Unlike conventional SMS reconstruction techniques that provide deterministic voxel estimates, the proposed framework models the reconstruction problem probabilistically and incorporates calibration information through structured prior distributions. Based on the discussion in the previous sections, to make the designed aliasing matrix to be full rank and invertible, slices information from the calibration images can be utilized as the reference information. The bootstrap sampling technique is a widely used tool which can decrease the correlation induced by the image separation process and eliminate the inter-slice signal leakage. In the image separation process, for each excitation, the bootstrap sampling technique will be applied to the calibration images. The bootstrapping size for each excitation is related to the TPA factor, which is equal to the number of aliased slices for each excitation and the IPA factor. Thus, for each excitation in the fMRI time series, $N_s R$ bootstrapped sampled slices will be randomly chosen from the fully sampled calibration image time series. The randomly chosen slices will be averaged and the mean calibration images will be utilized for the artificial aliasing process. Although this results in a slightly larger variance than averaging all calibration images, it eliminates correlation between unaliased slices.

For each excitation, the same image shift pattern will be applied to both acquired aliased images and the artificial aliased calibration images. But different 2D Hadamard aliasing coefficient matrix will be applied to acquired aliased images and the artificial aliased calibration images. Fig. 8 shows the 2D Hadamard aliasing coefficient for acquired aliased slices (red box) and the artificial aliased calibration slices (blue box) for the first 4 TRs with $N_s = 4$. For each segment of each slice, the white part means the Hadamard
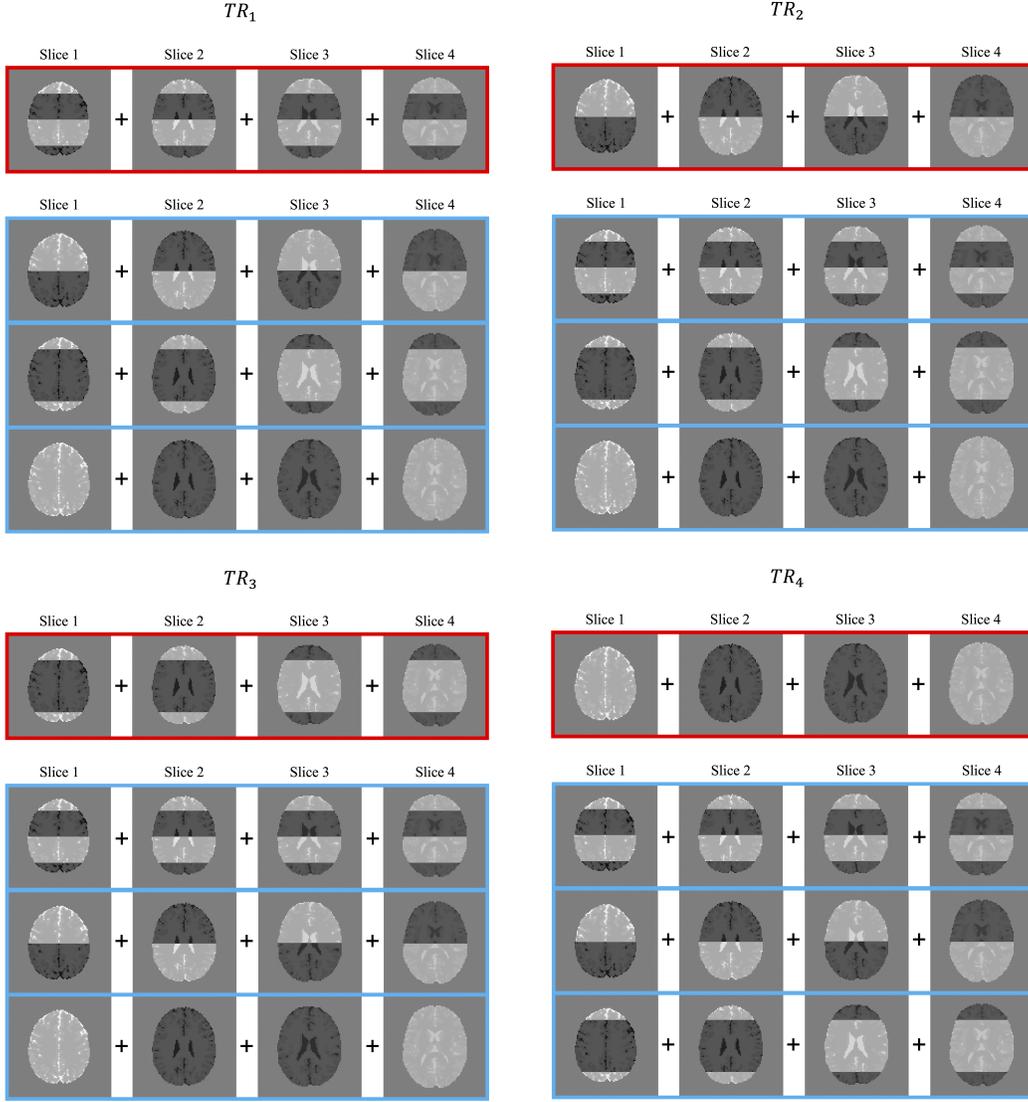
17

Figure 8: The the 2D Hadamard aliasing coefficients for acquired aliased slices (red box) and the artificial aliased calibration slices (blue box) for the first 4 TRs with $N_s = 4$.

coefficient is +1, and the black part means the Hadamard coefficient is -1. Moreover, the 2D Hadamard aliasing coefficient for acquired aliased slices and artificial aliased calibration slices at time point TR_{N_s+1} will be identical as TR_1. Based on the 2D Hadamard aliasing coefficients for acquired aliased slices and the artificial aliased calibration slices, for each excitation, $N_s - 1$

18

combinations of 2D Hadamard aliasing coefficient remain for the artificial aliasing process.

Similar to Eq. 10, for a single excitation, a single voxel, ν, from the artificial aliasing calibration aliased slices located at (x, y) across N_s slices, measured through N_c coils can be expressed as:

$$\nu = C\bar{\nu} = C_A\mu + C\eta. \tag{15}$$

In Eq. 15, the artificial aliased voxel value, $\nu = [\nu_R; \nu_I]$, is a vector with real and imaginary component and dimension $2N_s N_c(N_s - 1) \times 1$. The mean bootstrap sampled voxel, $\bar{\nu} = [\bar{\nu}_R; \bar{\nu}_I]$, is a vector with dimension $2N_s \times 1$. The true calibration voxel value, $\mu = [\mu_R; \mu_I]$, and the measurement error, $\eta = [\eta_R; \eta_I]$, have the same dimension with the mean bootstrap sampled voxel vector. Moreover, the mean of the measurement error is $E(C\eta) = 0$ and covariance is $cov(C\eta) = \tau^2 I_{2N_s N_c(N_s-1)}$ where $I_{2N_s N_c(N_s-1)}$ is the identity matrix. If the bootstrap sampling technique is not incorporated, *i.e.* the same calibration images are used in the model, then the covariance of the measurement error is $\tau^2 = 0$, thus a correlation between the reconstructed slices is induced solely by the image separation process. This is a very important result. However, with the assistance of the bootstrap sampling technique, $\tau^2 = \sigma^2$, and the covariance of the measurement error of the calibration image is $cov(C\eta) = \sigma^2 I_{2N_s N_c(N_s-1)}$. A small trade-off of increased variance for an elimination of correlation as shown later.

The artificial aliasing matrix, C_A in Eq. 15, is a known prior information including the 2D Hadamard coefficients for the artificial aliasing slices and the coil sensitivity information across N_c coils, N_α time points and N_s slices. Thus, the dimension of the artificial aliasing matrix, C_A, is $2N_s N_c(N_s - 1) \times 2N_s$. For the δth excitation, the known artificial aliasing matrix $(C_A)_\delta$ across N_c coils and N_s slices is defined as:

$$(C_A)_\delta = \left[\overline{H_{\delta,1}} \begin{pmatrix} S_{1,1} \\ \vdots \\ S_{N_c,1} \end{pmatrix}, \ldots, \overline{H_{\delta,N_c}} \begin{pmatrix} S_{1,N_s} \\ \vdots \\ S_{N_c,N_s} \end{pmatrix} \right]. \tag{16}$$

The notation $\overline{H}$ indicates the remaining 2D Hadamard aliasing coefficient for each excitation after removing the 2D Hadamard aliasing coefficient for the acquired aliased images. Across the N_α excitations, the Eq. 16 can be expressed as:

$$C'_A = \left[(C_A)'_1, \ldots, (C_A)'_{N_\alpha} \right]. \tag{17}$$

2.4. The Likelihood, Prior, and Joint Distribution

As discussed in Section 1.1, the acquired aliased voxel values across the whole brain image are independent and identically distributed and the measurement error for each acquired aliased voxel is specified to be Gaussian distributed. Thus, the likelihood distribution (Eq. 3) of the acquired aliased voxel is:

$$P(a \mid X_A, \beta, \sigma^2) \propto (\sigma^2)^{-\frac{2N_c N_\alpha}{2}} \exp\left[-\frac{1}{2\sigma^2}(a - X_A\beta)'(a - X_A\beta)\right]. \quad (18)$$

Following the methodology of the Bayesian approach, the voxel value from calibration images can be utilized as prior information. Moreover, in Section 1.1 the voxel value, β, is specified to have a normal prior distribution. Therefore, the prior distribution of the voxel value $\beta \sim N(\mu, \sigma^2(C_A'C_A)^{-1})$:

$$P(\beta \mid C_A, \mu, \sigma^2) \propto (\sigma^2)^{-\frac{2N_s N_r}{2}} \exp\left[-\frac{1}{2\sigma^2}(\beta - \mu)'(C_A'C_A)(\beta - \mu)\right]. \quad (19)$$

Moreover, in Section 1.1, the variance of the measurement error, σ^2 is specified to have an inverse gamma prior distribution:

$$P(\sigma^2 \mid \lambda, \delta) \propto (\sigma^2)^{-(\lambda+1)} \exp\left[-\frac{\delta}{\sigma^2}\right], \quad (20)$$

where hyperparameters μ, λ and δ are assessed from the calibration images. The posterior distribution of the voxel value, β, and the variance of the measurement error, σ^2, follows the joint distribution as Eq. 6:

$$P(\beta, \sigma^2 \mid \cdot) \propto P(a \mid X_A, \beta, \sigma^2)P(\beta \mid C_A, \mu, \sigma^2)P(\sigma^2 \mid \lambda, \delta). \quad (21)$$

2.5. Hyperparameters Assessment

Before applying the image acquisition process of this proposed novel SMS model, a time series of calibration images will be collected first. The calibration image time series will be acquired through the traditional fMRI technique, and unlike the novel SMS model incorporating with different image shift techniques and 2D Hadamard aliasing coefficient. The calibration image time series is acquired without any image shift techniques or aliasing coefficient, no task experiment will be executed during this time series. As discussed in Section 2.4, the calibration images can be utilized as prior

information, hence the unknown hyperparameters can be assessed from calibration time series. In Eq. 21, the acquired aliasing matrix X_A and the artificial aliasing matrix C_A are known prior information that we do not need to assess from the calibration image time series. The hyperparameters μ, λ, and δ, on the other hand, need to be assessed from the calibration image time series. As discussed in Section 2.3, the hyperparameter μ is the averaged voxel value after the bootstrap resampling process. For each excitation in the time series, N_s brain images will be randomly chosen from the fully sampled calibration images and averaged to assess the voxel hyperparameter value $\mu = \bar{\nu}$. The shape parameter λ and the scale parameter δ from inverse gamma distribution in Eq. 20, also need to be assessed from the calibration image time series. After the bootstrap resampling process, the sample noise variance σ_0^2 can be estimated from the calibration image time series. Thus, the shape parameter can be assessed by $\lambda = n_0$, and the scale parameter can be assessed by $\delta = (n_0 - 1)\sigma_0^2$, where n_0 is the number of calibration images and σ_0^2 is sample noise variance.

2.6. The Posterior Estimation

According to the discussion in Section 1.1, Section 2.4, and Section 2.5, the joint distribution (Eq. 21) of the likelihood distribution of acquired aliased (Eq. 18), the prior distribution of the voxel value β (Eq. 19), and the prior distribution of the noise variance σ^2 (Eq. 20) can be calculated after algebra:

$$P(\beta, \sigma^2 \mid \cdot)$$
$$\propto (\sigma^2)^{-\frac{p}{2}} \exp\left[-\frac{1}{2\sigma^2}((\beta - \hat{\beta}_{MPM})'(X_A'X_A + C_A'C_A)(\beta - \hat{\beta}_{MPM}) + w) \right],$$
$$(22)$$

where $p = 2N_c N_\alpha + 2N_s N_r - 2\lambda - 2$, and $w = a'a + \mu'C_A'C_A\mu - (X_A'a + C_A'C_A\mu)'(X_A'X_A + C_A'C_A)^{-1}(X_A'a + C_A'C_A\mu) + 2\delta$. Moreover, as discussed in Section 1.1, the posterior distribution of the voxel value, β, and the noise variance, σ^2 can be integrated through the MPM technique. Therefore, the marginal posterior distribution of estimate voxel value β after integration is a student-t distribution $\beta \sim t(\nu^\star)$:

$$f(\beta \mid \cdot) \propto \left\{ 1 + \frac{1}{\nu^\star}(\beta - \hat{\beta}_{MPM})' \left[\frac{(X_A'X_A + C_A'C_A)}{\tau^2} \right] (\beta - \hat{\beta}_{MPM}) \right\}^{\frac{\nu^\star+1}{2}},$$
$$(23)$$

with $\nu^\star = p - 1$ and $\tau^2 = w/\nu^\star$. The marginal posterior mean (MPM) for $\hat{\beta}$ after integration is:

$$E(\beta \mid \cdot) = \hat{\beta}_{MPM} = (X'_A X_A + C'_A C_A)^{-1}(X'_A a + C'_A C_A \mu). \qquad (24)$$

In Eq. 24, the matrix $C'_A C_A$ acts as a regularizer for the matrix inverse to improve the condition of the equation. Since the true voxel value from calibration images is close to the true voxel value from acquired aliased images, Eq. 24 leads to $E(\beta \mid \cdot) = \beta$. The marginal posterior covariance of the voxel value $\hat{\beta}$ is:

$$cov(\beta \mid \cdot) = \frac{\nu^\star}{\nu^\star - 2}\tau^2(X'_A X_A + C'_A C_A)^{-1}, \qquad (25)$$

the separated voxel values are uncorrelated, meaning that there will not be signal leakage or correlation induced between slices.

Moreover, the marginal posterior distribution of σ^2 after integration is an inverse gamma distribution, $\sigma^2 \sim IG(\gamma, w/2)$:

$$f(\sigma^2 \mid \cdot) \propto (\sigma^2)^{-\frac{p}{2}-1} \exp\left[-w/(2\sigma^2)\right], \qquad (26)$$

with $\gamma = (p-1)/2$. The MPM of the noise variance σ^2 is:

$$E(\sigma^2 \mid \cdot) = \frac{w/2}{\gamma}, \qquad (27)$$

and the marginal posterior variance of the noise variance is:

$$var(\sigma^2 \mid \cdot) = \frac{w/2}{(\gamma - 1)^2(\gamma - 2)}. \qquad (28)$$

3. FMRI Data

3.1. Simulated FMRI Data

The proposed novel image shifted SMS technique was first applied to simulated fMRI data. The reconstructed brain images were compared through the mSPECS-IPA model (non image shift technique), the mSPECS-IPA-CAIPIRINHA model (image vertically shift), the mSPECS-IPA-VAT model (image horizontally shift) and the mSPECS-IPA-VAT model (image vertically and horizontally shift). Our goal is to improve the efficiency of the image acquisition process while simultaneously determining which image shift direction provides the best reconstruction results.
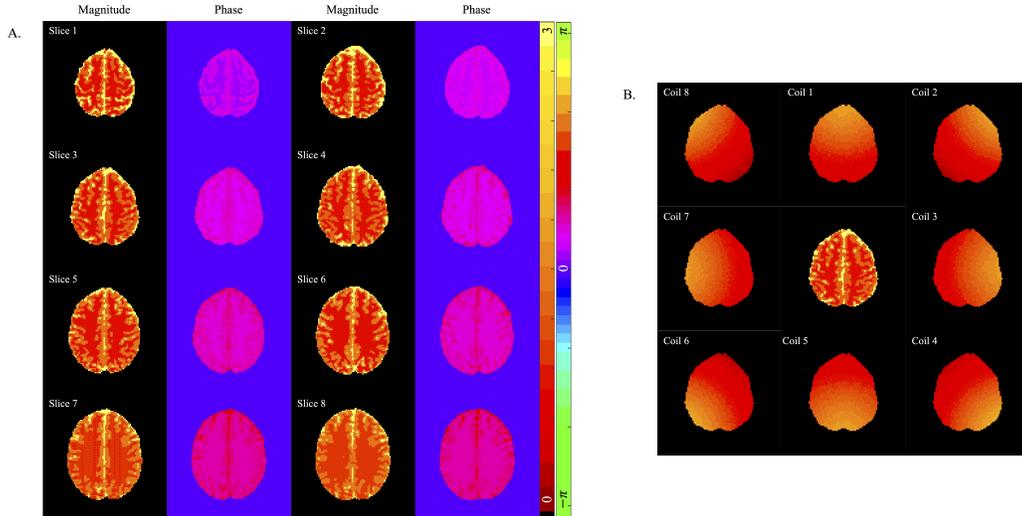
Figure 9: A. The magnitude and phase for the true noiseless simulated axial brain images with $N_s = 8$. B. The magnitude of the simulated sensitivity coils for slice 3 with $N_c = 8$.

The simulated fMRI time series mimicks our right hand finger tapping experimental data with the total number of TR (repetition time) = 510. According to the methodology of the image shifted SMS technique, two separate fMRI time series are simulated: the acquired fMRI time series and the calibration fMRI time series. The acquired fMRI time series was simulated using the mSPECS-IPA, mSPECS-IPA-CAIPIRINHA, mSPECS-IPA-VAT, and mSPECS-IPA-CAIPIVAT models, as different image shift directions were applied. The calibration fMRI time series, however, was simulated without any image shift technique or acceleration techniques. The calibration images were reconstructed by applying SENSE model. Since the simulated fMRI time series mimics an *in vivo* experiment, the first 20 repetition times are omitted to achieve a steady magnetic field, leaving a total number of $TR = 490$. In the simulated fMRI time series, total $N_s = 8$ axial brain images were included in the acquired simulated fMRI time series and the calibration simulated fMRI time series. In the calibration simulated time series, no simulated task block were added to the brain images. On the other hand, the simulated task blocks were added to the left motor cortex of the top 4 brain images. The simulated task blocks were added according to the real-world right hand finger tapping experiment with 15 TRs off and 15 TRs on for 16 epochs, and the first 20 TRs and last 10 TRs off. The contrast-

to-noise ratio and the signal-to-noise ratio we choose also mimick our fMRI experiment with $SNR = 50$ and $CNR = 0.5$. Thus, the mean magnitude added to each simulated slice is 4 and the mean magnitude added to the simulated task blocks is 0.04. The region-of-interest (ROI) was defined based on the reconstructed calibration images used in the experimental dataset. Specifically, voxels showing strong signal intensity in the reconstructed calibration images within the expected motor cortex region were selected as the reference location. The same spatial region was then used to define the ROI in the simulated datasets in order to maintain consistency between the simulated and experimental analyses. This ROI definition therefore reflects both anatomical location (motor cortex) and functional relevance for the finger-tapping task. Moreover, Gaussian distributed noise $N(0, 0.0064)$ was added to each slice of the simulated acquired fMRI time series and the simulated calibration fMRI time series. To mimic phade differences between slices, different phase angles from 5° to 40° with 5° intervals were added to each slice. Different phase angles were also added to different brain tissue types with 7.5° for white matter (WM), 15° for gray matter (GM), and 22.5° for cerebral spinal fluid (CSF).

In order to investigate the performance of different models with different acceleration factors, the IPA factor we used in the simulated acquired fMRI dataset is $R = 2$, and different TPA factors were incorporated in the experiment with $TPA = 2$, $TPA = 4$, and $TPA = 8$. Thus, the net acceleration factor is the product of the IPA factor and the TPA factor with $NET = 4$, $NET = 8$, and $NET = 16$. For the $TPA = 2$ scenario, the slice aliasing scenario is: packet 1: slice 1 and slice 5, packet 2: slice 2 and slice 6, packet 3: slice 3 and slice 7, packet 4: slice 4 and slice 8. For $TPA = 4$ scenario, the slices aliasing scenario is: packet 1: even slices, packet 2: odd slices. For $TPA = 8$ scenario, all slices are aliased in one packet.

Fig. 9A shows the true noiseless magnitude and phase for each slice of simulated axial brain images with $N_s = 8$. A total number of $N_c = 8$ channel sensitivity coils were simulated and applied according to the real right hand finger tapping experiment. Fig. 9B shows the magnitude and position for each coil corresponding to slice 3. The mean magnitude for each simulated coil is 0.95, and to increase the difference between each coil, different phase angles were added to the simulated coils from 0° to 17.5° with 2.5° intervals.

The simulated SMS data used in this study were generated through artificial aliasing of fully sampled k-space data. While this approach allows controlled investigation of image shift direction, Hadamard encoding, and

Bayesian regularization effects, it does not reproduce all characteristics of experimental SMS acquisitions, such as slice dependent phase errors, eddy current effects, and complex noise correlations. Therefore, the simulation results are intended to provide mechanistic insights into the reconstruction behavior rather than a definitive performance comparison against established SMS reconstruction methods such as Slice-GRAPPA or Split Slice-GRAPPA, which have been extensively validated using in vivo multiband acquisitions (Cauley et al. [4]; Setsompop et al. [22]).

3.2. Experimental FMRI Data

A right-handed finger tapping fMRI experiment for a single object was executed through a 3.0 T General Electric Signa LX MRI scanner. The flip angel was 90° and the acquisition bandwidth is 125 kHz in this experiment. The slice thickness for the axial brain images was 2.5 mm. A total of nine slices were scanned. In this experiment, an 8 channel receiver head coil was utilized with dimension 96×96 for a 24 cm full field-of-view, with the phase encoding direction from posterior to anterior. It should be noted that the 8 channel receiver coil used in this experiment provides limited spatial sensitivity variation for high through-plane acceleration factors. In current SMS fMRI practice, 32 channel or higher receiver arrays are typically employed to support robust slice separation. Consequently, the present dataset is not intended to demonstrate optimal SMS image quality, but rather to evaluate relative reconstruction behavior under constrained coil geometry. In our right-handed finger tapping fMRI experiment, two fMRI time series were acquired: a non-task calibration time series and a task time series. The right-handed finger tapping experiment was designed with an initial 20 TRs off rest, followed by 15 TRs off and 15 TRs on for 16 epochs, and the final 10 TRs of rest, resulting in a total 510 TRs for the task time series. The same echo time (TE) was applied to both fMRI time series, consisting of three segments. The calibration dataset was acquired with the same number of time points as the fMRI task acquisition to ensure stable parameter estimation and consistent comparisons across reconstruction models. Consequently, the calibration acquisition time is approximately equal to the task acquisition time in this experimental setup. The TE for the first 10 TRs and the last 490 TRs was 42.7 ms. From the 11th to the 20th time point, the TE values were 42.7 ms, 45.2 ms, 47.7 ms, 50.2 ms, and 52.7 ms, and this sequence was repeated twice. The first 20 TRs of the task time series were disregarded to
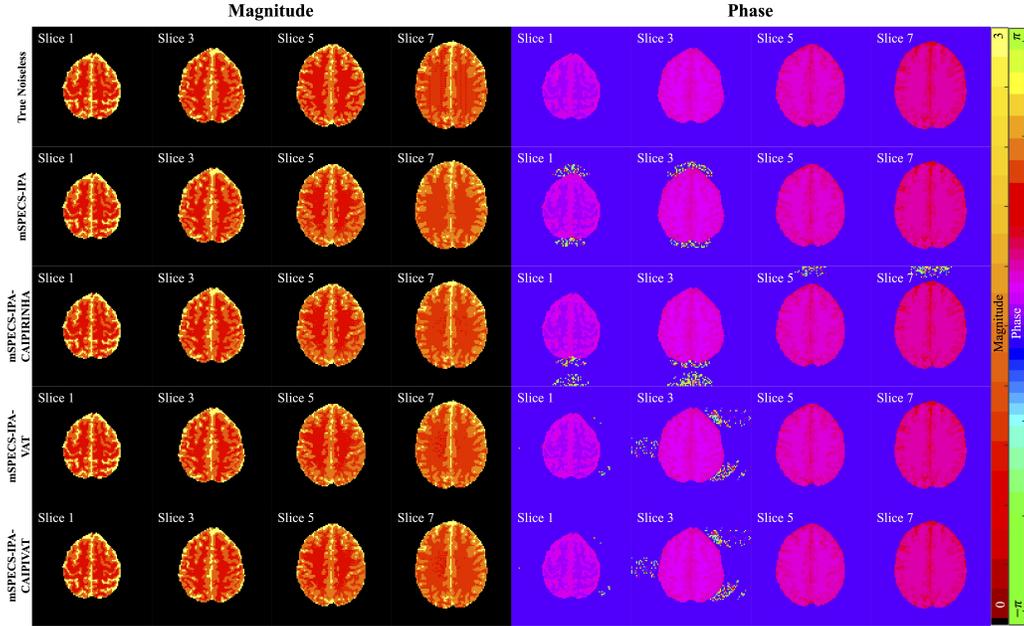
Figure 10: The magnitude and phase of the reconstructed images odd slices from mSPECS-IPA, mSPECS-IPA-CAIPIRINHA, mSPECS-IPA-VAT, and mSPECS-IPA-CAIPIVAT, compared with the magnitude and phase from true noiseless simulated images odd slices with TPA=2.

achieve a steady magnetic field of the scanner, resulting in last 490 TRs of the task time series were applied to the novel proposed model.

In our right-handed finger-tapping fMRI experiment, aliased task images were not acquired experimentally, as this is a methodological study and so we can evaluate various acceleration factors with the same data. Since the dimension of the 2D Hadamard aliasing coefficient must be a power of two, only eight slices were used in the proposed image-shifted SMS techniques, with the most interior axial brain slice disregarded. Instead, the task images were artificially aliased from the fully acquired task time series, following a procedure similar to that used for generating simulated aliased task images. The artificially aliased task images for each model were primarily generated using different image shift techniques and 2D Hadamard encoding coefficients. The artificially aliased subsampled k-space data were obtained by skipping every other line in the fully sampled k-space of the summed images after applying the Fourier transform. The aliased task images were then reconstructed from the subsampled k-space using the inverse Fourier transform.

26

The last $N_{cal} = 40$ fully sampled non-task calibration images were used to assess the hyperparameter. The same acceleration factors from the simulated fMRI time series were applied in the real-world right-handed finger tapping experiment with $R = 2$, and $TPA = 2, 4, 8$. The same net acceleration factors were achieved in the real-world experimental time series. The mSPECS-IPA model, mSPECS-IPA-CAIPIRINHA model, mSPECS-IPA-VAT model and the mSPECS-IPA-CAIPIVAT model were applied to the right-handed finger tapping experiment fMRI time series. The SENSE method was also applied to the calibration fMRI time series, and the reconstructed images were utilized as the reference images. The reconstructed results from the novel image shift SMS technique were compared with the reference images. All simulations and data analyses were implemented in MATLAB (MathWorks, Natick, MA, USA) using MATLAB R2022b. The numerical experiments were performed using built-in MATLAB functions together with standard toolboxes. A fixed random seed was used for the simulation procedures to ensure reproducibility.

4. The Simulation Results

4.1. Non-Task Simulated Reconstruction Results

Based on the methodology of the novel proposed image shift SMS techniques, we conducted the simulated experiment with the same in-plane acceleration factor, $IPA = 2$, and different through-plane acceleration factors with $TPA = 2$, $TPA = 4$, and $TPA = 8$. The reconstructed results were compared between mSPECS-IPA model (without image shift technique), mSPECS-IPA-CAIPIRINHA model (image shift along vertical direction), mSPECS-IPA-VAT model (image shift along horizontal direction), and mSPECS-IPA-CAIPIVAT (image shift along vertical and horizontal direction). The reconstructed results were also compared with the true noiseless simulated images. Fig. 10 shows the mean magnitude and mean phase from odd slices of the reconstructed images from mSPECS-IPA, mSPECS-IPA-CAIPIRINHA, mSPECS-IPA-VAT, and mSPECS-IPA-CAIPIVAT, compared with the magnitude and phase from true noiseless simulated images, and the through-plane acceleration factor is 2. Fig. 10 is generated based on Eq. 24. Compared to the true magnitude, the mean magnitude from these four models is closely aligned with the true value. No inter-slice signal leakage or artifact distortions appear in the mean magnitude images. The mean

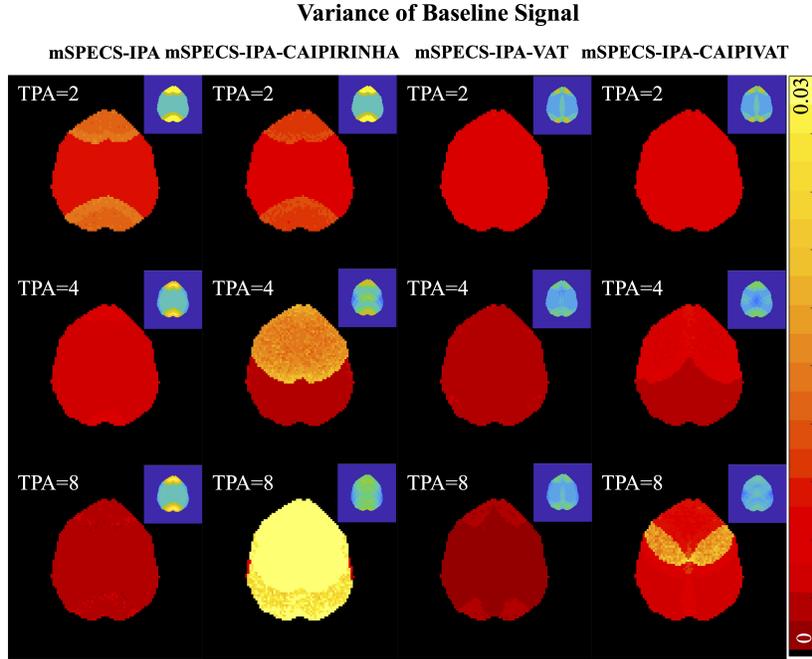27

Variance of Baseline Signal

Figure 11: The variance of the baseline regression coefficient of slice 3 from reconstructed images from mSPECS-IPA, mSPECS-IPA-CAIPIRINHA, mSPECS-IPA-VAT, and mSPECS-IPA-CAIPIVAT model with different through-plane acceleration factors. The top-right corner shows the overlapping indicator for each SMS reconstruction model under different TPA factors, illustrating the corresponding slice overlap and voxel aliasing patterns.

phase of the reconstructed images from these four models is also consistent with the phase value of the true noiseless simulated image inside the brain. ~~However, residuals are present outside the brain in the mSPECS-IPA, mSPECS-IPA-CAIPIRINHA, mSPECS-IPA-VAT, and mSPECS-IPA-CAIPIVAT models due to differences in the image shift techniques and slice overlapping conditions in each model.~~ Fig. 11 was generated according to Eq. 25. The top-right corner displays the overlapping indicator for each novel SMS image reconstruction model, incorporating different TPA factors. It represents the slice overlapping and voxel aliasing scenario for each approach and acceleration factor. When the acceleration factor is low, IPA = 2 and TPA = 2, all four models have a low variance at the center of the brain image. ~~However, due to a high overlapping indicator value at the anterior and posterior regions, high variance is detected at these region.~~ As the accelera-
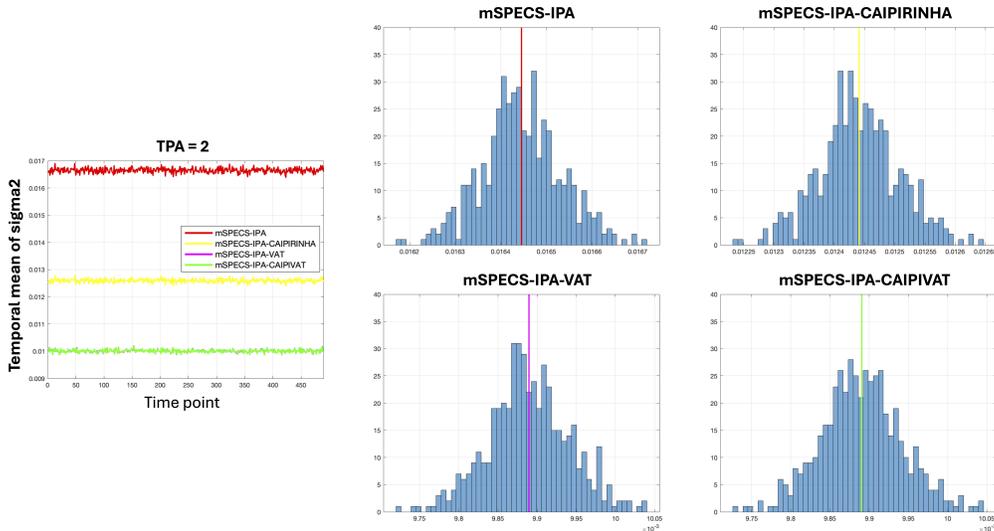
28

Figure 12: The temporal mean of residual variance of brain images reconstructed from the mSPECS-IPA (red), mSPECS-IPA-CAIPIRINHA (yellow), mSPECS-IPA-VAT (pink), and mSPECS-IPA-CAIPIVAT (green) models with IPA = 2 and TPA = 2. The curve corresponding to the mSPECS-IPA-VAT model (pink) closely overlaps with the curve for the mSPECS-IPA-CAIPIVAT model (green).

tion factor increases, models that do not incorporat the vertical image shift technique, mSPECS-IPA and mSPECS-IPA-VAT model, show a decrease in task regression coefficient variance. On the other hand, models that incorporate with the vertical image shift technique, mSPECS-IPA-CAIPIRINHA and mSPECS-IPA-CAIPIVAT model, exhibit an increase in task regression coefficient variance in the anterior region of the brain image. Among these four models, the mSPECS-IPA-CAIPIRINHA has the highest task regression coefficient variance when IPA = 2 and TPA = 8. The temporal variance of the task signal is shown in the Appendix A Fig. A.21.

Fig. 12 displays temporal mean of residual variance of brain images reconstructed from mSPECS-IPA, mSPECS-IPA-CAIPIRINHA, mSPECS-IPA-VAT and mSPECS-IPA-CAIPIVAT model with IPA = 2 and TPA = 2. Fig. 13 shows temporal mean of residual variance for brain images reconstructed from same models but with acceleration factors IPA = 2 and TPA = 4 and 8. Fig. 12 and Fig. 13 are generated based on Eq. 27. For each acceleration factor, among the four models, mSPECS-IPA has the highest temporal mean of residual variance, whereas the models incorporating
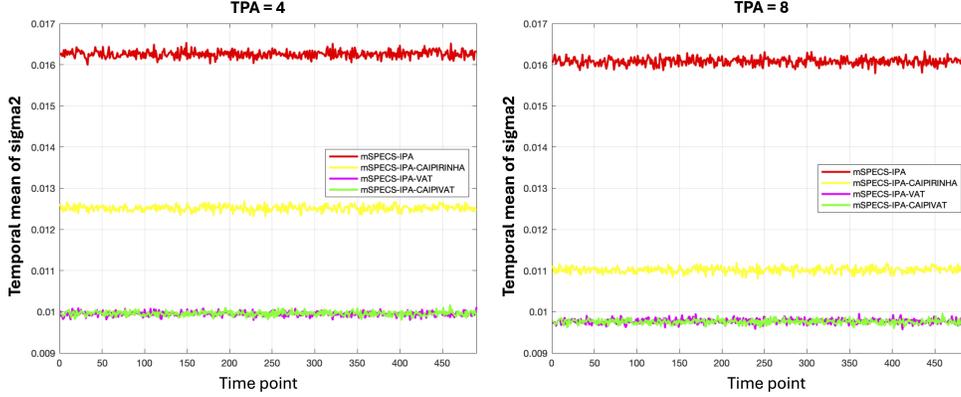
29

Figure 13: The temporal mean of residual variance of brain images reconstructed from mSPECS-IPA, mSPECS-IPA-CAIPIRINHA, mSPECS-IPA-VAT and mSPECS-IPA-CAIPIVAT model with IPA = 2 and TPA = 4 and 8.

the horizontal image shift technique, mSPECS-IPA-VAT and mSPECS-IPA-CAIPIVAT, exhibit the lowest temporal mean of residual variance. As the acceleration factor increases, the temporal mean of residual variance slightly decreases across all four models. We also investigated the temporal variance of the residual variance of brain images reconstructed from mSPECS-IPA, mSPECS-IPA-CAIPIRINHA, mSPECS-IPA-VAT and mSPECS-IPA-CAIPIVAT model with IPA = 2 and TPA = 2, 4, and 8, which is shown in Appendix A Fig. A.22 and Fig. A.23.

We also investigated the signal-to-noise ratio (SNR) and the geometric factor g-factor values across mSPECS-IPA, mSPECS-IPA-CAIPIRINHA, mSPECS-IPA-VAT, and mSPECS-IPA-CAIPIVAT models. The SNR can be calculated as $SNR = \beta_0/\sigma_N$, where β_0 represents the baseline signal for each location of the brain image, and σ_N represents the standard deviation of the noise. ~~The higher the SNR value is, the better performance of the model.~~ According to the g-factor definition(Eq. 1) in Section 2.1.1, the through-plane acceleration factor also needs to be incorporated into it. Thus, the g-factor can be calculated as $g_{accelerate} = \sqrt{N_s}SNR_{full}/SNR_{accelerate}\sqrt{R}$, where $R = 2$ indicating the in-plane acceleration factor. ~~The closer g-factor is to 1, the better reconstructed results the model will produce.~~ Fig. 14A shows the SNR value of slice 3 for four models with different through-plane acceleration factors. The top right corner is the slice overlapping scenario corresponding to average of the first N_α time point for each model. As the

30

TPA factor increases, the *SNR* value for the mSPECS-IPA and mSPECS-IPA-VAT models also increases. Moreover, in the mSPECS-IPA-VAT model, both the posterior and anterior regions of the brain exhibit higher *SNR* values compared to the mSPECS-IPA model. In contrast, for the mSPECS-IPA-CAIPIRINHA and mSPECS-IPA-CAIPIVAT models, the *SNR* value does not increase evenly across the entire brain image as the TPA factor increases. In the mSPECS-IPA-CAIPIRINHA model, at higher TPA factors, the *SNR* in the middle brain region is lower than at lower TPA factors. A similar pattern is observed in the left side of the brain image in the mSPECS-IPA-CAIPIVAT model. Fig. 14B shows the *g*-factor of slice 3 across different models with varying through-plane acceleration factors. As the TPA factor increases, the *g*-factor in the mSPECS-IPA-CAIPIRINHA and mSPECS-IPA-CAIPIVAT models increases dramatically, whereas in the mSPECS-IPA and mSPECS-IPA-VAT models, it increases only slightly. Comparing the *g*-factor values between the mSPECS-IPA and mSPECS-IPA-VAT models, the *g*-factor in the mSPECS-IPA-VAT model is closer to 1 in both the posterior and anterior regions of the brain. ~~The anterior artifacts observed at higher acceleration factors are consistent with insufficient coil sensitivity diversity rather than failure of the reconstruction framework itself.~~ These artifacts are expected under aggressive SMS acceleration when using low channel count receiver coils.

4.2. Task Simulated Reconstruction Results

In order to investigate the task activation detection performance of each model, we applied the novel image shift SMS techniques to the simulated right-handed finger tapping experiment with the same in-plane acceleration factor, IPA=2, and different through-plane acceleration factors TPA=2, TPA=4, and TPA=8. For each voxel in the brain image, the signal can be expressed as $y = \beta_0 + \beta_1 x + \epsilon$, where β_0 is the baseline signal of the voxel, β_1 is the task signal, x is a vector with elements 0 and 1 indicating each time point with or without task activation. Therefore, the contrast-to-noise ratio (*CNR*) can be calculated as $CNR = \beta_1/\sigma_N$, and same as the definition in *SNR*, σ_N stands for the standard deviation of the noise. The activation detection rate for each model was also investigated by applying a complex-valued model to compute fMRI activation (Rowe and Logan [18]). Fig. 15A shows the average and standard deviation of the *CNR* values in the region of interest (ROI) for odd slices from the mSPECS-IPA, mSPECS-IPA-CAIPIRINHA, mSPECS-IPA-VAT, and mSPECS-IPA-CAIPIVAT models with an acceler-
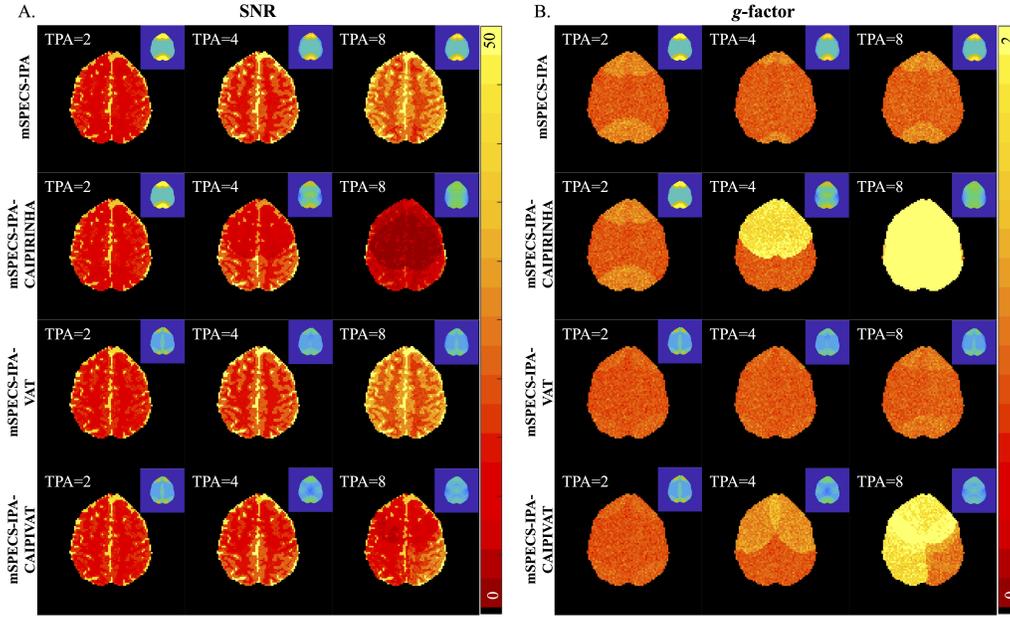
31

Figure 14: A. The *SNR* value of slice 3 from reconstructed images for mSPECS-IPA, mSPECS-IPA-CAIPIRINHA, mSPECS-IPA-VAT, and mSPECS-IPA-CAIPIVAT model with different TPA factor. B. The *g*-factor value of slice 3 from reconstucted images for mSPECS-IPA, mSPECS-IPA-CAIPIRINHA, mSPECS-IPA-VAT, and mSPECS-IPA-CAIPIVAT model with different TPA factor. The top-right corner shows the overlapping indicator for each SMS reconstruction model under different TPA factors, illustrating the corresponding slice overlap and voxel aliasing patterns.

ation factor of TPA = 2. The *CNR* value of the ROI for slice 1 in the mSPECS-IPA-VAT and mSPECS-IPA-CAIPIVAT models is slightly higher than in the mSPECS-IPA and mSPECS-IPA-CAIPIRINHA models. Meanwhile, the *CNR* value of the ROI for slice 3 is similar across all four models. Fig. 15B shows the average task activation detection rate in the ROI for odd slices from the mSPECS-IPA, mSPECS-IPA-CAIPIRINHA, mSPECS-IPA-VAT, and mSPECS-IPA-CAIPIVAT models with TPA = 2. Compared to the models with a horizontal image shift, mSPECS-IPA-VAT and mSPECS-IPA-CAIPIVAT, the models without horizontal image shift, mSPECS-IPA and mSPECS-IPA-CAIPIRINHA, exhibit a lower average z-score in the ROI. ~~This indicates that the activation detection ability of mSPECS-IPA and mSPECS-IPA-CAIPIRINHA is lower than that of the mSPECS-IPA-VAT and mSPECS-IPA-CAIPIVAT models.~~
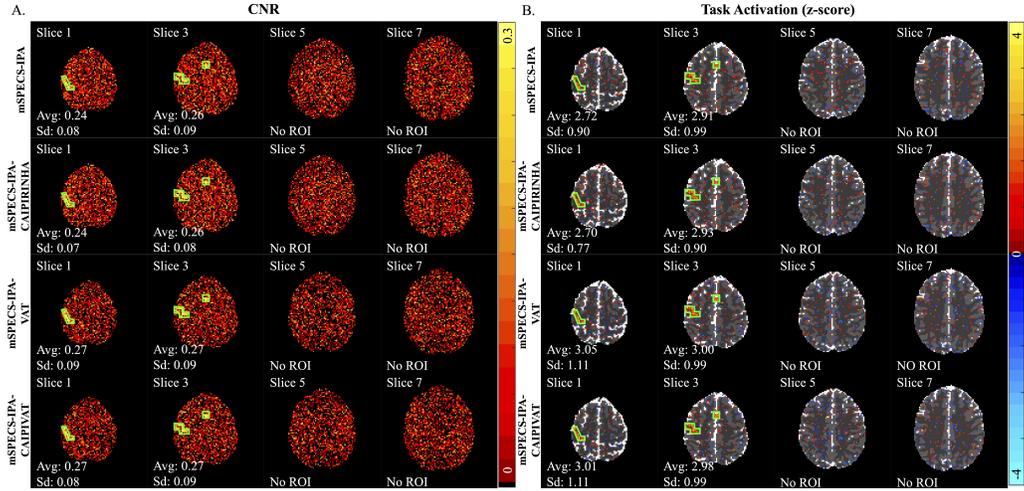
Figure 15: A. The average *CNR* value of ROI for odd slices with acceleration factor TPA=2 from mSPECS-IPA, mSPECS-IPA-CAIPIRINHA, mSPECS-IPA-VAT, and mSPECS-IPA-CAIPIVAT model. B. The average task activation rate (z-score) of ROI for odd slices with acceleration factor TPA=2 from mSPECS-IPA, mSPECS-IPA-CAIPIRINHA, mSPECS-IPA-VAT, and mSPECS-IPA-CAIPIVAT model.

To assess the influence of a high acceleration factor on the task activation detection ability of each model, we compared the *CNR* value and the task activation detection rate of ROI for mSPECS-IPA, mSPECS-IPA-CAIPIRINHA, mSPECS-IPA-VAT, and mSPECS-IPA-CAIPIVAT models under different acceleration factors, TPA = 2, TPA = 4, and TPA = 8. Fig. 16A shows the average *CNR* value in the ROI of slice 3 for the mSPECS-IPA, mSPECS-IPA-CAIPIRINHA, mSPECS-IPA-VAT, and mSPECS-IPA-CAIPIVAT models with different acceleration factors. As the acceleration factor increases, the average *CNR* value decreases across all four models. However, at high acceleration factors, the average *CNR* value in the ROI is higher in the mSPECS-IPA and mSPECS-IPA-VAT models compared to the models incorporating vertical image shift, mSPECS-IPA-CAIPIRINHA and mSPECS-IPA-CAIPIVAT. Among these models, the model applies image shift only along the vertical direction, mSPECS-IPA-CAIPIRINHA exhibits the lowest average *CNR* value in the ROI. Fig. 16B shows the activation detection rate (z-score) in the ROI of slice 3 for the mSPECS-IPA, mSPECS-IPA-CAIPIRINHA, mSPECS-IPA-VAT, and mSPECS-IPA-CAIPIVAT models with different acceleration factors. As the acceleration
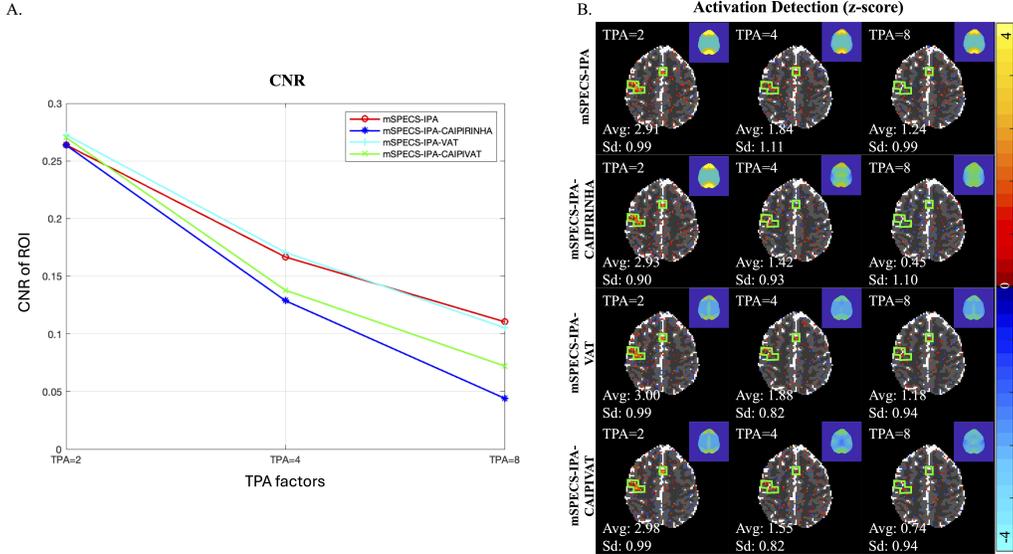
33

Figure 16: A. The average *CNR* value of ROI for slice 3 from mSPECS-IPA, mSPECS-IPA-CAIPIRINHA, mSPECS-IPA-VAT, and mSPECS-IPA-CAIPIVAT model with acceleration factor TPA=2, TPA=4, and TPA=8. B. The average activation detection rate (z-score) of ROI for slice 3 from mSPECS-IPA, mSPECS-IPA-CAIPIRINHA, mSPECS-IPA-VAT, and mSPECS-IPA-CAIPIVAT model with acceleration factor TPA=2, TPA=4, and TPA=8. The top-right corner shows the overlapping indicator for each SMS reconstruction model under different TPA factors, illustrating the corresponding slice overlap and voxel aliasing patterns.

factor increases, it becomes more difficult to capture the entire simulated activation blocks across all four models. However, at TPA = 8, the models without vertical image shift, mSPECS-IPA and mSPECS-IPA-VAT, exhibit higher average z-scores in the ROI compared to the models with vertical image shift, mSPECS-IPA-CAIPIRINHA and mSPECS-IPA-CAIPIVAT. Although the models incorporating vertical image shift exhibit lower average z-scores in the ROI, the mSPECS-IPA-CAIPIVAT model achieves a higher average z-score compared to the mSPECS-IPA-CAIPIRINHA model. Among all models, mSPECS-IPA-CAIPIRINHA provides the lowest activation detection rate, indicating that it has the least ability to capture the simulated task activation blocks. Although the proposed method exhibits higher mean *CNR* and activation detection rates across several configurations, the associated variability indicates that these improvements are not uniformly statistically significant. These findings suggest potential benefits that depend on
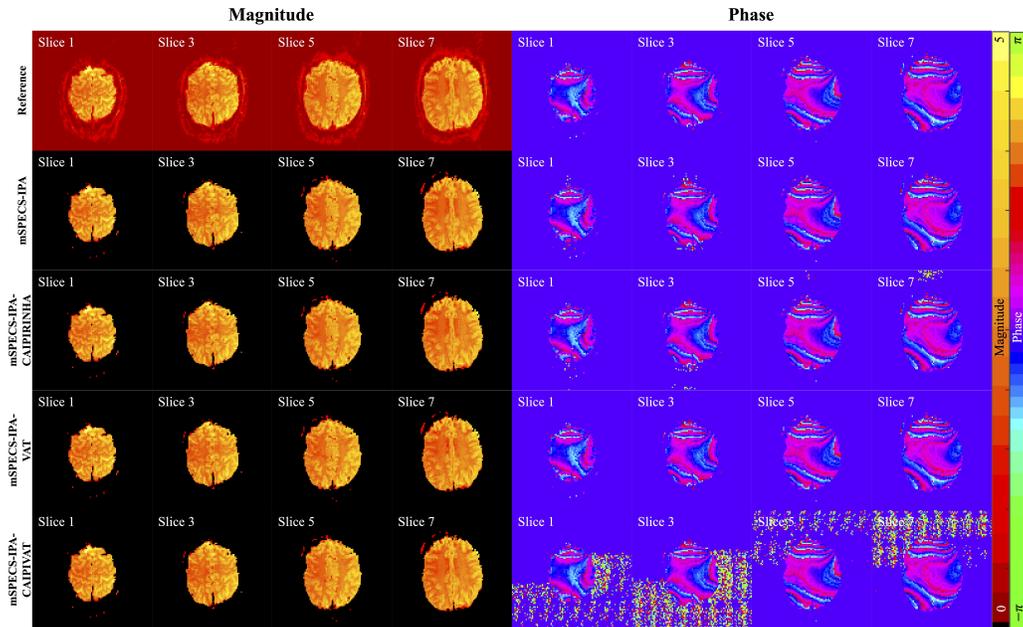
34

Figure 17: The mean magnitude and mean phase of the odd slices from reconstructed image with through-plane acceleration factor TPA=2 corresponding to mSPECS-IPA, mSPECS-IPA-CAIPIRINHA, mSPECS-IPA-VAT and mSPECS-IPA-CAIPIVAT model.

~~acquisition parameters, encoding strategy, and brain region, rather than a guaranteed performance improvement in all settings.~~ The detailed quantitative values of the activation detection (z-score) and *CNR* for the simulation and experimental analyses are summarized in Tables A.1 in the Supplementary Materials.

5. The Experimental Results

5.1. Non-Task Experimental Reconstruction Results

To investigate the performance of the proposed novel image-shifted SMS techniques in a real-world fMRI experiment, we applied four models to an in vivo right-handed finger-tapping fMRI time series. The reconstruction results from these models were compared with reference axial brain images, reconstructed using the SENSE technique from the calibration axial brain image time series. Additionally, we applied the novel image-shifted SMS techniques with the same in-plane acceleration factor, IPA = 2, and varying through-plane acceleration factors, TPA = 2, TPA = 4, and TPA =

8, to examine the impact of acceleration on each model. Fig. 17 shows the mean magnitude and mean phase of the odd slices reconstructed with TPA = 2 from the mSPECS-IPA, mSPECS-IPA-CAIPIRINHA, mSPECS-IPA-VAT, and mSPECS-IPA-CAIPIVAT models, compared to the mean magnitude and mean phase of the reference image from the calibration images. Compared to the mean magnitude of the reference image, the mean magnitude from the four image-shifted SMS models is closely aligned with the reference image. No inter-slice signal leakage or artifactual brain distortions from other slices were observed in the reconstructed images. Compared to the mean phase of the reference image, the mean phase of the reconstructed images from the mSPECS-IPA, mSPECS-IPA-CAIPIRINHA, mSPECS-IPA-VAT, and mSPECS-IPA-CAIPIVAT models exhibits a highly similar pattern inside the brain. However, residual artifacts (which could be measured) appear outside the brain, particularly in the mSPECS-IPA-CAIPIRINHA and mSPECS-IPA-CAIPIVAT models, which can be attributed to voxel aliasing, slice overlapping, and image shift techniques applied in different models. The temporal variance of the task signal is shown in Appendix B Fig. A.24.

Similar to the simulation-based reconstructed axial brain image analysis, we also investigate the signal-to-noise ratio (SNR) and the geometric factor (g-factor) in the reconstructed brain images from the mSPECS-IPA, mSPECS-IPA-CAIPIRINHA, mSPECS-IPA-VAT, and mSPECS-IPA-CAIPIVAT models under different acceleration factors. The SNR value and the g-factor are calculated as described in Section 4.1. Fig. 18A shows the average SNR value for slice 3 in the mSPECS-IPA, mSPECS-IPA-CAIPIRINHA, mSPECS-IPA-VAT, and mSPECS-IPA-CAIPIVAT models with acceleration factors TPA = 2, TPA = 4, and TPA = 8. As the acceleration factor increases, the average SNR in the mSPECS-IPA and mSPECS-IPA-VAT models also increases. The mSPECS-IPA-VAT model exhibits a higher average SNR at the edges of the brain image compared to the mSPECS-IPA model. Conversely, in the models incorporating vertical image shift (mSPECS-IPA-CAIPIRINHA and mSPECS-IPA-CAIPIVAT), the average SNR initially increases as the acceleration factor increases from TPA = 2 to TPA = 4 but decreases at TPA = 8. Comparing the average SNR of the reconstructed axial brain images across the four models, the mSPECS-IPA-VAT model provides the highest SNR value. Fig. 18B shows the g-factor of the reconstructed image of slice 3 for the mSPECS-IPA, mSPECS-IPA-CAIPIRINHA, mSPECS-IPA-VAT, and mSPECS-IPA-CAIPIVAT models under different acceleration factors. Although the g-factor increases across all four models
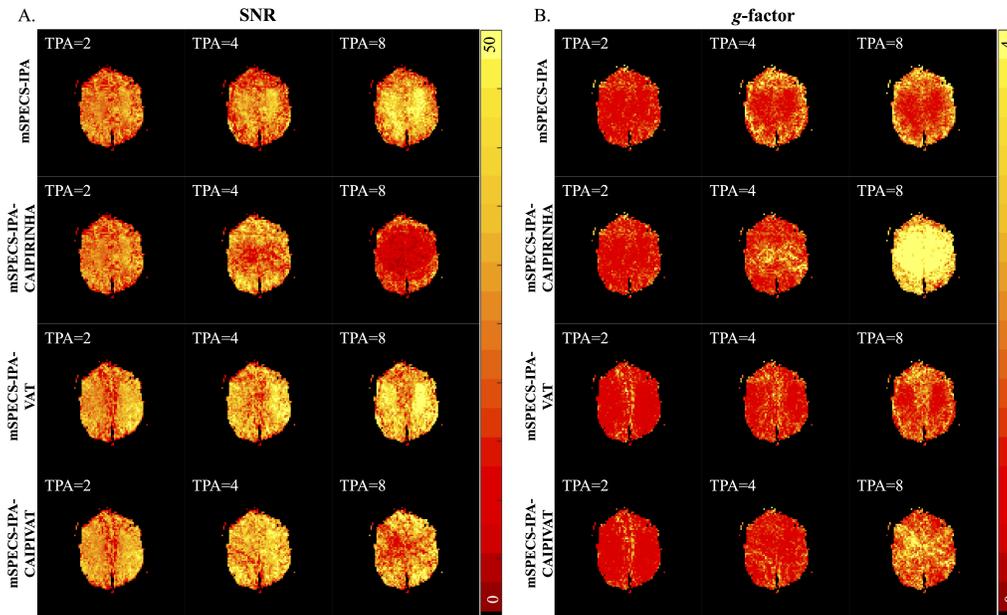
36

Figure 18: A. The *SNR* value of reconstructed brain images slice 3 from mSPECS-IPA, mSPECS-IPA-CAIPIRINHA, mSPECS-IPA-VAT and mSPECS-IPA-CAIPIVAT model with different acceleration factors. B. The *g*-factor value of reconstructed brain images slice 3 from mSPECS-IPA, mSPECS-IPA-CAIPIRINHA, mSPECS-IPA-VAT and mSPECS-IPA-CAIPIVAT model with different acceleration factors.

as the acceleration factor increases, the mSPECS-IPA-VAT model exhibits the lowest *g*-factor compared to the other three models. In contrast, the mSPECS-IPA-CAIPIRINHA model has the highest *g*-factor among the four models at TPA = 8.

5.2. Task Experimental Reconstruction Results

To analyze the activation detection ability of the proposed image-shifted SMS technique in a real-world right-handed finger-tapping fMRI experiment, we also investigate the contrast-to-noise ratio (*CNR*) and the activation detection rate (z-score) of ROI of the reconstructed axial brain images from the mSPECS-IPA, mSPECS-IPA-CAIPIRINHA, mSPECS-IPA-VAT, and mSPECS-IPA-CAIPIVAT models under different acceleration factors. Since a right-handed finger-tapping fMRI experiment was conducted, the task activation area was expected to be in the left motor cortex of the brain. Fig. 19A shows the average *CNR* value in the ROI for odd slices of the
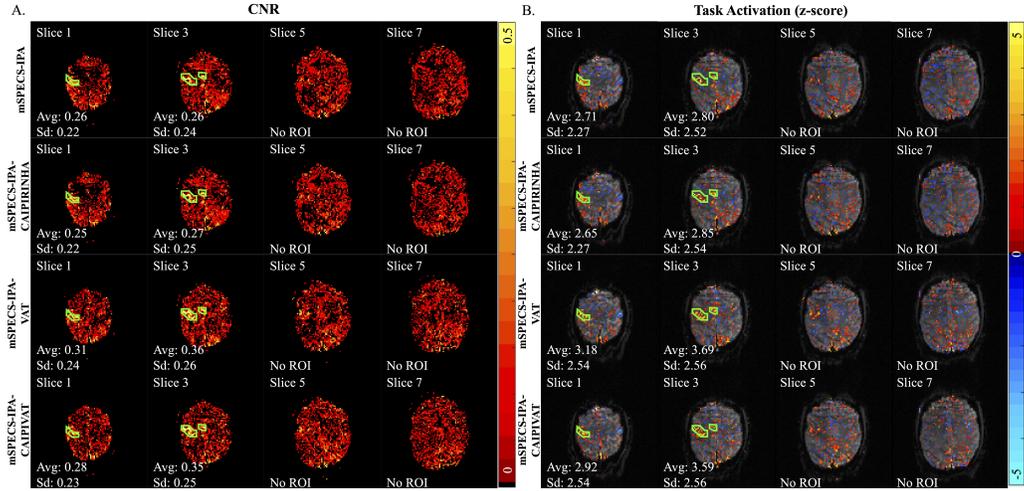
Figure 19: A. The average *CNR* value of ROI for odd slices of reconstructed images from mSPECS-IPA, mSPECS-IPA-CAIPIRINHA, mSPECS-IPA-VAT and mSPECS-IPA-CAIPIVAT model with TPA=2. B. The task activation detection (z-score) map of ROI for odd slices of reconstructed images from mSPECS-IPA, mSPECS-IPA-CAIPIRINHA, mSPECS-IPA-VAT and mSPECS-IPA-CAIPIVAT model with TPA=2.

reconstructed images from the mSPECS-IPA, mSPECS-IPA-CAIPIRINHA, mSPECS-IPA-VAT, and mSPECS-IPA-CAIPIVAT models with an acceleration factor of TPA = 2. Compared to models without horizontal image shift, mSPECS-IPA and mSPECS-IPA-CAIPIRINHA, models incorporating horizontal image shift, mSPECS-IPA-VAT and mSPECS-IPA-CAIPIVAT, exhibit a higher average *CNR* value in the ROI, with mSPECS-IPA-VAT achieving the highest *CNR* value among the four models. Fig. 19B shows the task activation detection rate for odd slices of the reconstructed images from the mSPECS-IPA, mSPECS-IPA-CAIPIRINHA, mSPECS-IPA-VAT, and mSPECS-IPA-CAIPIVAT models with TPA = 2. Similar to the conclusion drawn from the average *CNR* in the ROI, the mSPECS-IPA-VAT and mSPECS-IPA-CAIPIVAT models exhibit a higher average z-score in the ROI of the left motor cortex compared to the mSPECS-IPA and mSPECS-IPA-CAIPIRINHA models. Among these four models, the mSPECS-IPA-VAT model provides the best activation detection map at TPA = 2, ~~indicating that mSPECS-IPA-VAT is the most sensitive model for detecting task activation blocks.~~

The average *CNR* value in the ROI and the task activation detection

38

rate were also analyzed for the mSPECS-IPA, mSPECS-IPA-CAIPIRINHA, mSPECS-IPA-VAT, and mSPECS-IPA-CAIPIVAT models under different acceleration factors. Fig. 20A shows the average CNR value in the ROI of slice 3 for the four models, compared at different acceleration factors, TPA = 2, TPA = 4, and TPA = 8. As the acceleration factor increases, the average CNR decreases significantly across all four models. However, among them, the mSPECS-IPA-VAT model provides the highest average CNR in the ROI, while the mSPECS-IPA-CAIPIRINHA model exhibits the lowest average CNR. Moreover, models incorporating horizontal image shift exhibit a higher average CNR in the ROI compared to models without horizontal image shift. Fig. 20B shows the average task activation detection map for the ROI of slice 3 across the four models with different acceleration factors. As the acceleration factor increases, the average z-score in the ROI decreases significantly for each model. Among these four models, the mSPECS-IPA-VAT model provides the highest average z-score in the ROI, while the mSPECS-IPA-CAIPIRINHA model exhibits the lowest. Additionally, models incorporating vertical image shift exhibit a lower average z-score compared to models without vertical image shift. ~~The mSPECS-IPA-VAT model demonstrates the strongest ability to detect task activation blocks in brain images.~~ A detailed quantitative values of the activation detection (z-score) and CNR for the simulation and experimental analyses are summarized in Tables B.2 in the Supplementary Materials.

6. Discussion

The primary objective of this study was to evaluate the proposed complex-valued Bayesian reconstruction framework under different acceleration and image-shift conditions, rather than merely to compare image-shift strategies. The simulation and experimental results together show that reconstruction performance depends strongly on both acceleration factor and image-shift direction, particularly when activation detection is used as the performance criterion.

With increasing through-plane acceleration, the reconstructed images generally exhibited a trade-off between acquisition efficiency and activation sensitivity. Although SNR increased in some models, particularly mSPECS-IPA and mSPECS-IPA-VAT, both CNR and activation-related z-scores decreased as the acceleration factor increased. This pattern indicates that higher acceleration does not necessarily improve the practical detectability of task-
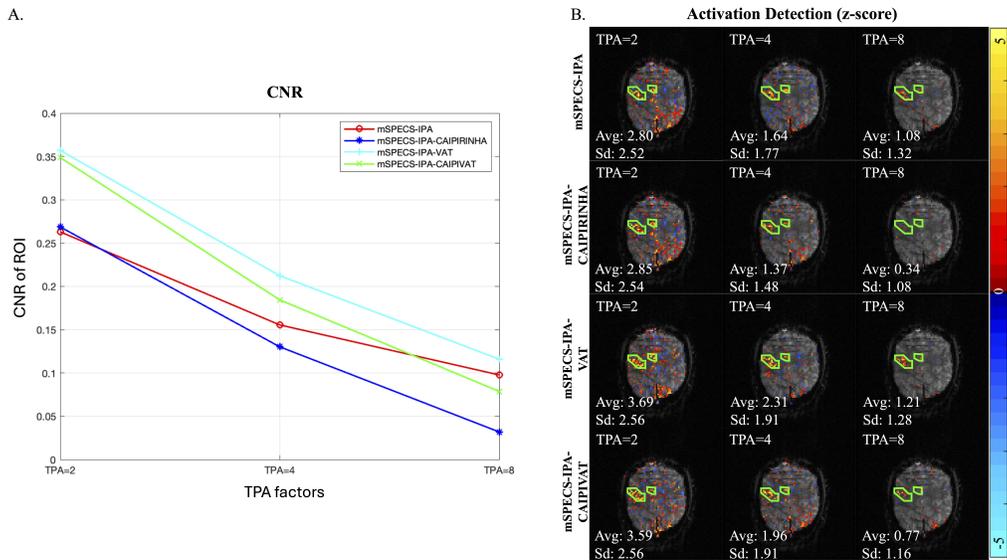
Figure 20: A. The average *CNR* value of ROI for slice 3 from mSPECS-IPA, mSPECS-IPA-CAIPIRINHA, mSPECS-IPA-VAT, and mSPECS-IPA-CAIPIVAT model with acceleration factor TPA=2, TPA=4, and TPA=8. B. The average activation detection rate (z-score) of ROI for slice 3 from mSPECS-IPA, mSPECS-IPA-CAIPIRINHA, mSPECS-IPA-VAT, and mSPECS-IPA-CAIPIVAT model with acceleration factor TPA=2, TPA=4, and TPA=8.

related signals, even when image reconstruction remains visually acceptable. Among the four models considered in this study, mSPECS-IPA-VAT showed the most stable performance across acceleration settings, maintaining comparatively higher *CNR* and z-scores under both simulated and experimental conditions. Previous studies suggest that an optimal multiband factor for resting-state fMRI is MB = 4 (Risk et al. [16]). From a practical perspective, the results suggest that moderate acceleration factors, such as IPA = 2 combined with TPA = 2, provide a more favorable balance between scan efficiency and activation detection performance, which is consistent with the conclusions of previous studies. Image-shift direction also had a substantial effect on reconstruction quality. Models incorporating vertical image shift, namely mSPECS-IPA-CAIPIRINHA and mSPECS-IPA-CAIPIVAT, generally showed poorer performance than models without vertical shift, especially at high acceleration factors. One possible explanation is that vertical image shift occurs in the same direction as the in-plane acceleration, leading to more complex slice overlap and voxel aliasing patterns. As the complexity of

40

slice overlap increases, the separation of aliased slices becomes more difficult, resulting in a less favorable conditioning of the reconstruction problem. In contrast, the horizontal shift used in mSPECS-IPA-VAT produced lower g-factor penalties and more favorable activation-related measures. These findings suggest that, within the present framework, image shift should preferably be applied in a direction different from the in-plane acceleration direction.

The Bayesian reconstruction framework provides voxel-wise posterior mean estimates together with associated uncertainty measures, allowing variability in the reconstructed signal to be quantified. The incorporation of calibration-derived prior information also introduces structured regularization that stabilizes the reconstruction under accelerated acquisitions. The advantages of this framework are most apparent under moderate acceleration settings and appropriate encoding strategies. In particular, improved activation detection was observed when IPA = 2 and TPA = 2, especially when horizontal image shift (VAT) was applied, where higher CNR and z-scores were obtained. At very high acceleration factors (e.g., TPA = 8), however, increased voxel aliasing and g-factor penalties reduce these benefits.

The proposed Bayesian framework should also be interpreted in relation to established SMS reconstruction methods such as Slice-GRAPPA, Split-Slice-GRAPPA, and MB-SENSE. Unlike these approaches, which produce deterministic voxel estimates, the present method provides posterior mean estimates together with voxel-wise posterior variance, enabling explicit uncertainty quantification. The Bayesian formulation also incorporates prior information from calibration images that introduces structured regularization and can stabilize reconstruction under accelerated acquisitions. The present study does not include a direct benchmark comparison with these techniques. Such comparisons are not entirely straightforward because conventional SMS reconstruction methods are typically designed for standard multiband acquisitions with fixed slice aliasing patterns separated using coil sensitivity information and calibration kernels. In contrast, the proposed framework incorporates additional encoding diversity through image-shift strategies combined with a 2D Hadamard phase-encoding scheme across multiple excitations. This design introduces structured variations in slice overlap and voxel aliasing patterns that are explicitly modeled in the Bayesian reconstruction framework but are not directly represented in conventional Slice-GRAPPA, Split-Slice-GRAPPA, or MB-SENSE formulations. A systematic benchmark under acquisition settings designed to support both the proposed framework and conventional SMS reconstruction pipelines will therefore be investigated

in future work using true multiband acquisitions and higher channel-count receiver arrays.

Several limitations of the proposed approach should be acknowledged. First, the 2D Hadamard encoding strategy requires multiple excitations to complete a full encoding cycle, which reduces the effective temporal sampling rate relative to conventional single-shot SMS acquisitions. Consequently, the framework is more naturally suited to block-design paradigms or moderate-TR studies than to high temporal resolution fMRI. Second, the current model assumes spatially independent Gaussian noise, whereas real EPI data may exhibit spatial and temporal correlations arising from physiological fluctuations and scanner drift. This independence assumption simplifies the reconstruction model but does not fully capture the noise structure present in practical fMRI acquisitions. Future extensions of the framework could incorporate more realistic noise models, such as spatial covariance structures or additional components representing physiological noise, to better characterize noise propagation in accelerated imaging. Third, the experimental study used an 8-channel receiver coil, which limits coil sensitivity diversity and is expected to reduce reconstruction stability under aggressive acceleration.

In summary, the present results suggest that the proposed Bayesian reconstruction framework provides a probabilistic approach for 2D-accelerated SMS fMRI that may offer advantages under certain acquisition settings, particularly with moderate acceleration and appropriate image-shift strategies. Among the configurations considered, horizontal image shift produced more stable reconstruction performance than vertical image shift within the current encoding design. The mSPECS-IPA-CAIPIVAT framework showed potential improvements in activation detection under these conditions, although the magnitude of the improvements was modest and depended on the acceleration and encoding configuration. The Bayesian formulation also provides voxel-wise uncertainty estimates and prior-based regularization derived from calibration data, which may help stabilize reconstruction in accelerated imaging. Consequently, the proposed approach should be interpreted as a complementary reconstruction framework that may offer benefits in specific scenarios rather than a universal replacement for existing SMS reconstruction methods. Future work will include higher channel-count receiver arrays, as well as extensions of the Bayesian model to incorporate more realistic spatial-temporal noise structures.

In traditional fMRI image acquisition techniques, images were collected slice-by-slice during the early development of fMRI studies. As imaging

techniques advanced, researchers focused on improving the efficiency of the image acquisition process while maintaining the ability to reconstruct high-resolution brain images. Two primary techniques have been developed to achieve this goal: through-plane acceleration and in-plane acceleration. Parallel imaging is one of the through-plane acceleration techniques, allowing multiple brain images to be acquired at each time point in an fMRI time series. A widely used in-plane acceleration technique, GRAPPA, can also reduce scan time by acquiring a subsampled k-space. In this study, through-plane acceleration and in-plane acceleration were combined to further shorten image scan time. However, due to the high similarity of coil sensitivity information in aliased voxels, additional techniques such as 2D Hadamard phase encoding and image shift were incorporated to mitigate the influence of the g-factor. As discussed in Section 2.1.2, the number of aliased brain images should be a power of 2 due to the constraints of the 2D Hadamard coefficient aliasing matrix. However, if an odd number of images are aliased, the orthogonal contrast aliasing matrix design can be incorporated into the model to maintain the orthogonality of the design matrix. In this study, we not only investigated the influence of net acceleration factors and image shift directions on model performance but also assessed the task activation detection ability of each model. The proposed 2D Hadamard encoded SMS framework requires multiple excitations to separate aliased slices, effectively reducing the temporal sampling rate compared to conventional single-shot SMS acquisitions. As a result, this approach is not intended to replace ultra fast SMS protocols designed for high temporal resolution event-related fMRI. Instead, it is best suited for block design or moderate TR paradigms where improved encoding diversity, reduced slice leakage, and enhanced CNR characteristics may outweigh the reduction in temporal resolution.

In this study, we first investigated the influence of high acceleration factors on the performance of the mSPECS-IPA, mSPECS-IPA-CAIPIRINHA, mSPECS-IPA-VAT, and mSPECS-IPA-CAIPIVAT models. Based on the simulated reconstructed results in Section 4 and the experimentally reconstructed results in Section 5, high acceleration factors had a positive impact on the SNR of the reconstructed images in the mSPECS-IPA and mSPECS-IPA-VAT models. As shown in Fig. 14 and Fig. 18, as the acceleration factor increased, the average SNR also increased. However, in models incorporating vertical image shift, the SNR of the reconstructed images decreased as the acceleration factor increased. This effect occurs because image shift in the same direction as the in-plane acceleration results in a more complex slice-overlapping pattern

43

than in models without vertical image shift. A similar conclusion can be drawn from the g-factor plot. The g-factor penalty in the mSPECS-IPA and mSPECS-IPA-VAT models is more stable compared to the mSPECS-IPA-CAIPIRINHA and mSPECS-IPA-CAIPIVAT models. As shown in Fig. 16 and Fig. 20, a high acceleration factor negatively affects the average CNR in each model. As the acceleration factor increased, the average CNR in the ROI decreased significantly across all models. However, among the four models, the mSPECS-IPA-VAT model exhibited the highest average CNR across different acceleration factors. A similar trend was observed in the task activation detection maps for each model under different acceleration factors. As the acceleration factor increased, the average z-score in the ROI decreased, indicating that capturing task activation signals became more difficult for all models at high acceleration factors. However, the mSPECS-IPA-VAT model maintained the highest average z-score in the ROI, making it the most sensitive model for detecting activation signals compared to the other models. Thus, with increasing through-plane acceleration, the SNR increases for all models, but the CNR values and task activation detection rates decrease. This trade-off necessitates a careful choice of the acceleration factor. Moreover, to balance the activation detection rate with efficient image acquisition, the recommended acceleration factors are TPA = 2 and IPA = 2.

We also investigated the influence of the image shift direction on the performance of each model. There are four different directions: mSPECS-IPA has no image shift technique, mSPECS-IPA-CAIPIRINHA has vertical image shift technique, mSPECS-IPA-VAT has horizontal image shift technique and the mSPECS-IPA-CAIPIVAT has vertical and horizontal image shift technique. Comparing the SNR, average CNR plot, and task activation detection maps, models incorporating vertical image shift, mSPECS-IPA-CAIPIRINHA and mSPECS-IPA-CAIPIVAT exhibited worse results in the reconstructed brain images. This is due to the increased voxel aliasing complexity when image shift occurs in the same direction as the in-plane acceleration (i.e., the phase encoding direction). Therefore, to avoid degraded reconstruction performance, it is recommended that image shift be applied in a direction different from the in-plane acceleration direction.

Moreover, other factors may also influence the performance of the novel image shift SMS technique, such as the location of the task activation signal and the size of the brain image. For example, if the task activation signal is generated in the posterior or anterior region of the brain, the mSPECS-IPA-VAT model is expected to perform better than the other models. In conclusion, the

~~novel image-shifted SMS technique is recommended to be used with a lower acceleration factor, and the image shift direction should be different from the in-plane acceleration direction to achieve optimal performance. The proposed Bayesian reconstruction framework is not designed as a direct replacement for Slice-GRAPPA or Split-Slice-GRAPPA in standard SMS acquisitions. Rather, it offers an alternative modeling perspective that emphasizes probabilistic inference, explicit uncertainty quantification, and the interaction between image shift strategies and encoding diversity. Future work will include direct comparisons using true multiband acquisitions with high channel count receiver arrays.~~

7. Acknowledgment

Appendix A. Supplemental Simulation Results

In the main text, we displays the temporal variance of the baseline signal of slice 3 from reconstructed images corresponding to four SMS models: mSPECS-IPA, mSPECS-IPA-CAIPIRINHA, mSPECS-IPA-VAT, and mSPECS-IPA-CAIPIVAT model with different through-plane acceleration factors. Fig. A.21 shows the temporal variance of task coefficient of slice 3 from the reconstructed images corresponding to the mSPECS-IPA, mSPECS-IPA-CAIPIRINHA, mSPECS-IPA-VAT, and mSPECS-IPA-CAIPIVAT with different through-plane acceleration factors. The top right corner is the slice overlapping scenario corresponding to the average of first N_α time point for each model, indicating the voxel aliasing complexity for each method. For TPA = 2 and IPA = 2, the voxel aliasing and slice overlapping conditions are identical for the mSPECS-IPA and mSPECS-IPA-CAIPIRINHA models, as well as for the mSPECS-IPA-VAT and mSPECS-IPA-CAIPIVAT models. Consequently, the temporal variance of the reconstructed images from mSPECS-IPA is similar to that of mSPECS-IPA-CAIPIRINHA, while mSPECS-IPA-VAT exhibits similar behavior to mSPECS-IPA-CAIPIVAT. Comparing temporal variance across different models, mSPECS-IPA and
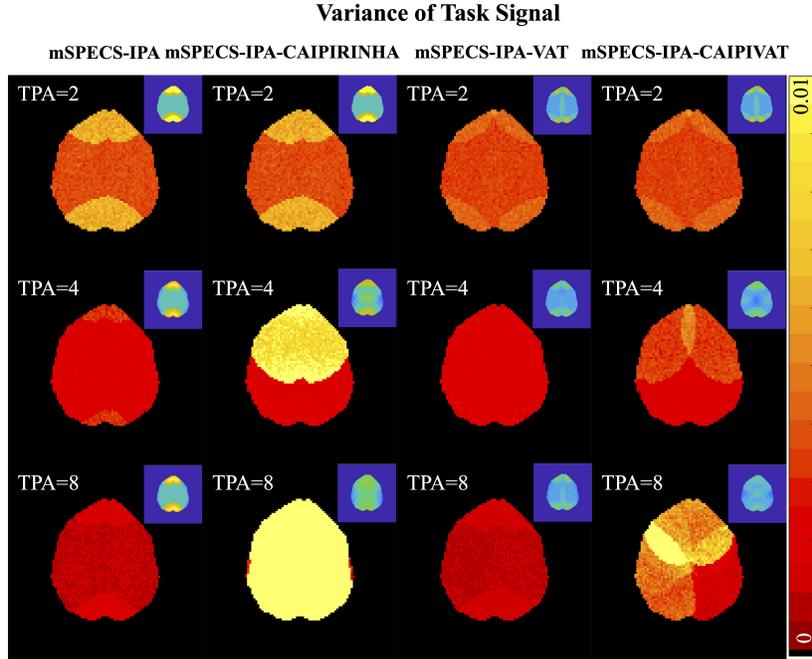
Variance of Task Signal

Figure A.21: The task regression coefficient variance of slices 3 from reconstructed images from mSPECS-IPA, mSPECS-IPA-CAIPIRINHA, mSPECS-IPA-VAT, and mSPECS-IPA-CAIPIVAT model with different through-plane acceleration factors. The top-right corner shows the overlapping indicator for each SMS reconstruction model under different TPA factors, illustrating the corresponding slice overlap and voxel aliasing patterns.

mSPECS-IPA-CAIPIRINHA yield higher variance values than mSPECS-IPA-VAT and mSPECS-IPA-CAIPIVAT, particularly in the posterior-to-anterior regions of the brain. When the through-plane acceleration factor increases to 4 and 8, mSPECS-IPA-CAIPIRINHA exhibits the highest temporal variance among the four models. Although the temporal variance in the posterior region is lower for mSPECS-IPA-CAIPIVAT compared to mSPECS-IPA-CAIPIRINHA, high temporal variance values are observed in the anterior region of the brain in the mSPECS-IPA-CAIPIVAT model. The mSPECS-IPA and mSPECS-IPA-VAT demonstrate better temporal variance performance compared to models incorporating vertical shifts. Among the four models, mSPECS-IPA-VAT provides the best temporal variance performance at high acceleration factors.

Fig. A.22 shows the temporal variance of the residual variance for brain images reconstructed from four SMS models: mSPECS-IPA, mSPECS-IPA-
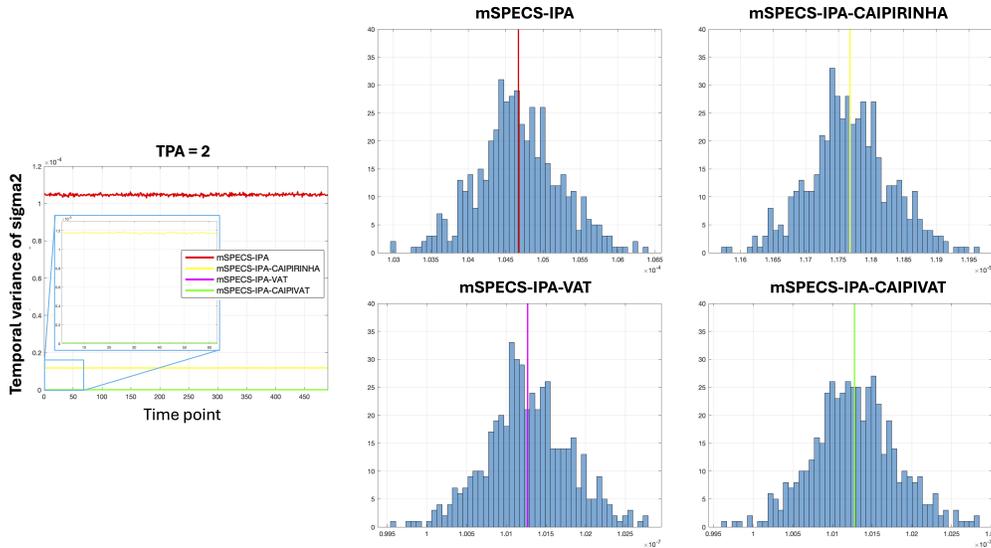
46

Figure A.22: The variance of the baseline regression coefficient of slice 3 from reconstructed images using the mSPECS-IPA (red), mSPECS-IPA-CAIPIRINHA (yellow), mSPECS-IPA-VAT (pink), and mSPECS-IPA-CAIPIVAT (green) models with IPA=2 and TPA=2. The curve corresponding to the mSPECS-IPA-VAT model (pink) closely overlaps with the curve for the mSPECS-IPA-CAIPIVAT model (green).

CAIPIRINHA, mSPECS-IPA-VAT and mSPECS-IPA-CAIPIVAT model with IPA = 2 and TPA = 2. Fig. A.23 shows the temporal variance of the residual variance for brain images reconstructed from the same model but with acceleration factor IPA = 2 and TPA = 4 and 8. Fig. A.22 and Fig. A.23 are generated from Eq. 28. For each acceleration factor, the mSPECS-IPA model has the highest temporal variance of residual variance, while the mSPECS-IPA-VAT and mSPECS-IPA-CAIPIVAT models have the lowest, with values approaching zero. Moreover, as the acceleration factor increases, the temporal variance of residual variance decreases for all four models.

Appendix B. Supplemental Experimental Results

Fig. A.24 shows the temporal variance of the reconstructed image of slice 3 for each model under different acceleration factors. As the acceleration factor increases, the temporal variance increases significantly in the mSPECS-IPA-CAIPIRINHA model. The temporal variance in the mSPECS-IPA-CAIPIVAT model also increases, particularly in the central region of the

47

Table A.1: Activation detection (z-score) and *CNR* for different reconstruction methods under varying through-plane acceleration factors for simulation results.

| | Activation Detection (z-score) | | |
Method	TPA = 2	TPA = 4	TPA = 8
mSPECS-IPA	2.91	1.84	1.24
mSPECS-IPA-CAIPIRINHA	2.93	1.42	0.45
mSPECS-IPA-VAT	3.00	1.88	1.18
mSPECS-IPA-CAIPIVAT	2.98	1.55	0.74
	CNR		
Method	TPA = 2	TPA = 4	TPA = 8
mSPECS-IPA	0.26	0.17	0.11
mSPECS-IPA-CAIPIRINHA	0.26	0.13	0.04
mSPECS-IPA-VAT	0.27	0.17	0.10
mSPECS-IPA-CAIPIVAT	0.27	0.13	0.07

brain, as the acceleration factor increases. However, in the two models without vertical image shift techniques, mSPECS-IPA and mSPECS-IPA-VAT, the temporal variance decreases. Moreover, in a comparison between these two models, the mSPECS-IPA-VAT model exhibits lower temporal variance
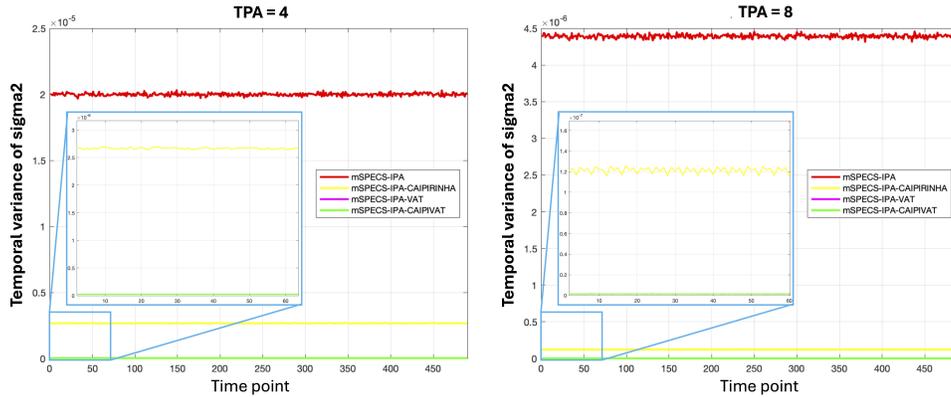

Figure A.23: Variance of the baseline regression coefficient of slice 3 from reconstructed images using the mSPECS-IPA (red), mSPECS-IPA-CAIPIRINHA (yellow), mSPECS-IPA-VAT (pink), and mSPECS-IPA-CAIPIVAT (green) models with IPA=2, TPA=4 and TPA=8. The curve corresponding to the mSPECS-IPA-VAT model (pink) closely overlaps with the curve for the mSPECS-IPA-CAIPIVAT model (green).
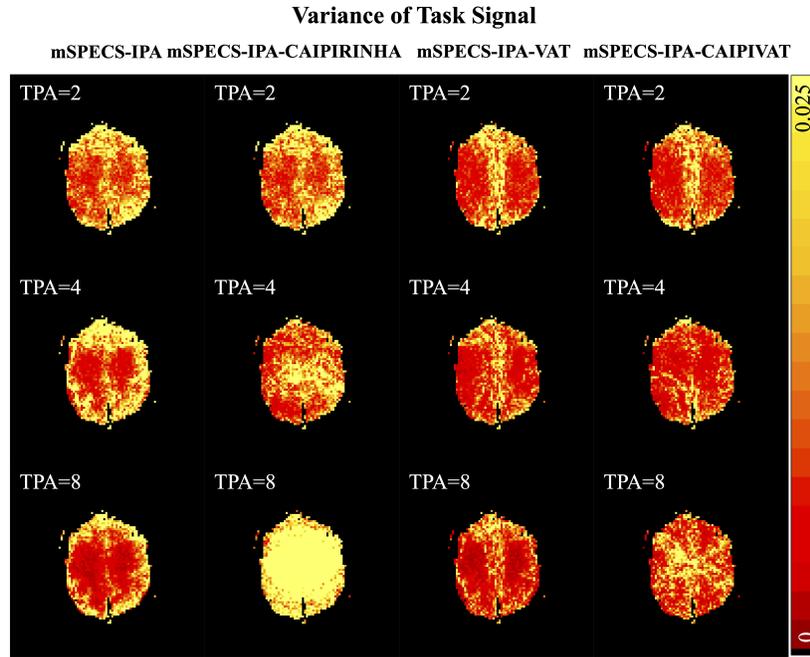
Variance of Task Signal

Figure A.24: The temporal variance of reconstructed image for slice 3 from mSPECS-IPA, mSPECS-IPA-CAIPIRINHA, mSPECS-IPA-VAT and mSPECS-IPA-CAIPIVAT model with different acceleration factor TPA=2, TPA=4, and TPA=8.

in the left and right motor cortex regions of the brain as the acceleration factor increases.

References

[1] Barth, M., Breuer, F., Koopmans, P. J., Norris, D. G., and Poser, B. A. *Simultaneous multislice (SMS) imaging techniques.* Magn Reson Med. 75(1):63–81. https://doi.org/10.1002/mrm.25897.

[2] Breuer, F. A., Blaimer, M., Heidemann, R. M., Mueller, M. F., Griswold, M. A., and Jakob, P. M. *Controlled aliasing in parallel imaging results in higher acceleration (CAIPIRINHA) for multi-slice imaging.* Magn Reson Med. 53(3):684–91. https://doi.org/10.1002/mrm.20401.

[3] Cho, Z. H., Kim, D. J., and Kim, Y. K. *Total inhomogeneity correction including chemical shifts and susceptibility by view angle tilting.* Medical physics. 15(1), 7-11. https://doi.org/10.1118/1.596162.

Table B.2: Activation detection (z-score) and *CNR* for different reconstruction methods under varying through-plane acceleration factors for experimental results.

Method	Activation Detection (z-score)		
	TPA = 2	TPA = 4	TPA = 8
mSPECS-IPA	2.80	1.64	1.08
mSPECS-IPA-CAIPIRINHA	2.85	1.37	0.34
mSPECS-IPA-VAT	3.69	2.31	1.21
mSPECS-IPA-CAIPIVAT	3.59	1.96	0.77
Method	*CNR*		
	TPA = 2	TPA = 4	TPA = 8
mSPECS-IPA	0.26	0.16	0.11
mSPECS-IPA-CAIPIRINHA	0.26	0.12	0.04
mSPECS-IPA-VAT	0.27	0.17	0.11
mSPECS-IPA-CAIPIVAT	0.27	0.14	0.07

[4] Cauley, S. F., Polimeni, J. R., Bhat, H., Wald, L. L., and Setsompop, K. *Interslice leakage artifact reduction technique for simultaneous multislice acquisitions*, Magn Reson Med, 72(1), 93-102. https://doi.org/10.1002/mrm.24898

[5] Fletcher, D. W., Haselgrove, J. C., and Bolinger, L. *High-resolution imaging using Hadamard encoding.* Magnetic Resonance Imaging. 17(10), 1457-1468. https://doi.org/10.1016/S0730-725X(99)00098-3.

[6] Griswold, M. A., Jamob, P. M., Heidemann, R. M., Nikkka, M., Jellus, V., Wang, J., Kiefer, B., and Haase, A. *Generalized autocalibrating partially parallel acquisition (GRAPPA).* Magn Reson Med. 47:1202–1210. https://doi.org/10.1002/mrm.10171.

[7] Hyde, J. S., Jesmanowicz, A., Froncisz, W., Kneeland, J. B., Grist, T. M., and Campagna, N. F. *Parallel image acquisition from noninteracting local coils.* Journal of Magnetic Resonance. 70(3), 512-517. https://doi.org/10.1016/0022-2364(86)90146-0.

[8] Jungmann, P. M., Ganter, C., Schaeffeler, C. J., Bauer, J. S., Baum, T., Meier, R., Nittka, M., Pohlig, F., Rechl, H., von Eisenhart-Rothe, R., Rummeny, E. J., and Woertler, K. *View-Angle Tilting and Slice-Encoding Metal Artifact Correction for Artifact Reduction*

in MRI: Experimental Sequence Optimization for Orthopaedic Tumor Endoprostheses and Clinical Application. PLoS One. 10(4):e0124922. https://doi.org/10.1371/journal.pone.0124922.

[9] Kociuba, M. C. *A Fourier description of covariance, and separation of simultaneously encoded slices with in-plane acceleration in fMRI.* Ph.D. Dissertation. Marquette University, Milwaukee, Wisconsin, USA. https://api.semanticscholar.org/CorpusID:114186307.

[10] Kim, M-O, Hong, T., and Kim, D-H. *Multislice CAIPIRINHA Using View Angle Tilting Technique (CAIPIVAT).* Tomography. 43-48. https://doi.org/10.18383/j.tom.2016.00109.

[11] Kim, M-O, Zho, S-Y, and Kim, D-H. *3D imaging using magnetic resonance tomosynthesis (MRT) technique.* Med. Phys. 39(8): 4733-4741. https://doi.org/10.1118/1.4737111.

[12] Lin, F. H., Kwong, K. K., Belliveau, J. W., and Wald, L. L. *Parallel imaging reconstruction using automatic regularization.* Magnetic Resonance in Medicine. 51(3), 559-567. https://doi.org/10.1002/mrm.10718.

[13] Mansfield, P. *Multi-planar image formation using NMR spin echoes.* Journal of Physics C: Solid State Physics. 10(3): L55. https://dx.doi.org/10.1088/0022-3719/10/3/004.

[14] Ogawa, S., Lee, T. M., Kay, A. R., and Tank, D. W. *Brain magnetic resonance imaging with contrast dependent on blood oxygenation.* Proc Natl Acad Sci USA. 87(24):9868-721. https://doi.org/10.1073/pnas.87.24.9868.

[15] Pruessmann, K. P., Weiger, M., Scheidegger, M. B., and Boesiger, P. *SENSE: Sensitivity Encoding for Fast MRI.* Magn Reson Med. 42:952–962. https://doi.org/10.1002/(SICI)1522-2594(199911)42:5<952::AID-MRM16>3.0.CO;2-S

[16] Risk, B. B., Murden, R. J., Wu, J., Nebel, M. B., Venkataraman, A., Zhang, Z., and Qiu, D. *Which multiband factor should you choose for your resting-state fMRI study?* Neuroimage. 234:117965. https://doi.org/10.1016/j.neuroimage.2021.117965

[17] Rowe, D. B., Bruce, I. P., Nencka, A. S., Hyde, J. S., and Kociuba, M. C. *Separation of parallel encoded complex-valued slices (SPECS) from a signal complex-valued aliased coil image.* Magn Reson Imaging. 34(3):359-69. https://doi.org/10.1016/j.mri.2015.11.003

[18] Rowe, D. B. and Logan, B. R. *A complex way to compute fMRI activation.* Neuroimage. 23(3):1078-92. https://doi.org/10.1016/j.neuroimage.2004.06.042

[19] Rowe, D. B., Nencka, A. S., Jesmanowicz, A., and Hyde, J. S. *Separation of two simultaneously encoded slices with a single coil.* In Proc Intl Soc Magn Reson Med. Vol. 21, p. 0123.

[20] Redzian, R., Mansfield, P., and Doyle, M. *Real-time nuclear magnetic resonance clinical imaging in pediatrics.* Lancet. 322:1281-2. 10.1016/S0140-6736(83)91153-4.

[21] Sakitis, C. J., Brown, D. A., and Rowe, D. B. *A Bayesian complex-valued latent variable model applied to functional magnetic resonance imaging.* Journal of the Royal Statistical Society Series C: Applied Statistics. 74(1), 100-125. https://doi.org/10.1093/jrsssc/qlae046.

[22] Setsompop, K., Gagoski, B. A., Polimeni, J. R., Witzel, T., Wedeen, V. J., and Wald, L. L. *Blipped-controlled aliasing in parallel imaging (blipped-CAIPI) for simultaneous multi-slice EPI with reduced g-factor penalty.* Magn Reson Med. 67(5): 1210-1224. https://doi.org/10.1002/mrm.23097.

[23] Souza, S. P., Szumowskim, J., Dumoulin, C. L., Plewes, D. P., and Glover, G. *SIMA - simultaneous multislice acquisition of MR images by Hadamard-encoded excitation.* J Comput Assist Tomogr. 12:1026–1030.

[24] Stehling, M. K., Turner, R., and Mansfield, P. *Echo-planar imaging: magnetic resonance imaging in a fraction of a second.* Science. 254(5028), 43-50. DOI: 10.1126/science.1925560.

[25] Welvaert, M. and Rosseel, Y. *On the Definition of Signal-To-Noise Ratio and Contrast-To-Noise Ratio for fMRI Data.* J PloS ONE. 8(11): e77089. https://doi.org/10.1371/journal.pone.0077089.

[26] Xu, K., and Rowe, D. B. *A Bayesian CAIPIVAT approach with through-plane acceleration to enhance efficiency of simultaneously encoded slice acquisition in FMRI..* Magnetic Resonance Imaging. 110540. https://doi.org/10.1016/j.mri.2025.110540.